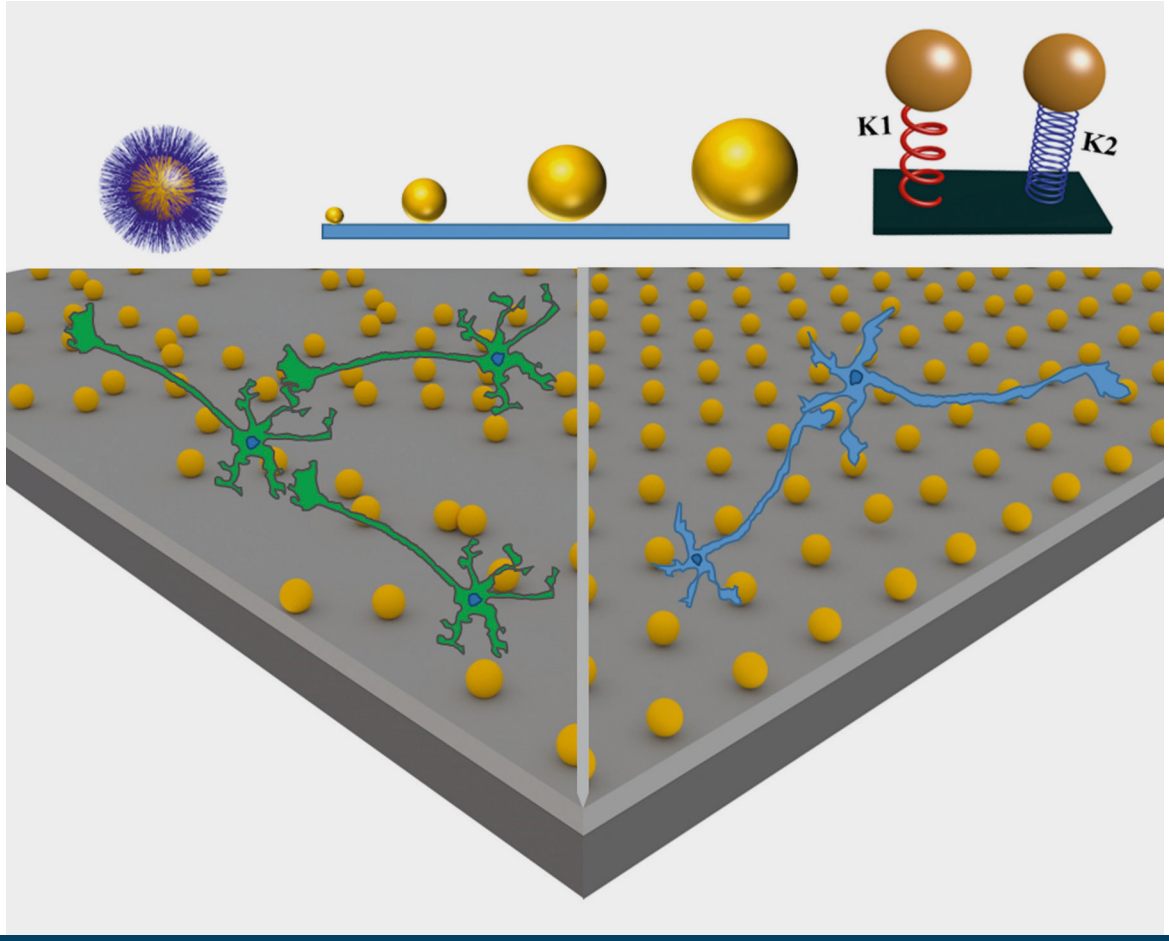

Control of neuron adhesion by metal nanoparticles

Anh Quang Tran

Schlüsseltechnologien / Key Technologies
Band / Volume 171
ISBN 978-3-95806-332-7

Mitglied der Helmholtz-Gemeinschaft

JÜLICH
Forschungszentrum

Schriften des Forschungszentrums Jülich
Reihe Schlüsseltechnologien / Key Technologies Band / Volume 171

Forschungszentrum Jülich GmbH
Institute of Complex Systems
Bioelectronics (ICS-8)

Control of neuron adhesion by metal nanoparticles

Anh Quang Tran

Schriften des Forschungszentrums Jülich
Reihe Schlüsseltechnologien / Key Technologies Band / Volume 171

ISSN 1866-1807 ISBN 978-3-95806-332-7

Bibliografische Information der Deutschen Nationalbibliothek.
Die Deutsche Nationalbibliothek verzeichnet diese Publikation in der
Deutschen Nationalbibliografie; detaillierte Bibliografische Daten
sind im Internet über http://dnb.d-nb.de abrufbar.

Herausgeber und Vertrieb:	Forschungszentrum Jülich GmbH Zentralbibliothek, Verlag 52425 Jülich Tel.: +49 2461 61-5368 Fax: +49 2461 61-6103 zb-publikation@fz-juelich.de www.fz-juelich.de/zb
Umschlaggestaltung:	Grafische Medien, Forschungszentrum Jülich GmbH
Druck:	Grafische Medien, Forschungszentrum Jülich GmbH
Copyright:	Forschungszentrum Jülich 2018

Schriften des Forschungszentrums Jülich
Reihe Schlüsseltechnologien / Key Technologies, Band / Volume 171

D 82 (Diss., RWTH Aachen University, 2018)

ISSN 1866-1807
ISBN 978-3-95806-332-7

Vollständig frei verfügbar über das Publikationsportal des Forschungszentrums Jülich (JuSER)
unter www.fz-juelich.de/zb/openaccess.

Abstract

The interaction between neurons and nanostructured materials is an increasing interest due to the possibility to manipulate the cells on the length scale of an individual biomolecule. A comprehensive understanding of neuron adhesion to non-biomaterials opens promising strategies to design neuronal network and for neuron-electrode integration. The neuronal adhesion can be mediated by specific receptor-ligand or non-specific interactions. The specific cell adhesion is often associated with the interactions between cell surface receptors (integrins) and their respective ligands from the extra cellular matrix (ECM) components or between hemophilic neuronal cell adhesion molecules (NCAMs) for cell-cell interactions. The non-specific cell adhesion is mainly induced by electrostatic interactions. NCAMs are associated with the negatively charge polysialic acid (PSA) and are known to be crucial for regulating neuronal adhesion. Previously, the chemical ligand 11-amino-1-undecanethiol (AUT) possessing positively charged terminals have been used to functionalize gold nanoparticles (AuNPs) on the substrate for tuning the neuron adhesion and neurite outgrowth. However, the preparation of cell culture samples has been restricted to the immobilization of disordered AuNPs only. Moreover, it has been found that the attachment of these AuNPs on the surface has been instable during long time cell culture, which results in particle aggregation and cytotoxicity due to particle uptake. Although the cell adhesion is obviously mediated by the electrostatic interactions, further studies to understand how charges and mechanical properties of the substrates affect the cell adhesion and neurite outgrowth are still missing. In this work, the block copolymer micelle nanolithography is used to synthesize both ordered and disordered AuNP arrays of different sizes and densities. Moreover, weakly bound (WB) and strongly bound (SB) AuNPs on the substrates can be obtained by tuning the oxygen plasma exposure time. The AuNPs are used as nanoplatforms to carry the AUT ligands, while the background is blocked by cell aversive molecules of 2-[methoxyl(polyethyleneoxy)6-9-propyl]trichlosilane (PEG).

The neuron adhesion and neurite outgrowth are firstly studied with WB AuNPs of different sizes and densities at sub 50 nm scale. It is found that the cell survival and neurite number increase with the rising ligand density and reach a saturation, independent of particle size. However, the axon outgrowth responses in a different manner. The average axon length exhibits an increase, a maximum, and a decrease phases, before reaching a plateau. The strong

influence of the electrostatic interactions for neuron adhesion is also confirmed by using different ligand concentrations or removing the PSA molecules from NCAM with a specific endoneuraminidase (Endo-N) enzyme. In both cases, a reduction in either ligand density (positive charge number) or the negative charge of PSA-NCAM on the cell surface result in decreasing neuron adhesion. Importantly, it is revealed that WB AuNPs cause drastic reduction in cell survival as compared to the SB particles. The cytotoxicity of immobilized AuNPs is investigated for different particle sizes, densities, and surface coupling strengths. It is also found that WB AuNPs can cause higher cytotoxic effects on neurons than the same particles dispersed in the culture medium. Besides the cytotoxicity, the surface coupling strength of AuNPs strongly affects the axon elongation of neurons. At a same ligand density range, WB AuNPs can enhance axon growth with increasing ligand density, while SB AuNPs dramatically reduce the axon length at the higher ligand density. This opposite behavior of the axon elongation on different particle coupling strength confirms the influences of mechanotransduction on neurite outgrowth also for the substratum-cell coupling via AuNPs.

Moreover, it is found that the distributions of AuNPs on the substrates can influence the neuron adhesion and neurite outgrowth. By a similar particle density (inter-particle distance) of each particle size, disordered AuNPs provide better capability for cell survival as well as neurite number than for the case of ordered AuNPs. However, the particle distribution does not affect the axon elongation.

Finally, by combining optical lithography with protein self-assembly, positively charged ferritin nanoparticle (FerNP) patterns are fabricated for controlling the neuron adhesion and neurite guidance. The positively charged surface of FerNPs acts as cell adhesion cues similar to the AUT ligands, while the background is passivated by the trichloro(1H,1H,2H,2H-perflueooctyl) silane molecules (FOTCS). A high guidance efficiency of 88% is observed for the neurite outgrowth due to the chemical contrast between the positively charged FerNPs and the FOTCS backfill. Importantly, the possibility of loading magnetic or other functional metal nanoparticles inside the nanocages of FerNPs opens potential applications for advanced controlling of cell adhesion.

Zusammenfassung

Die Wechselwirkung zwischen Neuronen und nanostrukturierten Materialien ist von steigendem Interesse, da mit Hilfe der Nanomaterialien Zellen auf der Längenskala einzelner Biomoleküle manipuliert werden können. Ein umfassendes Verständnis der Neuronenadhäsion an Festkörperoberflächen eröffnet vielversprechende Möglichkeiten gezielt neuronale Netzwerke aufzubauen und diese in bio-anorganische Hybridbauelemente zu integrieren. Die neuronale Adhäsion kann durch spezifische Rezeptor-Ligand oder nicht-spezifische Interaktionen vermittelt werden. Die spezifische Zelladhäsion ist mit den Wechselwirkungen zwischen Zelloberflächenrezeptoren (Integrine) und ihren jeweiligen Liganden der extrazellulären Matrix (ECM) assoziiert oder durch homophile neuronalen Zelladhäsionsmoleküle (NCAMs) bei Zell-Zell-Wechselwirkungen. Unspezifische Zelladhäsion werden dem gegenüber häufig durch geladene Molekülliganden induziert. NCAMs sind mit der negativ geladenen Polysialinsäure (PSA) assoziiert, die den Abstand zur benachbarten Zellmembran regulieren. In früheren Studien wurde deren elektrostatische Wechselwirkungen zu 11-Amino-1-undecanthiol (AUT) mit positiv geladenen Endgruppen genutzt, um die Neuronenadhäsion und das Auswachsen von Neuriten zu kontrollieren. Hierfür waren die AUT-Moleküle als chemischen Liganden an Goldnanopartikel (AuNP) gekoppelt. Bei diesen Partikeln handelte es sich jedoch ausschließlich um Partikel, die ohne Ordnung auf Festkörperoberflächen immobilisiert waren. In der vorliegenden Arbeit wurde festgestellt, dass die Oberflächenhaftung dieser AuNPs für lange Zellkulturzeiten instabil ist, was zu Partikelaggregation und Zytotoxizität führt. Obwohl die Zelladhäsion offensichtlich durch elektrostatische Wechselwirkungen vermittelt wird, fehlen weitere Studien die den Zusammenhang zwischen Ladungsdichte, Ladungsverteilung, Partikelbindungsstärke und Zelladhäsion bzw. Neuritenwachstum untersuchen. In dieser Arbeit wird die Blockcopolymer-Mizellen-Nanolithographie verwendet, um sowohl geordnete als auch ungeordnete AuNP-Anordnungen verschiedener Größen und Dichten zu erzeugen. Darüber hinaus können schwach (WB) als auch stark gebundene (SB) AuNP auf den Substraten generiert werden, indem die Zeit der Sauerstoffplasmabehandlung variiert wird. Die AuNP werden als nanoskalige Bindungsstelle für die AUT-Liganden verwendet, während der Hintergrund durch zellabweisende Moleküle 2- [Methoxy (polyethylenoxy) 6-9-propyl] trichlorsilan (PEG) blockiert wird.

Die Neuronenadhäsion und das Neuritenwachstum werden zunächst mit WB AuNP verschiedener Größen und Dichten im sub-50 nm Bereich untersucht. Es wurde festgestellt, dass die Zellvitalität und die Neuritenzahl mit wachsender Ligandendichte ansteigen und unabhängig von der Partikelgröße eine Sättigung bei gleicher Dichte an Ligandenladungen erreichen. Das Axonswachstum verhält sich davon jedoch verschieden. Die durchschnittliche Axonlänge nimmt zunächst zu, durchläuft ein Maximum und nimmt schließlich wieder ab bis sie ein Plateau erreicht. Für SB-AuNPs wurde ein deutlich unterschiedliches Verhalten beobachtet. Die Axonlänge nimmt kontinuierlich mit steigender Ligandendichte ab. Diese unterschiedliche Axonwachstumscharakteristik bestätigt und verdeutlicht die Bedeutung der Kraftübertragung zwischen Oberfläche und Zelle auf die Neuritenentwicklung.

Die große Bedeutung der elektrostatischen Wechselwirkungen auf die Neuronenadhäsion wurde durch Verwendung unterschiedlicher Ligandenkonzentrationen und durch Entfernen der PSA-Moleküle vom NCAM mithilfe von Endoneuraminidase (Endo-N) -Enzym verifiziert. Sowohl die Verringerung der Ligandendichte (positive Ladungen, Partikel) als auch der PSA-NCAM (negative Ladungen, Zelle) führt zu einer abnehmenden Neuronenadhäsion. Weiterhin wurde beobachtet, dass die Verwendung von WB AuNPs im Vergleich zu SB AuNP zu einer drastischen Reduktion der Zellvitalität führt. Die Zytotoxizität immobilisierter AuNPs wird durch die Partikelgrößen, Dichten und Oberflächenkopplungsstärken beeinflusst. Die Zytotoxizität WB AuNPs kann sogar höher sein als die vergleichbarer kolloidaler Partikel.

Darüber hinaus wurde festgestellt, dass die Verteilung der AuNPs auf den Substraten die Neuronenadhäsion und die Neuritenbildung beeinflussen. Ungeordnete AuNP ermöglichen eine höhere Zellvitalität und Anzahl an Neuriten als geordnete AuNP bei vergleichbare Partikeldichte. Dem gegenüber beeinflusst die Partikelverteilung das Axonswachstum kaum.

Schließlich werden durch Kombination von optischer Lithographie und Selbstorganisation positiv geladene Ferritin Nanopartikel (FerNP) Strukturen zur Steuerung der Neuronenadhäsion und Neuritenausrichtung hergestellt. Ähnlich wie bei den AUT-Liganden wirken die positiven Ladungen der FerNP als Zelladhäsionssignale, während der Hintergrund durch die Trichloro (1H, 1H, 2H, 2H-perfluorooctyl) silanmoleküle (FOTCS) passiviert wurde. Aufgrund des chemischen Kontrasts zwischen den positiv geladenen FerNPs und dem FOTCS-Hintergrund wird eine hohe Ausrichtungseffizienz von 88% für das Neuritenwachstum

beobachtet. Die Möglichkeit, magnetische oder andere funktionale Metall-Nanopartikel in die Ferritinpartikel zu laden, eröffnet potentielle Anwendungen für eine verbesserte Kontrolle der Zelladhäsion.

Table of Contents

1. INTRODUCTION

Cell functions are based on the interaction of cells and their surrounding structures. For the adherent cells, cell differentiation, proliferation and migration are highly regulated by adhesive interactions. The interactions of cells and nanostructured materials have attracted interest due to the possibility to manipulate cells on the length scale of an individual biomolecule. The adhesion of cells to the nanostructured substrate can influence their survival,[1-2] differentiation,[3-4] motility,[4-6] and in case of neurons, also their excitability.[7-8] Nanomaterials, especially gold nanoparticles (AuNPs) have been used as nanostructure platforms for biological applications.[9-11] The universal usability of AuNPs is because of their biocompatibility, easy preparation, and straightforward ligand immobilization (utilize the special gold-thiol affinity). By controlling the particle size and density, the amount of cell adhesive cues functionalized AuNPs on surfaces can be well controlled. Many studies used AuNPs as platforms to study cell adhesion for various types of cells.[12-14] However, most studies were performed on different cell types than neurons. Moreover, the utilized adhesive ligands are often associated to specific interactions (directly induced integrin binding) such as cell receptor mediated adhesion of arginylglycylaspartic acid (RGD) or other laminin derived peptides. Neurons differ from other cell types as they possess dendrites and axons. Another difference is that they communicate with each other by electrochemical signals via synapses. Neurons seem to prefer adhering on soft substrates rather than stiff substrates like most other cell types such do as fibroblasts or epithelial cells.[15-17] Although there have been studies on neuronal adhesion, the detailed understanding of the mechanism behind still remains obscurity until now. Neural cell adhesion molecules (NCAMs) are cell-surface glycoproteins, which mediates cell adhesion, migration, and plasticity in the nerve system.[18] The negatively charged polysialic acid (PSA) is found to associate with the NCAM has an important role in regulating neuronal adhesion.[18-20] Moreover, it is reported that cell adhesion can be influenced by non-specific interactions such electrostatics interaction between the positively charged ligand coating on substrates and the negative charge from the PSA-NCAM or other glycocalyx proteins on the cell surface.[21-22] These studies have shown that non-specific interaction can be even stronger than specific adhesion. Although the electrostatic effect on cell adhesion are obvious, the detail mechanism how charges induce cell adhesion is still not well understood. A comprehensive understanding of cell adhesion is indispensable for

succeeding in regulation of neuronal outgrowth on non-biomaterials for biotechnological applications such as implant devices or neuroelectronic signal recording.

In recent reports, P.Li at al. has shown that AuNPs can be used for controlling neuronal adhesion.[23-24] In this study, the neuron adhesion and neurite outgrowth were studied by tuning the density of chemical cell adhesive ligands which were immobilized on the substrates via AuNPs, while the background was blocked by different cell repulsive molecules. It was found that the cell viability increases with the ligand density, which is independent of particle size. The influences of AuNP sizes, densities and particle patterns on neurite outgrowth and polarization had been also studied and reported. However, other important parameters of AuNPs such as the surface coupling strength, particle distribution, and cytotoxicity can also affect neuron adhesion and cell differentiation. More importantly, when studying neuron-material interactions for neurobioelectronic devices or long time in-vitro cell cultures, the cytotoxic effects of the non-biomaterials on the cells are crucial and need to be carefully investigated. Moreover, the AuNP immobilization method based on the salanization[23, 25] shows a limitation in fabrication of the ordered AuNP array as well as stable surface coupling strength of AuNPs.

The goal of this thesis is to provide a more comprehensive study of neuron adhesion and neurite outgrowth by investigating the influence of not only the particle sizes and densities, but also the particle coupling strength and distribution on neuron adhesion. An alternative AuNP synthesis will be introduced for this work, the block copolymer micelle nanolithography, which allow to directly synthesis both ordered and disordered AuNPs of different sizes and densities on the silicon substrates.[26-31] For the first time, chemical cell adhesive ligands immobilized on the surface via AuNPs of different sizes, densities, coupling strengths and distributions are used for a comprehensive study of neuron adhesion and neurite outgrowth during long time in-vitro culture. This work will also provide more detail about some remaining issues from our preliminary experiments such as the cytotoxicity of AuNPs and the influence of charges on neuron adhesion. Moreover, the electrostatics interaction of the positively charged ligand and the PSA-NCAM on cell surface is further studied by using a specific enzyme, which can cleave the cell-ligand interactions. Last but not least, motivated by the novel achievement from Beck et al.[32] a new approach of neuron adhesion and neurite guidance is established by using positively charge ferritin nanoparticle (FerNP) patterns as the nanostructured platforms. The

FerNPs can be loaded with different (magnetic) material nanoparticles, which opens a possibility for more advanced neuron adhesion regulation, for example, selectively spatio-temporal controlling of the cell adhesion by an external magnetic field.

2. FUNDERMENTALS

This chapter will summarize background information relevant for this thesis for a better understanding the experiments and results. The fundamental concepts of neuron adhesion, neuron-nanomaterial interaction, and methods for nanostructure fabrication and characterizations will be mentioned.

2.1 Biological background

2.1.1 Neuron

Neurons are the basic working units in the nervous system, which can be electrically excited, so that the cells communicate with each other through electrical and chemical signals. The mammalian brain contains from 100 million to 100 billion neurons, depending on the species. Neurons are similar to the other cells as they have a cell body with cell membrane, a nucleus and many other organelles (Figure 2.1). However, neurons differ from other cells because their cell body (soma) possesses extension parts called neurites. The cell body contains a nucleus and cytoplasm, while the neurites arise from the cell body and often extend for hundreds of micrometers and branch multiple times. The neuritis consists an axon and dendrites, particularly when the neuron is in its undifferentiated stage. The axon extends from the cell body by elongating its terminal part (growth cone) and often branches before connecting to the dendrites of other neurons by synaptic connections. The neuron adheres not only to the other neurons to form a neuronal network, but also to the extracellular matrix (ECM) or to the substrates. The

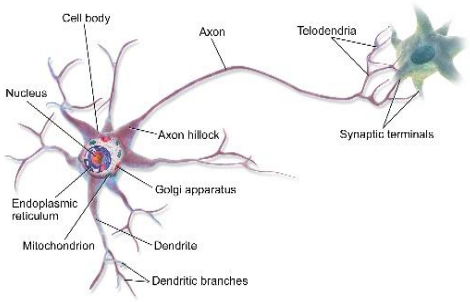

Figure 2.1 Anatomy of a typical neuron with a cell body containing a nucleus and other organelles and an axon and dendrites. (BruceLaus, wiki).

neuron adhesion allows neuronal migration and differentiation, neurite outgrowth, axonal fasciculation, synapse formation and plasticity. Hippocampal and cortical neurons are commonly used for studying a variety of cell functions such as neurite initiation and extension in short-term cultures. These neurons are also easier to handle compared to neurons from other regions in the central nervous system. Moreover, the neurons express many key phenotypic features such as well-developed dendrite branches and synaptically connected network formation.[33] Importantly, both hippocampal and cortical neurons are located in primary regions that are responsible for information acquisition, storage, and processing.[34] These regions can be significantly suffered by neurondegenerative diseases such as Alzheimer, epilepsy, and stroke. Therefore, these neuronal cell lines are excellent candidates and accessible models for studying normal neuronal development.

2.1.2 Cell adhesion

Cells interactions to other cells, ECM or substrate is called cell adhesion. Cell adhesion is essential in cell communication and regulation. It also plays a pivotal role to maintain 3D structure and the cell functions in tissue. Cell adhesion also involves in cell spreading, migrating and signal transduction.[35] The cell adhesion is typically mediated by multiprotein complexes involves three: the cell adhesion molecules (CAMs)/adhesion receptors, the ECM proteins, and the cytoplasmic plaque/peripheral membrane proteins. The cell adhesion molecules (receptors)

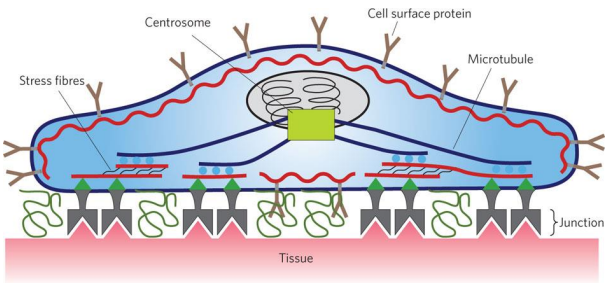

Figure 2.2 Cell adheres to a surface, such as tissue, via cell adhesion domains. The adhesion domains which are formed by the attachment of cell adhesion molecules (CAMs)/ receptors (integrins) and surface adhesive cues of the ECM, link the cell to the surface by clusters of adhesion complexes between integrins and cytoskeletal. The adhesion domains act as anchors which not only maintain the global mechanical stability, but also have an important role in cell-force sensing.[36]

are usually transmembrane glycoproteins such as the integrin, cadherin, immunoglobulin, selectin or proteoglycan superfamilies. The receptors from cell surface can recognize and adhere to either other cell adhesion receptors of neighbouring cells or tissues or to the ECM. At the intracellular part of the membrane, the integrin receptors associate with cytoplasmic plaque of peripheral membrane proteins to form adhesion complexes (ACs), which link the cell cytoskeleton to the outer part of cell membrane. Thus, the cell can sense and transduce the signal through their adhesion receptors on the cell surface. An example of a cell adheres to a soft surface, such as tissue (Figure 2.2).[36-37] Here the cell surface receptors (integrins) associated with CAMs adhere specifically to the ECM (such as collagen fibrils) forming adhesion domains. At the adhesion domain inside the cell membrane, the integrins are linked to the actin and microtubule cytoskeleton through adhesion complexes, which are formed by the clustering of different adapter proteins.[38-40] Indeed, the adhesion complexes are typically formed by different intracellular proteins (can be over 100 different proteins such as talin, vinculin and tensin) into large macromolecular complexes, which connect the cell receptors to the cell-organizing centrosome via actin and intermediate filaments. The example of adhesion complexes (AC) which link actin filaments to the integrins (Figure 2.3).[41] Many proteins involved in the AC have specific roles in cell signaling. For example, vinculin proteins which link integrin adhesion molecules to the actin filaments have an important role in mechanotransduction of cells.[42-44] Therefore, the coupling of these adhesion domains to the cell cytoskeleton not only maintains the global mechanical stability of the cell, but also has an important role in the cell's mechanical sensing ability of surrounding environment. Moreover, the cells can transfer the tension forces to the substrates via the adhesion sites which formed by AC proteins.[45-47] The ACs also involve in cell migration, proliferation and cell survival as well. [48-50] This adhesion of the cell to the ECM is considered as specific binding, in which the transmembrane receptors (integrin) of cells specifically bind to the ligand molecules such as laminin, fibronectin and collagens. For example, in mammals, the integrin receptors such as α3β1, α4β1, α6β1, α7β1, α6β4 in a variety of cell types have highly binding specificities and affinities to the laminin.[51] The specific cell adhesion can be also the adhesion through binding between specific cell membrane receptors and corresponding CAM functionalized substrates.[52-55] Likewise, the surface coated substrates with the laminin-derived synthetic peptide, PA22-2 (CASRARKQAASIKVAVSADR), IKVAV or the arginylglycylaspartic acid (RGD) peptide, can promote neuronal adhesion and

stimulate neurite outgrowth by its specifically affinity on the integrin receptors.[21, 56] Beside from the specific binding, cell adhesion can be mediated by non-specific interactions between the surface and cells such as electrostatics and van der Waals interactions. Although many adhesion proteins are involved similarly as specific adhesion, the electrostatic interaction of cells is considered as a passive process of non-specific and non-receptor mediated adhesion. In some cases, the nonspecific adhesion of hippocampal neurons on a positively charged poly-D-lysine (PDL) surface is found to be even higher than the specific adhesion of cells.[21-22] For neural cells, the polysialic acid (PSA) moiety of neural cell adhesion molecule (NCAM) regulates cell-cell and cell-substrate adhesion through electrostatic interactions.[18, 57-59] The PSA is mainly located at the terminal of linear branch glycans on cell surface glycoproteins (glycocalyx). The repulsive interaction of PSA-NCAM between adjacent cells facilitates cell migration, plasticity, and cell-cell adhesion. [19-20, 60] Moreover, the attractive interactions between the negative charged of PSA-NCAM and positively charged adhesion ligands immobilized to a substrate can be used to control the cell adhesion and therefore regulating their viability and differentiation.[24, 61-64]. Thus, the cell adhesion can be regulated if the electrostatic interaction of PSA-NCAM is interrupted.

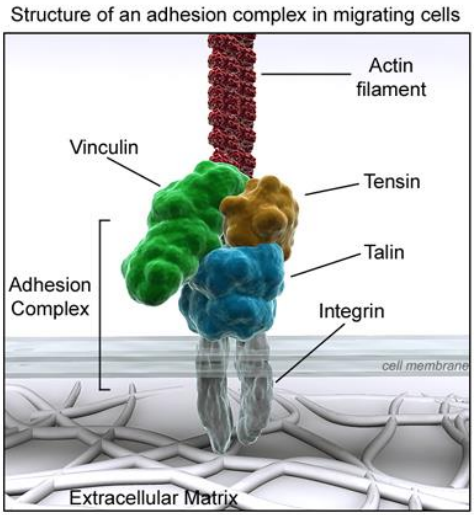

Figure 2.3 Composition of a adhesion complex (AC) formed by arrangements of different proteins such as vinculin, tensin, talin, and so on.[41]

2.1.3 Cell-material interfaces

The adhesive interaction between cell and material surface is bi-directional and dynamic and should mimic the natural interactions of cells and the extracellular matrix (ECM).[65-66] Cell adhesion to material surfaces at nanoscale is fundamental for the design of biomaterial substrates for biological applications such as medical implants or in-vitro cell cultures. The interface between cells and nonbiological surface regulates cell adhesion and therefore influences cell function, development and cell viability.[5, 67-68] A complete understanding of cell adhesion to materials is pivotal to enhance the biocompatibility of the materials and to minimize scar tissue formation. This also opens promising strategies for development of tissue-engineering applications or cell-electrode integration to meet the biochemical and biophysical requirements.

There are three main material properties that influence of adhesion of cells: surface topography,[69-71] compliance,[72-74] and the surface chemical compositions.[75-79] For topography influences, many experiments have found that cells response differently to different topography surfaces.[80-82] The substrate topography can determine neuron polarization, growth and nerve regeneration.[83-84] Secondly, the mechanical properties of substrates have been confirmed to strongly affect cell adhesion. For example, the stiffness of the substrate can directly regulate stem cell differentiation in different lineages.[85] Neurons are differed among mechanosensitive cells that seem to prefer soft to stiff substrates.[15, 86] The stiff substrate can also enhance cultured neuronal network activity.[87] Finally, in terms of surface chemical compositions, it has been found that a change in surface chemistry significant effect on cell function.[88-90] Nano-fabrication techniques and surface chemically modifications allow to functionalize surface chemistry for controlling the cell adhesion.[24, 62, 91-92] For examples, cell adhesive ligand functionalized AuNPs were decorated on substrates to control the neuron adhesion by various parameters such as particle sizes, densities and binding strengths.[24, 61]

2.2 Nanolithography fabrication

2.2.1 Block copolymer micelle nanolithography

The block copolymer micelle nanolithography is a bottom-up, self-assembly method utilized for nanofabrication. This technique employs intrinsically chemical or physical forces, which operate at the nanoscale to assemble basic units into larger structures.[93] Here, the self-organization of macromolecules allows fabrication of well-ordered arrays (hexagonal) of

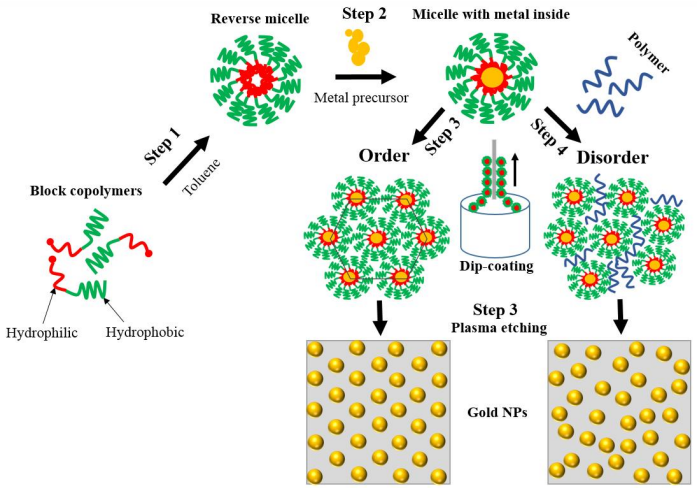

Figure 2.4 A schematic principle of nanoparticle synthesis using the micellar method. Reverse micelles formed in a non-polar organic solvent toluene with their polar heads towards to interior of the micelles forming spheres (step 1). Metal precursors, such as gold salt, can be loaded into the cores of the micelles (step 2). The micelles with loaded metal precursor will be transferred onto the substrate with a hexagonally ordered arrangement (in step), or a disordered arrangement (by adding extra polymer in step 4). Finally, the polymers are etched by plasma leaving the AuNPs on the substrates.

nanoparticles with adjustable sizes and inter-particle spacing on a variety of substrates. In this method, reversed micelles are formed by dissolving a block copolymer such as *polystyrene(x)-b-2-poly-vinylpyridine(y)* (*PS(x)-b-P2VP(y)*), in a non-polar solvent (Figure 2.4). Here x and y are the monocular weight (MW) of each polymer chain respectively. The resulting reverse micelles provide nanosized compartments for loading a metal precursor, which can be added with the precise amount calculated depending on the added polymers (step 2). Using the dip-coating technique, the reverse micelles confining the metal salt can be transferred onto the substrate with a highly-ordered arrangement according to the self-assemble processes (step 3). Finally, the nanoparticles are formed on the substrate after the polymers are etched by oxygen plasma.[14, 94-96] Using this method, the size of the nanoparticles can be tuned by using different loading ratio (LR) of the metal salt adding and by choosing the appropriate block length of the *P2VP* block of the copolymer. On the other hand, the inter-particle distance can be adjusted by choosing the appropriate *PS* block length or modulating the dip-coating speed. The arrangements of nanoparticles are also alternated by adding extra hydrophobic polymer (step 4) for disordered NP array.

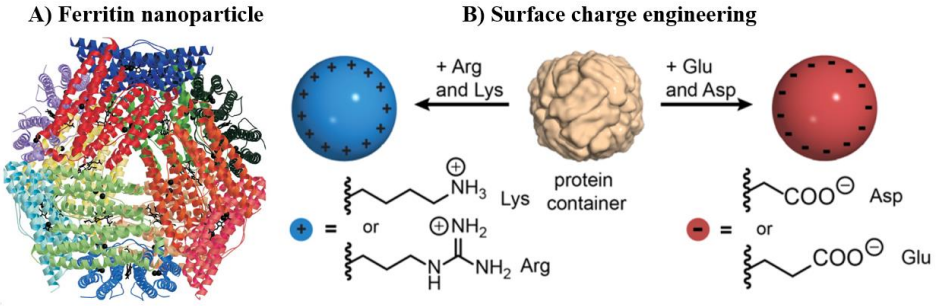

Figure 2.5 A) The structure of ferritin formed by a family protein into a nanocage, which can conain iron ions.[98] B) The ferritin can be engineered to possess a positively (left) or negatively (right) surface charge.[32]

2.2.2 Ferritin nanoparticles

Ferritin is a universal intracellular protein that can store or release irons in a controlled fashion. In nature, ferritins are found in all domains of life. They are composed of 24 protein subunits to form a cage architecture with a range of 10 nm.[97] A typical structure of ferritin from the bacterium, Desulfovibrio desulfuicans, which is formed by 24 homodimer subunits (Figure 2.5A).[98] There have been many reports that ferritins can be used for bionanotechnology applications such as building nanodevices, medical imaging, or drug delivery.[99] Moreover, Beck at al. has shown that the total charge of ferritins can be engineered to possess a positive or negative surface net charge (Figure 2.5B).[32] The nanocages of ferritins can be loaded with different inorganic NPs, such cerium oxide or cobalt oxide The positively or negatively charged surface of ferritin NPs (FerNPs) can act as cell adhesive or repulsive cue, which regulates cell adhesion through electrostatic interactions.

2.3 Characterization techniques

2.3.1 Scanning Electron Microscopy (SEM)

A scanning electron microscope (SEM) is an electron microscope that produces images of a sample surface by using a focused beam of electrons. During imaging, the electrons are emitted and interact with atoms in the sample surface. The interaction produces various signals that contain information about the sample's surface topography and composition. The SEM allows researchers to examine a big variety of specimens with many advantages over traditional optical microscopes. One of the main advantages is it can produce very higher resolution images of a sample surface (about 10 nm in size). The electron beam follows the path through

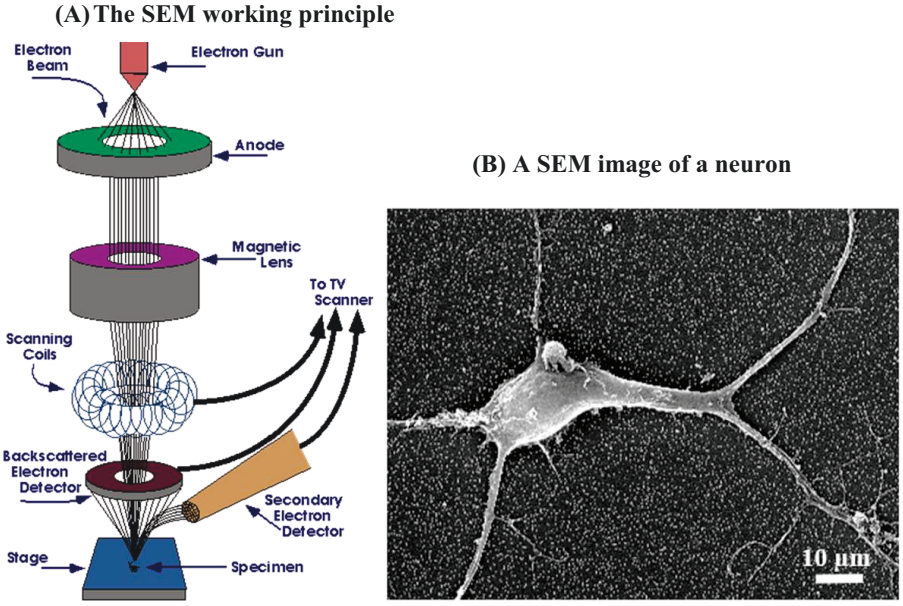

Figure 2.6 A) The working principle of a scanning electron microscope (SEM), (source: enfo.agt.bme.hu). B) A SEM image of a neuron cultured on nanostructure after sample preparation steps of cell fixation, dehydration, and metal sputtering.

electromagnetic lenses, which focus the beam down toward the sample in vacuum (Figure 2.6A). When the electron beam hits the sample, electrons and X-ray are emitted from the surface of sample. Detectors will collect emitted beams such as X-rays, secondary electrons (SE) and backscattered electrons (BSE) in order to process and produce the final image. The SE detection is the most common SEM mode. In the SE imaging, the low-energy SE are emitted from atoms at very close specimen surface when they are excited by an electron beam. Consequently, the emitted SE is collected by a special detector to create the high-resolution image of sample topography. In order to image deeper locations within specimen, a BSE imaging mode is use. The BSE consist high-energy electron beams that are reflected from the sample by elastic scattering interactions. Since the backscattering interactions are higher in heavy elements than the light elements, the BSE mode can be used to detect different contrast between different chemical compositions.

As the SEM works under vacuum conditions and uses electrons to for imaging. Therefore, all water inside the samples must be removed, as the water would vaporize in the vacuum. For

biological samples such as cells or tissues, they must be technically dried, while their structures should be preserved. Therefore, live cells or tissues will be fixed to remain their 3-D structures by a chemical fixation method. The sample can be also stained with heavy metallic materials to enhance contrast such as osmium tetroxide, uranyl acetate, lead or copper citrate.[100] The samples also need to be conductive. Non-conductive samples need to be covered with a thin layer of conductive material (sputter coater). Gold, platinum and iridium are usually used as conducting materials for coating bio-specimen. An example of a SEM image of a neuronal cell after performing sample preparation steps such as cell fixation, dehydration, and metal sputtering (Figure 2.6B).[101]

2.3.2 Focused Ion Beam (FIB)

Focused ion beams (FIB) previously used for material and semiconductor sciences, are nowadays powerful tools for ultrastructural imaging of biological samples. The FIB technique allows to create fresh cross-sections of cells or biological specimens by the progressive removal of materials, so that the internal structures of the samples can be imaged by the SEM. FIB can also image samples directly like the SEM by detecting emitted electrons from the sample surface. Additionally, FIB can be used as a sculpting tool to create specific specimen shapes such as lamellae or needles for further investigations of transmission electron microscopy (TEM) or chemical composition analysis.

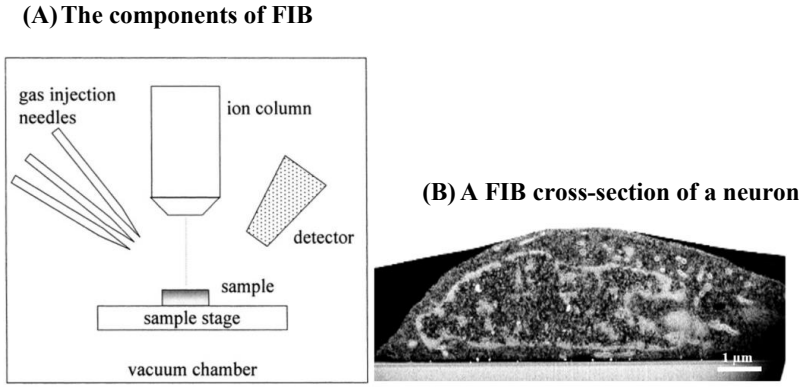

Figure 2.7 A) The principle of focused ion beam (FIB). B) The FIB cross-section of a neuron cell after sample preparation steps of cell fixation, metal staining, dehydration, resin embedding and surface sputtering.

The basic FIB instrument consists of vacuum chamber, liquid metal ion source, an ion column, a sample stage, detectors, and gas delivery systems (Figure 2.7A). FIB systems use a finely focused ion beam, especially gallium (Ga^+), to modify and image the sample of interest. For FIB imaging, low beam currents are often used, while high beam currents are required for sputtering or milling specific sample location. The primary Ga+ ion beam hits the sample surface, which results the emission of secondary ions (i^+ or i^-) and neutral atoms (n^0) as well as secondary electrons (e^-). As the primary beam scans on the sample surface, the signal from the ions or secondary electrons is collected to produce an image. However, to obtain the highest resolution imaging and prevent damage to sensitive samples, SEM imaging is still required. The combination of SEM and FIB columns onto the same chamber allows to take the advantages of both techniques. In the SEM and FIB combination, both the ion beam and the electron beam are used as a dual-beam system, which complement each other to allow sample preparation, imaging, and analysis can be accomplished in one system.

As the FIB works in vacuum condition and is usually combined with the SEM, so the samples also need to be completely dry. For biological samples, the same sample preparation steps as mentioned in the SEM section, are required before performing the FIB experiments. An example of SEM imaging of a FIB cross-section performed with a neuron after preparing with cell fixation, osmium tetroxide and uranyl acetate staining, cell dehydration, resin embedding, and metal sputtering.[101] Here, the ion beam is used to remove materials of the cell for creating a cross-section, while the electron of beam is used to image the cross-section by the SEM with BSE imaging mode. An example of a SEM image of a FIB cross-section of a neuron after performing sample preparation steps such as cell fixation, heavy metal staining, cell dehydration, resin embedding, and metal sputtering (Figure 2.7B).

2.3.3 Atomic Force Microscopy (AFM)

Microscopes have historically been used as important tools in biological analysis. The atomic force microcopy (AFM) is one of the most powerful techniques for studying insulators and semiconductors as well as electrical conductors. The AFM probes the surface of a sample by a sharp tip attached at the end of a cantilever (Figure 2.8A). The tip is often a couple of microns in length and less than 100Å in diameter. Forces between the tip and the sample surface cause the cantilever to bend or deflect. In this case, the cantilever acts as a spring and follows the rule

(B) The working principle of AFM **(A) An AFM image of AuNPs**

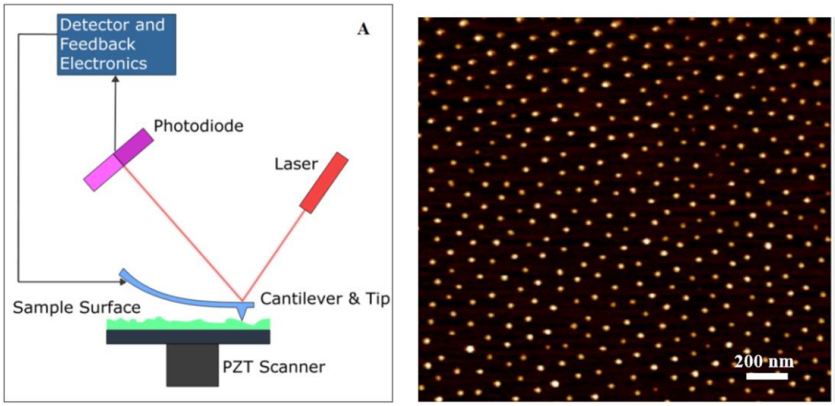

Figure 2.8 A) The principle of the atomic force microscope (AFM) (source: wikipedia.org). **B)** The AFM image of array of nanoparticles decorated on a substrate.

of *Hooke's law*.[102] A detector will measure the deflection of a laser beam caused by the vibration of the cantilever when the tip is scanned over the surface of the sample. The measurement of the cantilever deflections allows a computer to plot a map of surface topography[103].

AFM can work in two main scanning modes, contact and non-contact modes (regimes). In the contact regime, the cantilever is held less than a few angstroms from the sample surface, whereas in non-contact mode the tip stays at a distance of 10 to 100 nm from the sample. However, another mode called,''tapping mode'', which belongs to the non-contact regime, is most commonly used. In the tapping mode, the tip will vibrate above the surface of the substrate at a certain resonant frequency. The change of the forces between the surface and tip by modulating amplitude setpoint during scanning, will result in a change of vibration amplitudes of the tip. The tapping mode take advantages of both contact and non-contact modes. It eliminates friction forces by intermittently contacting the surface, therefore minimize damage on the sample. Moreover, the oscillation with sufficient amplitude of tapping mode prevent the tip being trapped by adhesive meniscus from the possible contaminant layer of sample surface. An example of AuNP array is imaged by the AFM with the tapping mode (Figure 2.8B).

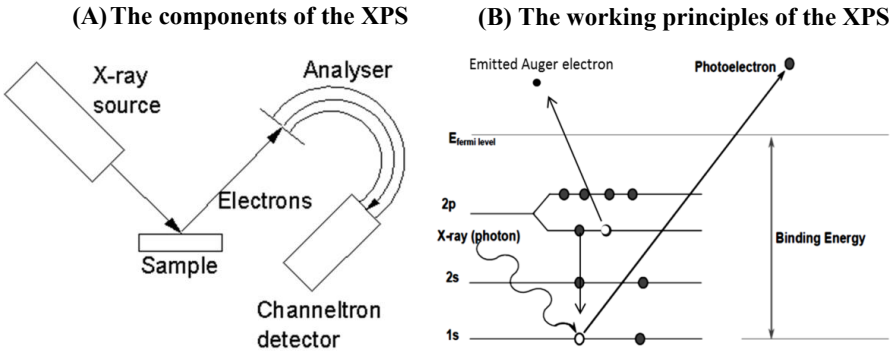

Figure 2.9 A) A schematic diagram of X-ray photoemission spectroscopy (XPS) apparatus. B) An overview of working principle of XPS.

2.3.4 X-ray Photoelectron Spectroscopy (XPS)

X-ray photoelectron spectroscopy (XPS) is a surface sensitive and widely used technique to obtain chemical information and the electronic state of various material surfaces. The components of a XPS are shown in figure 2.9A. When the X-ray beam is irradiated to the surface, electrons in the core-level of surface atoms are emitted from the surface. These photoelectrons will be collected to plot a spectrum of emission intensity versus electron binding energy. A simple example of the XPS process is schematically represented for the emission of one electron from the 1s shell (Figure 2.9B). The binding energies of the photoelectrons are characteristic for the element from which they are emitted, and therefore, the spectra can be used for chemical analysis of the surface.[104] Small shifts in the elemental binding energies provide additional information about the chemical state of the elements on the surface. However, XPS cannot identify hydrogen and helium elements because these are small atoms and electron emission does not take place.

2.3.5 Fluorescence Microscopy

Fluorescence microscope is a technique for acquiring an optical microscope that uses fluorescence to produce an image by illuminating the fluorescent species of on the sample and collecting the emitted fluorescent light to produce the image. The interest part of species on a sample can be stained using specific-affinity property of anti-body labelled fluorescent dyes. This allows the investigation of those parts of desired organelles or unique surface features on the same sample. The working principle of the fluorescence microscope is shown in Figure

(A) The working principle of the microscopy

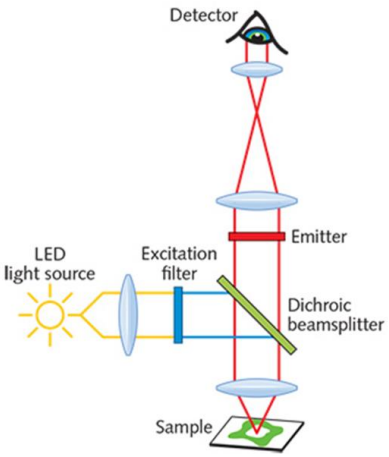

(B) A fluorescence image of a neuron

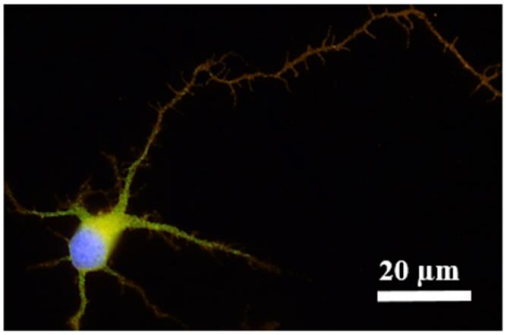

Figure 2.10 A) the working principle of a fluorescence microscopy. B) The fluorescence image of axon (orange), dendrites (green) and nucleus (blue) staining from a neuron.

2.10A. The light from a source will be passed to a filter to choose a desired wave-length light before excite the sample, which has been already labelled with fluorescent substance. The excitation light is absorbed by the fluorescent substance labelled in specimen and this fluorophore will emit light with a lower energy level compared to the excitation light. The emission light will be passed to a proper filter to a detector (camera or eyes directly) for obtaining the image. An example of the fluorescent image of a neuron is labelled with fluorescent chemicals for axon (orange), dendrites (green), and a nucleus (blue) (Figure 2.10B).

3. MATERIALS AND METHODS

In this section, all materials, instruments, and methods used for the experiments will be introduced. In the beginning, the step-by-step fabrication of AuNPs arrays and chemical modifications for the cell culture will be described. Ordered and disordered AuNPs of different sizes and densities synthesized by the block copolymer micelle nanolithography are introduced. The disordered AuNPs arrays are also prepared by directly immobilizing on the silicon substrate with different surface coupling strength. The atomic force microscopy, X-ray photoelectron spectroscopy, and electron scanning microscope are used to characterize the nanoplatforms. In the end, the cell culture and sample preparation for the fluorescent microscopy, scanning electron microscope, and focused ion beam cross-sections will be also described.

All molecules and chemicals were purchased and used in this thesis without further purification. MilliQ water with a resistance of 18.2 MΩ (Elix and MilliQ minipore system). Common use solvents such as absolute ethanol, 2-propanol, acetone, dried toluene (< 0.0005% H_2O) were purchased from the Merck Millipore Germany. Nitrogen with a purity of 99.8%, and silicon wafers (<100>, n-doped, 1-10 Ω cm, *Rms* ~0.147 nm) with a 100 nm top layer of SiO_2 were used throughout all the experiments.

3.1 Sample preparation for cell culture

3.1.1 Block copolymer micelle nanolithography

The block copolymer micelle nanolithography is employed to produce gold nanoparticles of different sizes, densities and distributions onto the silicon substrates (see section 2.2.1). The parameters such as the amount of polymer, the volume of toluene, the salt loading ratio and time for stirring were already optimized to make size-selective nanoparticles.[94, 105] Here, gold nanoparticles with sizes of from around 5 nm to 20 nm were produced by using diblockcopolymer, *polystyrene(x)-b-2-poly-vinylpyridine(y)* (*PS(x)-b-P2VP(y)*), which were purchased from the Polymer Source (Dorval, Canada). The number *x* and *y* are the molecular weight (MW) numbers of polystyrene (PS) and poly(2 vinylpyridine) (P2VP) respectively (see Table 3.1). A 7 ml glass vial (for containing the solution) with a plastic cap, plastic tweezers, a Teflon coated magnetic bar and other tools were carefully cleaned with toluene and dried with

$$Amount\ of\ salt = \frac{Polymer\ amount}{MW(PS)+MW(P2VP)}\ x\ \frac{MW(P2VP)}{MM(P2VP)}\ x\ MM(HAuCl_4)\ x\ LR$$

Equation 1: Amount of gold salt ($HAuCl_4$) to be added to the solution. The size of the formed nanoparticles can be adjusted by changing the loading ratio (LR) and the block length of P2VP block.

Table 3.1 Summary of micelle solutions prepared

Size (nm)	Polymer Amount (mg)	MW of PS (u)	MW of P2VP (u)	MM of P2VP (g/mol)	MM of $HAuCl_4$ (g/mol)	Loading ratio	Amount of $HAuCl_4$ calculated (mg)	Amount of $HAuCl_4$ added (mg)
4.5	25.1	32500	7800	105	339.79	0.5	7.86	7.9
10	24.9	44000	18500	105	339.79	0.7	19.35	19.8
14.7	24.98	185000	90000	105	339.79	0.6	16.07	16.5
19	25.25	185000	90000	105	339.79	0.9	25.56	25

nitrogen gas. Each micellar solution was prepared by adding 25 mg polymer to 5 ml toluene and magnetically stirred for at least three days to make sure the polymer was completely dissolved for the reverse micelles formation. Then gold salt, *HAuCl*$_4$, was added to each solution with pre-calculated amount corresponding to its loading ratio (calculated by Equation 1) and as shown in Table 3.1. A plastic spatula used to add the salt was cleaned with isopropanol and dried with nitrogen gas before use. The loaded solutions reached their equilibrium states after seven days of magnetic stirring.

In order to making disordered AuNPs, 5 mg of polystyrene (PS) with MW of 170.000 (Polymer Source, Dorval, Canada) was added to the micelle solution (after 3 days loading the gold precursor) and magnetically stirred for at least one day before using.

3.1.2 Nanoparticle immobilization of different surface coupling strength

The AuNP immobilization on silicon substrates with different surface coupling strength is illustrated in Figure 3.1. Following this approach, the citrate stabilized gold nanoparticles (cit-

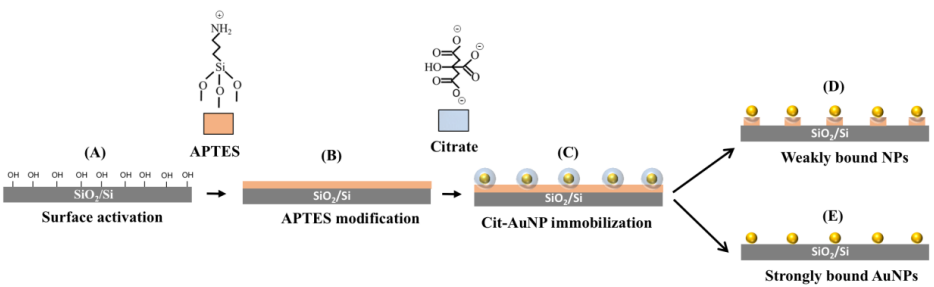

Figure 3.1 AuNPs immobilizations of different surface coupling strength. (A) Surface activation of the silicon substrate by oxygen plasma. (B) Attachment of APTES monolayer by salinization. (C) Decoration of the silicon surface with cit-AuNPs. The immobilized cit-AuNPs followed by 2 min plasma exposure for weakly bound (D) and 30 min plasma exposure for strongly (E) bound AuNPs.

AuNPs) of different sizes are tethered on silicon samples through an electrostatic immobilization process, which has been previously established at our lab.[24-25, 62] Briefly, silicon substrates were first successively cleaned with acetone and 2-isopropanol for 3 min in an ultrasonic bath (repeatedly 2 times for each step). The cleaned samples were then dried in a nitrogen stream and activated by oxygen plasma at 200 W, 1.4 mbar for 2 min (Pico, Electronic Diener plasma surface technology) (Figure 3.1A). The activated silicon wafers were then exposed to a vapour of 3- aminopropyltriethoxysilane (APTES, 99 % Sigma) in a glass desiccator (Argon air, 5 mbar, 1 hour) inside the glovebox (MB-200B Modular Glove Box Workstation**)** (Figure 3.1B). Thereafter, the APTES modified substrates were incubated into the colloidal citrate stabilized AuNPs **(**Cit-AuNPs) solutions with particle diameters of 5, 10, 20 (Sigmal-Aldrich), 30 and 50 nm (SPI) for 0.5, 1, 10, 30 and 60 min and overnight to obtained different particles densities. For the overnight incubation samples, the cit-AuNPs solutions were added with NaCl 1mM by 1:50 ratio to reduce the ionic strength of the solutions for obtaining higher particle density. The samples were finally rinsed by Milli-Q water and dried in a N_2 flow (Figure 3.1C). The citrate molecules surrounding the AuNPs were then removed by oxygen plasma etching with varying exposure times resulting in different particle binding conditions. The weakly bound (WB) particles were fabricated with a short oxygen plasma exposure of 2 minutes (Figure 3.1D). This short plasma treatment just partially decomposes the citrate molecules.[106] In order to obtain to obtain strongly bound (SB) particles, the samples were treated with an oxygen plasma for 30 min instead of the 2 min (Figure 3.1E).

3.1.3 Chemical modifications

Simultaneously, after WB and SB AuNPs were obtained by different oxygen plasma exposure (Figure 3.2A), the AuNP free areas of the SiO_2 surface were activated by the oxygen plasma for a subsequent attachment of cell aversive 2-[methoxyl(polyethyleneoxy)6-9-propyl] trichlorosilane **(**PEG silane) for passivation (5 µL of the PEG silane, obtained from Fluorochem, UK, in 5 mL toluene for 8 hour incubation) (Figure 3.2B). The samples were then thoroughly washed by clean toluene, and finally by absolute ethanol. In the last modification step, the AuNPs on the samples were modified with 1mM 11-amino-1-undecanethiol **(**AUT) molecules **(**ordered from Sigma-Aldrich) dissolved in the absolute ethanol overnight, and finally rinsing with pure ethanol (Figure 3.2C). The samples were then sterilized by UV light for 30 min inside the sterile bench (Heraeus) before seeding the cells.

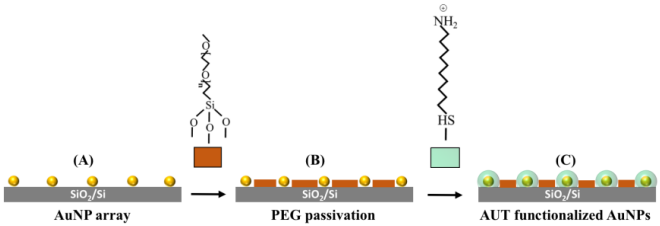

Figure 3.2 Surface chemical modifications of the nanostructured platform for the cell culture f. (A) AuNPs decorated SiO_2/Si substrates (both WB and SB coupling strength). (B) Attachment of PEG molecules on the silicon background for passivation. (C) AUT ligands are functionalized onto the AuNPs for the cell adhesion.

3.2 AuNP array and chemical modification characterizations

For investigating the nanostructure and surface chemical modifications, different characterization methods such as AFM, SEM, XPS have been performed. The densities and sizes of nanoparticle decorated substrates were characterized by SEM (Gemini 1555 (Leo/Zeiss_HNF) using an inlens detector mode or by the AFM (Nanoscope Multimode, Bruker) with the tapping mode. The AFM was also used to measure the change in average heights of AuNPs after each chemical modification step of the PEG passivation and AUT functionalization. The nanoparticle binding strengths were imaged and manipulated by AFM with the tapping mode by a high spring constant cantilever (200N/m, Bruker). The composition of the surface modification was characterized by XPS (PHI 5000 VersaProbe II, UL VAC-PHI) to prove the binding of AUT-AuNPs.

3.3 Cell culture and analyses

3.3.1 Neuron cultures

All animal experiments were carried out in accordance with the Landesumweltamt für Natur, Umwelt und Verbraucherschutz Nordrhein-Westfalen, Recklinghausen, Germany, approval number 84-02.04.2015.A173. Rat embryonic cortical neurons were prepared according to Brewer et al. [107] and Fricke et al. [108] The detailed protocol to prepare and culture the cells was discussed in our previous work. [24-25] Briefly, neurons were obtained by separating cortices from the embryonic brain of pregnant Wistar rat at 18 days gestation and immersed in Hank's Balance Salt Solution (HBSS) without calcium and magnesium for at least 3 minutes. The cortices were then mechanically dissociated by pipetting with a silanized Pasteur pipette. Subsequently, the cell suspension was diluted in HBSS with calcium and magnesium by 1:2 ration and left for at least 3 minutes on ice. The majority of glial cells and non-dispersed tissue attach to the calcium

and magnesium ions, which results precipitation at the bottom of the tube. The suspended neuron in upper layer were collected and centrifuged for 2 min at 200 g to separate the cell from the solution. Finally, the neuronal pellet was redispersed in neurobasal medium (Life Technologies) with ratios of 1% B27 (Life Technologies), 0.5mM L-glutamine and 50μg/ml gentamycin. For all experiments in this thesis, the obtained neurons were seeded with the density of 30,000 cells per cm^2 on the samples and the culture medium was exchanged after 1-3 hours of cell seeding. Cells were stored in incubator at 37^o C, 5% CO_2, and 100% humidity condition for the cell characterizations at 3^{rd} day in vitro (DIV3) culture.

3.3.2 Fluorescent microscopy

3.3.2.1 Live and dead staining

Cells were characterized by a fluorescence microscopy (ZEISS Axio Imager Z1, Zeiss) after three days of culture for visualizing live and dead cells. The cells were first stained with calcein (for live cells) and ethidium homodimer (for dead cells) in 1xPBS (1:1000 ratio) for 15 min under dark condition at RT. Images were recorded by an Axiocam XRm Cam (Zeiss) and processed using Zen 2012 (blue edition) and ImageJ software (version 1.50b). The cells and number of neurite were counted using the 'Analyze Particles' function and 'Cell Counter' plugin of ImageJ. The average axon length was measured by using the 'NeuronJ' plugin. Each data value was obtained from two or three different samples and the data recording was repeated for at least three times. All data were averaged and the standard error was determined as indicated in the respective graphs.

3.3.2.2 Immunostaining of nuclei, axons, dendrites, tubulin, actin, and vinculin

For the first steps of axon staining, cells were rinsed 2 times with pre-warmed PBS at 37^0 C, and fixed with 4% paraformaldehyde for 12 min at RT. The samples were then rinsed three times with PBS, and the cells were permeabilized in a blocking buffer (1% bovine serum albumin + 2 % goat serum in PBS) with 0.1% Triton X for 15 min at RT. The samples were rinsed three times with PBS and stored in the blocking buffer for 1 hour at RT. From these steps, the different fluorescent sustains can be used for labelling axon, dendrites, tubulin, and vinculin:

For dendrites and axons staining, the samples were incubated with a first antibody (Tau 1 mouse, Life Technologies) with a 1:200 concentration ratio in the blocking buffer solution for 1.5 hours. After rinsing three times with PBS, the samples were stored with a second antibody

(Alexa Fluor 546 anti-mouse, Life technologies) with 1:500 ratio, in the blocking buffer for 1.5 hours in dark condition at RT and then rinsed three times with PBS. In the next steps for dendrite staining, the samples were incubated with a second antibody (MAP2 Rabit, Life Technologies) with a 1:500 concentration ratio in the blocking buffer solution for 1.5 hours. After rinsing three times with PBS, the samples were stored with a second antibody (Alexa Fluor 488 anti-rabbit, Life Technologies) with 1:500 ratio, in the blocking buffer for 1.5 hours in dark condition at RT. In the meanwhile, cell nuclei were stained with 4',6-diamidino-2-phenylindole (DAPI) by adding a concentration of 1:500 to the second antibody solution.

For tubulin and vinculin staining, the samples were incubated with a first antibody (Anti beta tubulin antibody, Life Technologies) or monoclonal anti-vinculin antibody (Sigma) with a 1:200 concentration ratio in the blocking buffer solution for 1.5 hours. After rinsing three times with PBS, the samples were stored with a second antibody (Alexa Fluor 488 anti-mouse, Life technologies) with 1:500 ratio, Alexa Fluor 633 phalloidin (ThermoFisher Scientific) with 1:40 ratio, and dapi (Life Technologies) with 1:500 ratio together in the blocking buffer for 1.5 hours in dark condition at RT.

Finally, the samples were rinsed three times with PBS and imaged by the fluorescence microscopy with proper excited lights for each fluorescent chemical labelling. The fluorescent labelled samples can be also mounted on the glass coverslip for later characterizations.

3.3.3 Cell fixation for scanning electron microscopy (SEM) and focused ion beam (FIB) cross-sections

The cells were prepared for FIB cross-sections according to the following steps.[101, 109-110] In brief, samples were rinsed twice with pre-warmed PBS buffer (37^{o} C) and then incubated for fixing the cells in 3.2 % glutaraldehyde for 15 min. Samples were rinsed twice with PBS at RT and followed by 5 times washing with milliQ water or cacodylate buffer. For enhancing the contrast of internal cellular structures, the samples were then stained with 1% osimum tetraoxide (OsO4) (obtained from Sigma-Aldrich) in cacodylate buffer for 2 hours on ice. After rinsing 5 times with milliQ (2 min for each step), the samples were incubated in 1% Tannic acid diluted in milliQ for 30 min at RT and then washing 5 time with milliQ (2 min for each step). The samples were continued to stain by 2% uranyl acetate for 5 hours at 4° C and then washed 5 times with milliQ (2 mins for each step). The samples were then subsequently immersed in increasing concentrations of ethanol (10 % for 5 min, 30 % for 5 min, 50 % for 5 min, 70 % for

15 min, 90 % for 7,5 min by 2 times, and 95 % for 7,5 min for 2 times) and stored in 100 % ethanol for the next steps. The absolute ethanol (EtOH) on the cells was then step by step exchanged by epoxyl resin (a mixture of epoxyl embedding medium epon 812, epon hardener DDSA, epoxyl embedding medium hardener MNA, tris(dimethylamino)phenol 95 %-DMP-30, all ordered from Sigma). The samples were subsequently immersed in solutions of EtOH: resin (3:1) for 3 hours, EtOH:resin (2:1) for 3 hours, EtOH:resin (1:1) for overnight, EtOH:resin (1:2) for 3 hours, EtOH:resin (1:3) for 3 hours, and in resin for 3 hours. The resin on the surface of the samples was carefully rinsed by flushing EtOH over the samples. Finally, the samples were dried in an oven at 60^{o}C overnight. Then, each sample was mounted on a typical electron microscopy stub using liquid silver glue. A thin layer of iridium (approximately few nanometer) was sputtered (15–30 s deposition time, 15 mA current) *via* sputtering device (K575X Sputter Coater, Quorum EMITECH, Lewes, United Kingdom) onto the samples for imaging in SEM or FIB. The FIB cross-sections of cells were performed by a Helios Nanolab 600i apparatus (FEI, USA). Before cutting, the cells were sputtered in a 1 µm thick platinum layer and cut in a Ga-ion beam with a current of 2.5 nA and an acceleration voltage of 30 kV. For each cut, the tangent surface of the cell was polished by a lower current of 21 pA to clearly visualize the internalized NPs.

3.4 Cytotoxic investigations

In order to investigate the cytotoxic effects of the WB AuNPs, 5, 10, 20 nm AuNPs of different particle densities were decorated on silicon substrates by the incubation times of 1, 10, 30 and 60 mins (see method 3.1.2) for both WB and SB. For comparing the cytotoxic effects between WB and colloidal AuNPs, the SB 5, 10 and 20 nm AuNP arrays with densities of 234, 268, and 240 particles/ µm^2 respectively were prepared as the substrates for experiments. Laminin coated silicon substrates were also used as control samples. The silicon substrates were first cleaned with acetone, isopropanol, before rinsing with milliQ and drying by a nitrogen gun. The substrates were treated by oxygen plasma (2 min, 200W, 1.4 mBar) and sterilized in 70% Ethanol solution for 30 min, and then immersing in 10 µl laminin (Sigma-Aldrich) diluted in 10 ml Grey's buffer salt solution (GBSS) (Thermo Fisher Scientific).

The AUT-AuNPs with concentrations of 4.7 x 10^{12}, 1.5 x 10^{11}, and 1.9 x 10^{10} particles per µl for 5 nm, 10 nm, and 20 nm AuNPs respectively were synthesized as previously reported by Kaulen et al.[111-112] Briefly, glass beads (1-1.3 mm, Carl Roth GmbH + Co. KG) were silanized

with APTES according to a procedure reported by Nath et al.[112] 2.5 g of silanized glass beads were washed once with 1 mL of water, then 2 mL cit-AuNP (5 nm, 10 nm, and 20 nm) were added. The glass beads were incubated overnight, the liquid phase was removed and the beads were rinsed 3 times with water. Successful immobilization of the AuNP was evident by a color change of the glass beads from colorless (before immobilization) to red (after immobilization). Upon addition of 1mL water, 50 µL AUT (2 mM solution in ethanol and 50 µL HCl (0.1 M) and subsequent sonication ligand exchange occurred and the formed AUT-AuNPs were released from the solid support. The AuNP dispersion was removed from the glass beads and allowed to stand for two hours to ensure complete formation of an AUT coat on the particles surface. The AUT-AuNPs were further purified three times by centrifugation and redispersion in acidified water. After the last centrifugation step, the supernatant was removed and the concentrated AUT-AuNP pellet was used for cell tests.

The dispersed AUT-AuNPs of different sizes were added to the culture medium of the same particle size samples after the medium exchange with the volume of 1.5 µl, 5 µL, and 20 µL for 5 nm, 10 nm, and 20 nm particles respectively. A same volume of each colloidal AUT-AuNPs were also added to the laminin coated control samples.

3.5 Cell culture with endoneuraminidase (endo-N) enzyme adding

20nm ordered AuNP arrays with a density of 90 particles/ μm^2 per were prepared by the micelle nanolithography as nanostructure platforms for this experiment. The AUT functionalization steps were followed the protocol described in part 3.2.3. In in study, the specific cell adhesion ligand of PA22 was used as the control samples. For the PA22 functionalization of AuNPs, 150 µl PA22 peptide in water (100 µg/ml) was dropped on the AuNP array for overnight at 4^o C. The samples were then rinsed with milliQ and dried by a nitrogen gun. The laminin coated silicon samples were also used as the specific cell adhesion control samples. The endoneuraminidase (endo-N) enzyme (200 mg/mL, obtained from the ABC Scientific) was diluted in the neurobasal culture medium with a ratio of 1:1000 ratio (3.5 U/mL) immediately after cell seeding.

4. RESULTS AND DISCUSSIONS

As mentioned in the fundamental part of this thesis, cell adhesion plays a pivotal role in determining the cell development and survival. Therefore, the ability to control the behaviour of cells that interact with non-biomaterials is desirable for the success of a variety of biotechnological applications such as biomedical implants. The growing knowledge of surface coatings has allowed not only the control of cellular adhesion but also the regulation of cell morphogenesis through surface mediated signalling pathways.[113-115] Control of the cell adhesion can be performed by tuning chemical compositions, which induce interactions between cell membrane and the synthetic surface.[24, 62, 116] In this thesis, following our preliminary results,[23-24, 62] metal nanoparticles especially AuNPs have been used as surface chemical cues to control the adhesion of neurons in vitro cultures. Besides the chemical effects, the other parameters such as the particle size, density, distribution and surface coupling strength have been also thoroughly investigated to better understand how neurons response to the non-biomaterials at sub-50 nm nanoscales.

In the first part of this section, AuNPs decorated on Si/SiO_2 substrates with particle variations of sub-50 nm sizes, densities, distributions, and surface coupling strengths are fabricated to be used as nanoplatforms for studying neuron adhesion and neuritogenesis. Surface chemical modifications of chemical ligands for cell adhesion and background passivation are performed. Moreover, different characterization techniques such as AFM, SEM, FIB, XPS and fluorescent microscopy are utilized to investigate the nanoplatforms.

In the second section, the influence of surface topography and chemical ligand density on neuron adhesion and neurite outgrowth are evaluated by weakly bound (WB) AuNPs of different sizes and densities. The amount of chemical ligand on the surface can be precisely controlled by a define particle size and density. A bigger particle size possesses a higher capacity of ligand binding, which is a spare proportional to the particle size. The dependence of cell survival, neurite number, and axon outgrowth are statistically quantified by the influences of not only the nanotopography in sub-50 nm AuNPs, but also the surface chemical ligand density.

In the next section, cytotoxic effects of the WB AuNPs are investigated as function of different particle sizes, densities, and surface coupling strengths. The cell survival is compared between cells cultured on the WB and strongly bound (SB) AuNP arrays to evaluate the cytotoxic effects. Importantly, the cytotoxic effects of the WB AuNPs are also compared with the colloidal AuNPs of the same size and ligand, but dispersing in culture medium. Besides the cytotoxic effects on the cell survival, the influence of the WB and SB particle coupling strengths on axon outgrowth is characterized for different particle sizes and densities.

Another parameter of the AuNPs array, which could affect the cell adhesion is discussed here, namely particle distributions. The block copolymer micelle nanolithography allows synthesizing both highly ordered and disordered AuNP arrays on the substrates. Once again, the cell survival and neurite outgrowth dependence on the particle sizes and densities are characterized, but for the different particle distributions of ordered and disordered AuNPs.

Moreover, the neuron adhesion is supposed to be mainly mediated by the unspecific electrostatic interactions between the negatively charged glycocalyx integral membrane NCAM and the positively charged AUT ligands immobilized on the AuNP array. Thus, the cell adhesion would be interrupted by using a specifically selective enzyme to remove the negative charge of glycocalyx elements from the NCAM. The cell survival is quantified and compared between the cells cultured in medium with and without adding the enzyme for different type of adhesion cues (AUT, PA22, and laminin).

Since neurons in the brain form a complex and directed network by billions of cells and much higher number of synaptic connections, local control of neuron adhesion and neurite guidance on biochemical patterns is essential for development of artificial neuronal network. Instead of using AuNPs array, in this thesis, positively charged ferritin nanoparticle patterns are fabricated on the silicon substrate for controlling the neuron adhesion and guiding neurite outgrowth. Moreover, the ferritin nanoparticles can be loaded with different metal (magnetic) nanoparticles, which allows possibly to control the cell adhesion by advanced methods such as externally magnetic fields.

4.1 Nanoparticle array preparation and characterizations

Nanoparticles, especially AuNPs are commonly used as nanomaterials for biotechnological and biomedical applications due to their good biocompatibility, easy synthesis, and simple surface chemical functionalization (capabilities high gold-thiol affinity). Our preliminary results have

shown that AuNPs can be used for tuning neuron adhesion.[24, 61-62] The usage of AuNPs to control the cell adhesion in terms of surface chemistry have some important advantages: the cell adhesive cues (ligands), which support the cell adhesion, can be easily immobilized on the sample surface through chemically functionalized AuNPs. Thus, the number of ligands on the surface can be well controlled. Moreover, other important parameters such as particles sizes, densities, distributions, and surface binding strengths can be regulated by the methods used for particle immobilization.

Thanks to self-assemble nanofabrication methods, in this thesis AuNPs of different sizes, inter-particle distances, distributions and surface binding strengths are prepared on substrates for studying neuron in-vitro cultures. Therefore, AuNPs have been functionalized by with 11-amino-1-undecanethiol (AUT) as cell adhesion ligands, while the background is passivated by 2-[methoxyl(polyethyleneoxy) 6-9-propyl] trichlorosilane (PEG silane), a cell aversive molecule, which prevents undesired cell adhesion.

4.1.1 AuNP synthesis by the block copolymer micelle nanolithography method

The block copolymer micelle nanolithography is a bottom-up, self-assembly method utilized for nanofabrication. This technique employs intrinsically chemical or physical forces which operate at the nanoscale to assemble basic units into larger structures.[26-28, 96] Using this method, AuNPs of different sizes, inter-particle distances (densities), and orders are synthesized and bound onto SiO_2 substrates. Highly ordered AuNP of 5 nm, 10 nm, and 20 nm are synthesized by using the PS(30.000)-b-P2VP(8.500), PS(44.000)-b-P2VP(18.500), and PS(175.000)-b-P2VP(70.000) block copolymer micelle solutions respectively, whereas the inter-particle distances (densities) are tuned by changing the dip-coating speed from 3 to 21 mm/s (see method section 3.2.1). The ordered AuNPs of different sizes and densities are prepared by using the different block copolymers and varying the dip-coating speed in the respective micellar colloidal solutions (Table 4.1). Since the samples are dip-coated from a toluene based solution, the drying speed of toluene can affect the particle arrangements. The self-assemble arrangement of densely packed colloidal micelles on the substrate is affected by long-range van der Waals interactions and capillary forces between the micelles during the evaporation of the solvent onto the substrate surface. Faster speeds of withdrawing sample from the colloidal micelle solvent result in closer packed particle coverage of the surface.[29] The highly well-ordered arrangement (hexagonal order) of nanoparticles can be optimized by choosing a proper dip-coating speed

Table 4.1 Ordered AuNPs of different sizes and densities synthesized on SiO_2 substrates.

Size (nm)	Particle density (particles /μm^2) of different dip-coating speed (mm /s).			
	3	**9**	**15**	**21**
4.5 ± 0.7	453 ± 28	1029 ± 97	1093 ± 58	1232 ± 53
11 ± 1.4	180 ± 16	300 ± 21	396 ± 46	444 ± 42
19 ± 2.7	29 ± 2	56 ± 4	73 ± 4	92 ± 6

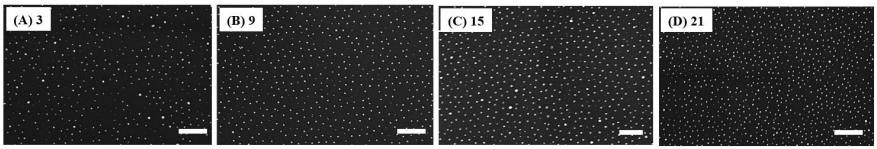

Figure 4.1. The SEM images of the highly ordered 20 nm AuNPs with different densities obtained by varying dip-coating speed of 3 mm /s (A), 9 mm /s (B), 15 mm /s (C), and 21 mm /s (D). Scale bar: 200 nm.

depending on the polymers use[95]. Although, verifying the dip-coating speed results in different particle densities (or inter-particle distances), the hexagonal order of AuNPs could be also affected to a certain extent. The SEM images of 20 nm AuNPs with different densities are obtained by changing the dip-coating speed as shown in Figure 4.1. The AFM characterizations of all particle sizes and densities are obtained by changing the dip-coating speeds from 3 to 21 mm/s (Figure A4.1; Appendix B). An optimal dip-coating range from 9 to 15 mm/s for obtaining the highly well-ordered arrangement can be observed for the 20 nm AuNPs. For examples, the highly hexagonally ordered arrangements of the AuNP array obtained after plasma etching from the respective dip-coated colloidal micelles are indicated by using the autocorrelation transformation as shown in the inset image at the corners in Figure 4.2.

On the other hand, disordered AuNP arrays can be also synthesized by this block copolymer micelle nanolithography method. After gold precursor is loaded to the colloidal

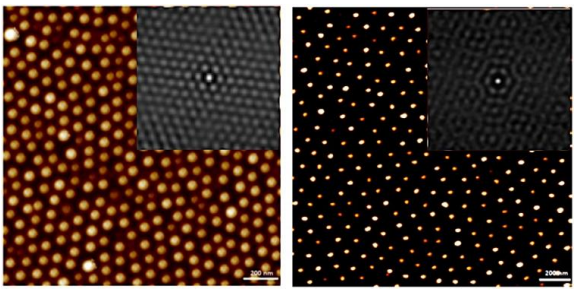

Figure 4.2. The AFM images of dip-coated micelles (right) and their respective 20 nm AuNPs (left). The Fourier spectrum obtained by 2D-autocorrelation of the AFM images indicate the highly hexagonal order of particle arrangements as shown by the inset square image at respective corner. Scale bar: 200 nm.

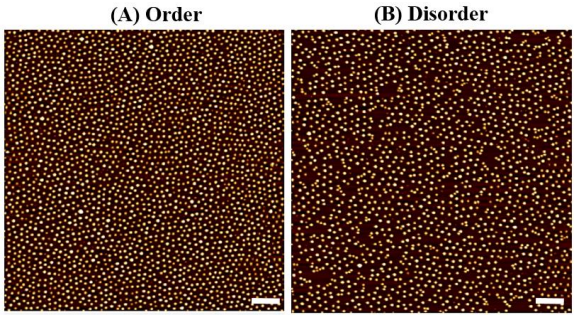

Figure 4.3. The AFM images of 10 nm AuNPs with highly well-order (A) without and disorder (B) with adding the PS polymer. The Fourier spectrum obtained by 2D-autocorrelation of the AFM images indicated the difference in particle arrangements, as shown by the inset square image at respective corner. Scale bar: 300 nm.

micelles, another hydrophobic polymer of PS (170.000) is added into the micelle solvent (see method section 3.2.1). The added PS polymer interrupts the originally hexagonal order of the micelles during the dip-coating step.[14] The amount of PS polymer is experimentally calculated to be enough for creating the disorder, but avoiding the aggregations of the colloidal micelle

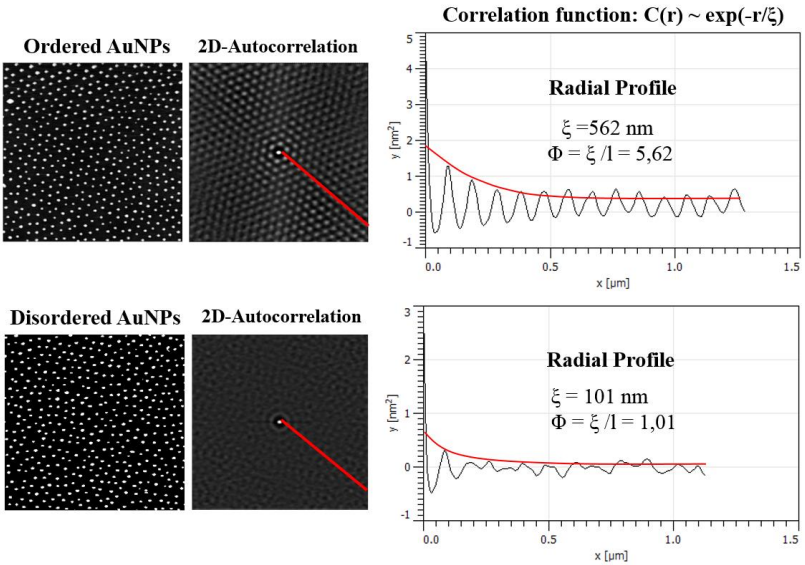

Figure 4.4 Autocorrelation spectra of AFM images (2x2 μm^2) for ordered and disordered 10 nm AuNPs. The periodic distribution of ordered AuNP array is extracted from the radial profiles of the corresponding autocorrelation spectra with the lateral correlation length (ξ), the number of unit repeats (Φ), and the average inter-particle distance (l).

solvent. The existence of the PS polymer in the colloidal micelle solvent obviously disrupts the order of the AuNPs as shown in the AFM images of 10 nm AuNPs obtained by a dip-coating speed at 15 mm/s (Figure 4.3).

By using the Gwyddion[117] or Nanoscope Analysis software[118], important parameters such as the size, the inter-particle distance, the order of the particles can be determined. In order to quantitatively evaluate the degree of order in AuNP arrays, 2D-autocorrelation spectra are created for the AFM images of the above 10 nm ordered and disordered AuNPs (2 x 2 μm^2 in scan size). From these spectra, radial profiles[119-120] can be extracted to characterize geometrical arrangement of the two AuNP arrays as shown in Figure 4.4. The radial profile is fitted to the correlation function allowing the extraction of the correlation length ξ with r, the distance measured on the autocorrelation profile (in nm). When the average distance of AuNPs is measured, the number of unit repeat, φ could be calculated, which quantitatively proves the degree of the AuNP order for each array. From this quantitative investigation of the particle arrangement, the periodic distribution of ordered AuNP arrays (ξ = 562 nm, φ = 5.62) is extracted to be more than five times higher than the distribution of disordered AuNP array (ξ = 101 nm, φ = 1.01).

4.1.2 AuNPs immobilization with different surface coupling strength.

Beside from the direct synthesis of AuNPs on surfaces as the aforementioned block copolymer micelle nanolithography, arrays of AuNPs can be also prepared by immobilizing colloidal AuNPs on the surface. Usually, the anchoring of AuNPs on the solid substrates was performed by using intermediate linker of organic molecules functionalized on the surfaces, in which, their terminal functional groups were designed for physical or chemical interactions. [121-123] Using one common method from these approaches, negatively charged citrate-stabilized AuNPs (cit-AuNPs) could be attached to the silicon surface through a self-assembly on a of 3-aminipropyltriethoxysilane (APTES) coated surface.[121] This AuNPs immobilization had been investigated and optimized for different particle sizes and densities in our preliminary experiments.[23-24]

In this thesis, not only the particle size and were varied, but also the particle surface coupling strength of AuNPs is controlled for more comprehensive neuronal adhesion studies. To study the influence of the surface binding strength of AuNP on neuron adhesion, weakly bound (WB) AuNPs are firstly decorated on the substrate with different particle sizes and

densities.[61] Thus, 5, 10 nm, 20 nm, 30 nm, and 50 nm cit-AuNPs are decorated with different densities by varying the sample incubation time in the respective colloidal particle solution (see method section 3.2.2). The SEM images of the lowest and highest particle density for 5 nm, 10 nm, 20 nm, 30 nm and 50 nm AuNPs are shown in Figure 4.5 (a full set of all particle sizes and densities are shown in the (Figure A4.2; Appendix B).

It is found that the electrostatic immobilization of 5 nm and 10 nm AuNPs is much faster than for the bigger particle sizes of 20 nm, 30 nm, and 50 nm AuNPs. This can be explained by different binding kinetics and ionic strength of each AuNP solution.[121] The negatively charged cit-AuNPs are surrounded by an electrical double layer of positive ions, which is based upon repulsive interactions to keep individual AuNP stable in the colloidal solution. A difference in the thickness of the double layer directly changes the electrostatic repulsion and thus the interparticle distance (density).[124-126] Moreover, P.Li studied the kinetics of AuNPs binding to the substrates for the same system in her work.[23] In accordance with previous work, the binding kinetics of the AuNPs depends on the incubation time also in this study. The density of 20 nm AuNPs, for example increases steeply during the first hour of incubation and gradually reaches a saturation state after few hour incubation.[23] The detail densities of all particle sizes are prepared by varying the sample incubation time in the respective colloidal particle solution, as shown in Table 4.2.

More importantly, the surface coupling strength of 5 nm, 10 nm, and 20 nm AuNPs on the sample surface could be controlled by changing oxygen plasma treatment after the AuNPs are immobilized on the substrate. A short plasma treatment of 2 min results weakly bound (WB)

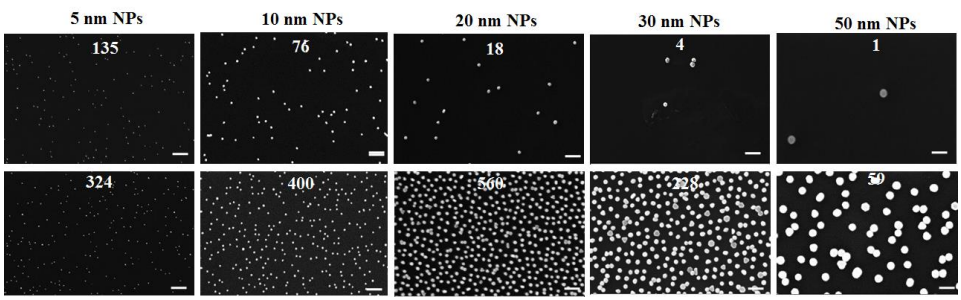

Figure 4.5 SEM images of SiO_2 surfaces decorated with AuNPs of different sizes (nm) and densities (particles per μm^2). The lowest (top row images) and highest densities (bottom row images) are obtained for 5 nm, 10 nm, 20 nm, 30 nm and 50 nm AuNPs by changing the incubation time. The number in each image indicates the particle density /μm^2 (the full densities of all AuNPs are shown in Table 4.2). Scale bar: 100 nm.

Table 4.2 WB disordered AuNPs of different sizes and densities immobilized on SiO_2 substrates.

Size (nm)	Particle density (particles /μm^2) obtained by different incubation time (min). Error bar is standard error (SE)				
	0.5	**1**	**10**	**60**	**Overnight**
5	135 ± 4	173 ± 4	225 ± 3	239 ± 8	324 ± 16
10	76 ± 5	208 ± 4	258 ± 6	268 ± 15	400 ± 32
20	18 ± 1	49 ± 6	98 ± 7	240 ± 12	560 ± 46
30	4 ± 1.3	39 ± 3.4	78 ± 4	115 ± 7	228 ± 10
50	1 ± 0.3	4 ± 1.2	11 ± 2.3	25 ± 2.7	59 ± 3.3

AuNPs on the surfce, while a longer plasma treatment of 30 min allows obtaining surface strongly bound (SB) AuNPs. After 2 min plasma treatment, the attachment of AuNPs to the SiO_2 surface occurred via electrostatic binding between negative charges of cit-AuNPs and positive charges of the amino groups of the APTES molecules. It is assumed that only freely exposed APTES molecules on the oxide layer and exposed citrate molecules surrounding the AuNPs are removed during the short 2 min plasma treatment, while molecules underneath the particles are conserved and maintain the particle binding.[106] If the 30-min plasma is applied, the AuNPs binding would convert from the electrostatic adsorption to the contact attachment to the oxide layer. Moreover, it has been reported that AuNPs have catalytic properties, which can be activated by oxygen plasma.[127-129] The process of gold oxidation during long time plasma activation enhances the attachment of AuNPs on the silicon surface in agreement with the observation of Xu et al.[128] However, the detail mechanism behind how oxygen plasma enhances the attachment of the AuNPs on the silicon surface is still not fully elucidated and need further studies.

4.1.3 Particle binding strength characterizations

It is found that the duration of the plasma treatment after cit-AuNP immobilization influences the particle binding strength. A first indication of a different binding strength for both the 2 min and 30 min plasma treatments can be derived from a simple sonication and washing procedure applied to the particle-modified samples (Figure A4.3; Appendix B). Specifically, for the AuNPs of 5, 10, and 20 nm in size, they are observed well distributed and less aggregated particles for 30 min plasma treatment in contrast to the 2-min plasma treatment.

To characterize differences between the two types of NP binding, the AuNPs can be manipulated by an AFM tip.[130-131] Both long and short plasma treated 10 nm AuNPs are actuated

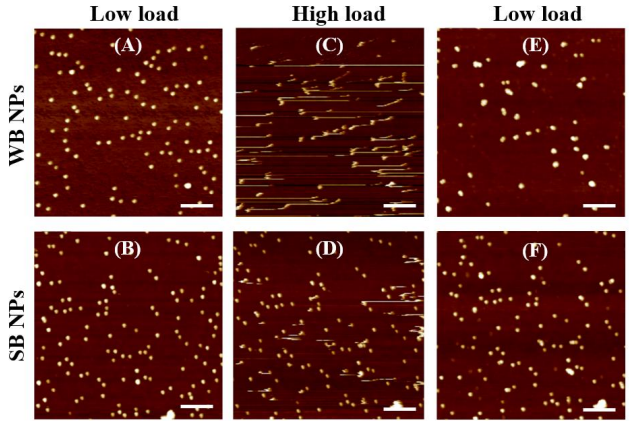

Figure 4.6 Characterization of the AuNP binding strengths. (A-F) show AFM images of 10 nm AuNPs for both weak (WB) and strong binding (SB) strengths. (A, B) Low load scan with a setpoint amplitude difference, ΔS of 50 mV, (C, D) high load scan with a higher ΔS of 380 mV, (E, F) and a final low load scan for the evaluation of particle displacement. Scale bar: 200 nm.

by adjusting the tip-sample loading forces under ambient conditions with the same AFM tip (Figure 4.6). The tapping AFM in the repulsion mode is used to image the surface by a cantilever with a spring constant of 200 N/m. First, the AuNP densities is determined by a low load scan with an amplitude setpoint difference ΔS of 50 mV (an initial amplitude setpoint is set to a value of about 400 mV after the tip engagement) without displacing the AuNPs by the AFM tip, (Figure 4.6A, B). When ΔS increases, the load between sample and tip increases. If the force applied via the tip is bigger than the binding strength of the AuNPs to the substrate, the AuNPs start moving. Particle trajectories can be observed, which are caused by shifting AuNPs when the amplitude setpoint is significantly lowered down to 20 mV (an amplitude setpoint difference ΔS of 380 mV), (Figure 4.6C, D). It can be seen that mainly AuNPs after short plasma treatment times are moved during scanning with high load. In contrast, only few particles are displaced for samples after long plasma treatment. This observation indicates differences in the binding strengths for both types of treated AuNPs. The shortly treated AuNPs can be easier displaced than AuNPs that experienced a long plasma treatment. Figure 4.6E, F show control images of AuNPs recorded with amplitude setpoint difference ΔS of 50 mV after scanning with high load. Various shortly plasma treated AuNPs are removed and most particles change their original positions, while the positions of long plasma treated AuNPs are almost preserved. The number

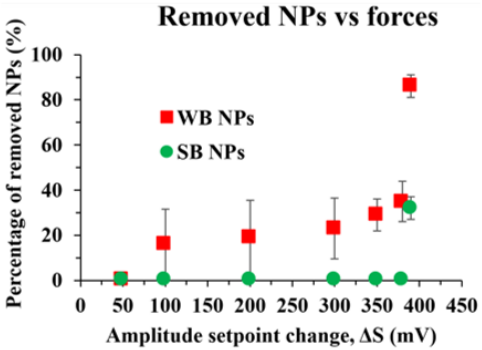

Figure. 4.7 The percentage of removed particles presented as a function of the amplitude setpoint difference, ΔS (mV). (two experiments are repeated by a same AFM tip for two separate samples, N=2; and variation shown by standard error, SE).

of particles that have been removed during scanning while the load is increased by decreasing the amplitude setpoint for both binding strength particles, (Figure 4.7).

Increasing ΔS by reducing the setpoint step by step from 350 mV down to 10 mV leads to a considerable detachment of shortly plasma treated AuNPs already at relatively low amplitude setpoint differences (low loads), which becomes even stronger for higher setpoint differences (high loads). In contrast, almost all long plasma treated AuNPs remain at their original position until the amplitude setpoint becomes smaller than 50 mV. From this analysis, we can indirectly confirm that the binding strengths of particles after long plasma treatment to the substrate are significantly higher than of the shortly activated particles. Therefore, we consider the samples after 2 min plasma treatment as weakly bound (WB) particles, whereas the long plasma treatment leads to strongly bound (SB) particles.

4.1.4 Chemical surface modifications and characterizations

As our aforementioned motivation, AuNPs are used as a tool to regulate surface chemical compositions of the substrates for controlling neuron adhesion and neuritogenesis. Thus, surface chemistry is utilized to functionalize the AuNPs with cell adhesive ligands of AUT. The use of the AUT ligands have been obviously confirmed to enhance neuronal adhesion from the previous work by Gilles at al.[62] and Li at al.[23-24] Here, the cell adhesion is chemically mediated by the electrostatic interaction between the positively charged amino terminal groups of the AUTs and the negatively charged molecules on the cell surface. Although the process of cell adhesion involves the arrangements of cell surface molecules, it is considered as non-specific

cell adhesion as mentioned in the fundamental section. From biological observation of cell culture and the quantitative characterization by XPS, Li has shown in her work, the AUT ligands are firmly attached to the AuNPs.[24] Compared to this work, although the same method is used to immobilize the AuNPs on the silicon substrates, the strongly bound (SB) AuNPs are etched by oxygen plasma for 30 mins[61] instead of 2 min as in Li's work. Moreover, it has been reported that gold can be oxidized by oxygen plasma exposure, [129, 132-133] so that longer time etching the cit-AuNPs with oxygen plasma may influence the attachment of AUT-AuNPs. To quantitatively confirm, the attachment of the AUT to AuNPs, the chemical composition of the particle-decorated surfaces is characterized by X-ray photoelectron spectroscopy (XPS). Therefore, the samples of the SB 20 nm-AuNPs (30 min plasma treatment) with a surface coverage of about 16 % are prepared for this characterization. The XPS results indicate an increase of C and O as well as the occurrence of N and S atoms at the sample surface after AuNPs are modified by the AUT in comparison to samples with the bare AuNP indicating the successful attachment of the amino alkyl thiols (Table 4.3). The amount of N and S is relatively low as only a small part of the surface is covered with AuNP where AUT can bind. The Au signal decreased after AUT binding due to the formation of a molecular layer on the AuNPs attenuating the gold signal. The observed XPS data are in good agreement with similar investigation for AuNP decorated surfaces after 2 min oxygen plasma treatment and AUT modification.[24] This proves that the duration of the plasma treatment does not influence the attachment of the thiol-ligands to the AuNPs. This XPS characterization of the AUT attachment on AuNPs via gold-thiol bounds is also consistent to observation from other previous research, in which AuNPs are also similarly exposed in oxygen plasma.[1, 14, 95]

In order to control the neuron adhesion on substrates, the passivation of the background also plays an indispensable role in preventing the non-desired cell adhesion. It has been proven that the silicon oxide surface can support the cell adhesion.[25, 134-136] Thus, the PEG silane, a cell

Table 4.3 XPS analysis in atom percent of AuNPs after 30 min oxygen plasma treatment and AUT modification.

	Element [%]					
	Au	**C**	**N**	**S**	**Si**	**O**
AuNPs	8.7	6.2	0	0	60.5	24.6
AUT-modified AuNPs	5.3	22.5	1.1	0.8	28.6	41.7

aversive molecule, is applied on the surface for passivating the particle free-area background. The common use of PEG for background passivation in cell culture has been reported from many groups.[1, 14, 88-89, 91, 137] P.Li et al.[24] have thoroughly investigated the essential role of background passivation by different backfill molecules such as the PEG or octyltrichlorosilane (OTS). An important role of the PEG backfill on controlling the neuronal adhesion will be also confirmed in the next section of this thesis.

To affirm the attachment of the PEG molecules applied on the silicon surface, contact angle (CA) and XPS measurements had been performed previously.[23-24] In this work, the attachment of PEG and AUT molecules on AuNPs can be also qualitatively proven by AFM imaging the AuNPs after each modification step. SB AuNPs with the size of approx. 15 nm are synthesized on the silicon substrate by using the block copolymer micelle method. The AFM images characterize the average height of AuNPs of the same sample which indicates a decrease of 1.96 nm height after the PEG binding to the background, while the height increases by 2.76 nm when the AUT is attached to the AuNPs, (Figure 4.8). These relative changes in the averaged AuNP height after each chemical modification step together with the XPS data (Table 4.3) prove the success of the PEG passivation and subsequent AUT-AuNP attachments.

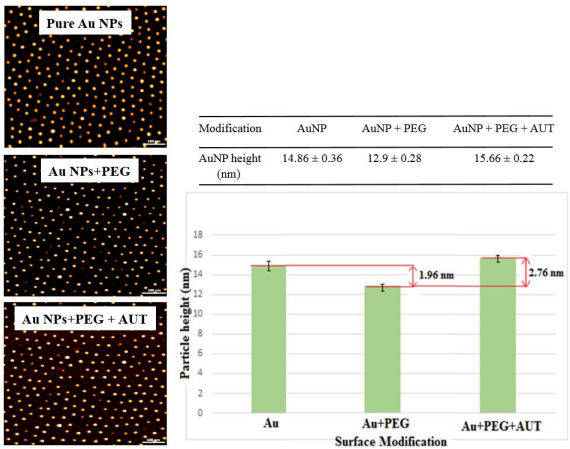

Figure 4.8 The average heights (particle sizes) of ~15 nm AuNPs are measured by AFM images after each step of surface chemical modification of PEG passivation and AUT attachment (The average heights of particles are taken from particles in three different areas, N=30; the variations shown by standard error, SE).

4.2 Influence of ligand and backfill on neuron adhesion

As aforementioned description in the sample preparation section 4.1, AuNPs are mainly used to control the chemical composition on surface for studying neuron adhesion. For this purpose, AuNPs are functionalized by the AUT ligand as the cell adherent cue via the gold-thiol binding, whereas the background is passivated with the PEG molecules. The adhesion of cells to the substrates has been reported to be mediated by the unspecific electrostatic interaction between the positively charged AUT and the negatively charged glycocalyx associated cell receptors.[23-25] To study the influence of surface charge density on neuron adhesion, the surface composition on nanometer scale is controlled by using AuNPs of different sizes and densities. For the same NP size, the increasing AuNP density leads to an increase of the number of particle associated adhesion molecules (AUT), which supports the cell adhesion. The number of AUT molecules bound to the AuNP surface can be estimated from the density of thiol containing SAM-molecules on AuNP of about 4.5 molecules per nm^2 determined by Kaulen et al.[111] If we take only the upper, solution exposed hemisphere of the AuNP (semi-particle) into consideration, then the total number of AUT molecules for each particle size can be calculated. Both, increasing particle size and particle density lead to an increase of the ligand density by more than one order of magnitude. Moreover, the use of the PEG backfill plays an essential role for controlling the cell adhesion or cell guiding as well as studied before.[24] The indispensable role of the backfill is clearly confirmed again in this work (Figure 4.9). Here, neurons are cultured on two series of ordered 20nm AuNPs of different particle densities (prepared by a same protocol) for both cases of with and without PEG passivation. The fluorescent microscope images of live (green) and dead (red) cells are recorded after 3 days of in-vitro culture (DIV-3), Figure 4.9A. The number of live cells per mm^2 are statistically quantified (Figure 4.9B). In case of applied backfill, the dependence of live cells on particle density can be observed, in which the number of adherent cells increases with the increase of particle densities. In contrast, the non-backfill samples show a different behavior. Although the number of adherent cells for this case is generally noticeable higher than those of the backfilled samples, a clear dependence of the cell number on the particle density cannot be seen. Possible explanation is that also the bare

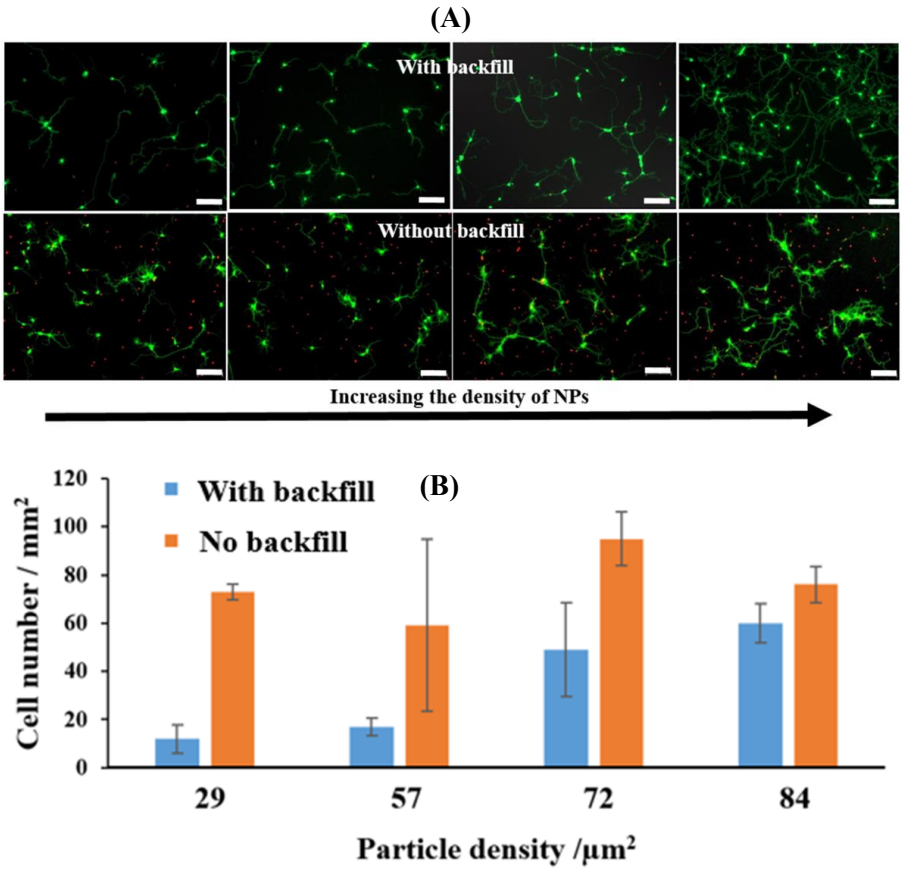

Figure 4.9 A) DIV3 neurons cultured on AUT functionalized 20 nm AuNPs of different densities with and without PEG passivation (scale bar: 100µm). B) The statistical quantification of live cell number on different particle densities of 29, 57, 74, and 84 particles per μm^2 (experiment is repeated at least three times, N=6; the variations shown by standard error, SE).

silicon dioxide (SiO_2) surface can support the neuron adhesion. In fact, it has been reported that silicon substrates can facilitate cell adhesion.[135-136, 138] The SiO_2 layer on the substrate possesses the negative charge, which enables the positive ions in culture medium to absorb onto the surface. This adsorption layer of surface acts as additional adherent cue for the neuron adhesion. In the case of backfilling, the increase of the live cell with the particle density is exclusively due to the increased number of cell adherent ligands. This observation is also consistent with the previous finding.[23] It is obviously known that the PEG backfill is a cell aversive molecule,

which prevents the attachment of cells onto the surface. In fact, the dead cells can be much easier dispossessed from the same during medium exchange than the live cells when less cell adherent cues are present on the whole backfill environment. Therefore, the backfill plays an indispensable role for studying the influence of surface chemical composition on the cell adhesion. Moreover, the cell survival (live cell number) should be considered to correlate with the cell adhesion instead of using cell viability as well as cell live/dead ratio.

4.3 The influence of weakly bound AuNPs on neuron adhesion and neurite outgrowth

In this part, the influence of sub-50 nm topography and surface chemical composition on the neuronal adhesion and neuritogenesis is comprehensively investigated as a function of particle sizes and densities. For this work, the WB disordered AuNPs with a diameter of 5 nm, 10 nm, 20 nm, 30 nm and 50 nm are immobilized on the SiO_2/Si substrates using the salinization method (see method section 3.1.2). The densities of each particle size were controlled by changing the incubation time (detail about the particle density, see Table 4.2). The AuNPs are functionalized with AUT, while the background is passivated by PEG backfill.

To investigate neuron adhesion as well as neurite outgrowth on the WB AuNPs of different sizes and densities, the cell survival and neurite number were firstly evaluated, which directly correlate to the cell adhesion and neuritogenesis, respectively. The fluorescent images of live (green) and dead (red) cells were taken after 3 DIV (Figure A4.4; Appendix B), while the dependence of cell survival (per mm^2) and neurite number (per cell) on different particle sizes and density are statistically quantified (Figure 4.10). The number of live cells increases with the particle density for most particles sizes (Figure 4.10A). The increases of the cell survival with the particle density are significant higher for bigger particle sizes. Neuron survival on 50 nm NPs shows the highest slope of cell survival/particle density curve, whereas the dependence curve for the small NPs of 5 nm shows the lowest slope. A similar dependence of neurite number on the particle density was also observed for the cells on different particle sizes (Figure 4.10B). Similarly, the neurite numbers of cells on bigger NPs is significant higher than those on smaller NPs. The increase in the cell survival and neurite number associated with the bigger particle size for a similar particle density indicates a clear particle size effect on promoting neuron adhesion and neurite development.

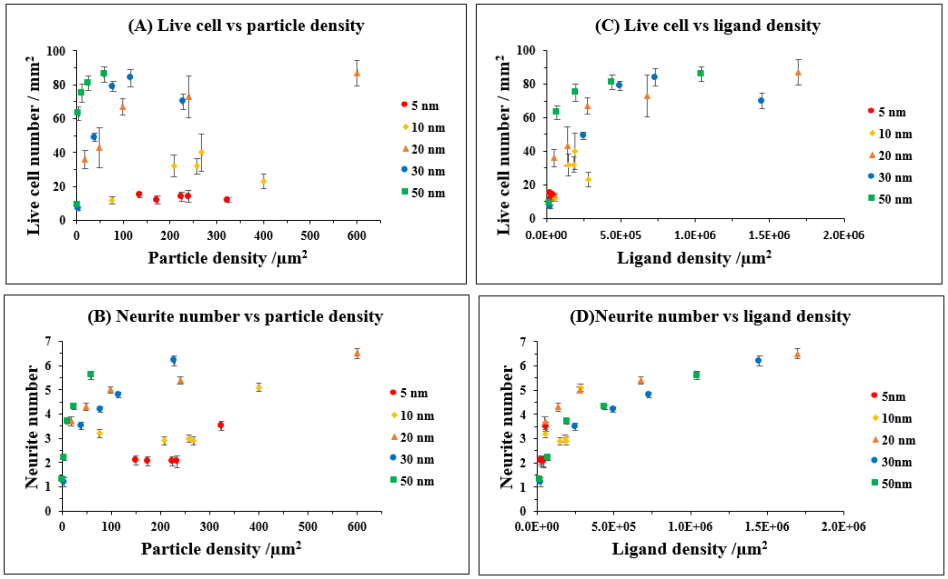

Figure 4.10 Dependence of live cell and number on particle density (A) and ligand density (C) for different WB AuNP sizes. Dependence of neurite number on particle density (B) and ligand density (D) for different WB AuNP sizes. The cells on WB particles: 5 nm, 10 nm, 20 nm, 30 nm and 50 nm AuNPs with different densities (Experiment is repeated at least three times, N=6; the variation shown by standard error, SE).

However, when the particle density is converted to the ligand density as shown in Figure 4.10C for the live cell number and Figure 4.10D for the neurite number, it can be seen that the difference of the cell survival and neurite number dependence on ligand density between different particle sizes becomes obviously smaller. The particle size effect is not observed when the particle density is converted to the ligand density. Different particle sizes process different capacity of ligand binding, since the binding ligand is proportional to the particle surface area. In case of the AUT molecules, the number of ligand was estimated to around 4.5 AUT /nm^2.[111] If only the upper half of AuNPs (semi-sphere) is considered to be involved in cell surface interaction, a specific number of ligand can be calculated for each particle size. When the particle size increases, the ligand number on each particle will be proportional to the square of its radius. By the same unit area, the ligand density is correlated to the density of AuNPs by a same proportional ratio, therefor the number of ligands per unit area is determined. Since the ligand number is increased by the square of the particle radius, a 50 nm AuNP will possess 100 times higher ligand binding number as compared to a small particle of 5 nm. For this reason,

larger particles possess a higher ligand binding capacity and support cell adhesion already at low particle densities. Obviously, the live cell and neurite number dependence on particle density are separated for each particle size, while the dependence on the ligand density are similar for all particle size. A steeply increasing trend before reaching a plateau is found for both the cell survival and the neurite number depending on the ligand density (Figure 4.10C, D). Very poor cell survival (under 10 cells /mm^2) is observed for all particle sizes when the ligand density is lower than about 10^5 ligands/ μm^2. However, the cell survival increases steeply with the ligand density until about 7.5 x 10^5 (ligands /μm^2), before it reaches more or less a saturation at a live cell number of about 80 cells/mm^2 (Figure 4.10C). A small fluctuation with a sudden decreasing in cell survival is observed in the case of 10 nm, which can be explained in the latter section when the cytotoxicity of the WB NPs is investigated. Altogether, the dependence of cell survival on the ligand density elucidates a quantitative relation between the cell density and the positive charges of surface ligands. The ligand density from about 10^5 (ligands/ μm^2) is required as a threshold ligand number to induce and promote cell adhesion, while the ligand density higher than 7.5 x 10^5 (ligands /μm^2) is the saturation ligand number for the cell adhesion. The slope of rising phase indicates the sensitivity of neurons responding to the change of surface cationic charges. This relation between cell survival and ligand density on the surface corresponds to a sigmoidal dose-response curve as can be also seen in Figure A4.5, Appendix B. Similarly, the number of neurite increases rapidly from 1 to 5 neurites per cell for all particle sizes until the ligand density reaches a range of about 7.5 x 10^5 (ligands /μm^2) (Figure 4.10D). At the higher density than 7.5 x 10^5, the neuron possesses an almost saturated neurite number, which corresponds to the development stage 4 and normal maturation.[33] The dependence of the neuron survival and neruite number on the particle sizes and the ligand density are consistent with P.Li's observations.[23] Although the ligand density of about 7.5 x 10^{15} ligands /μm^2 mostly saturates both the cell survival and the neurite number, this value is smaller than the value of 15 x 10^{15} reported by P.Li. However, the AUT concentration of 1 mM used in this work (compared to 0.5 mM in the case of P.Li) and the different binding ligand density of 4.5 ligands per nm^2,[111] (compared to 5.5 ligands per nm^2 in case of P.Li)[139] might contribute to this different observation. Therefore, it can be derived a plausible consideration that the neuron survival (adhesion) and the neurite number are strongly regulated to the ligand density. In fact, the cell survival and neurite number is independent of

the particle size in the sub-50 nm range. It denotes that the cell adhesion can be initiated as long as there is a sufficient ligand density of about 10^5 (ligands/ μm^2). The distribution of local spots with high ligand density (big particle) can promote the cell adhesion similarly as the case of a higher density of spots of low ligand number (small particle). For example, only 4 particles /μm^2 of 50 nm AuNPs can support the cell survival as similar as a 98-particle density of the 20 nm AuNPs (Figure 4.10A). The low density of 50 nm AuNPs in a unit area correlates to a significantly larger average interparticle distance compared to the case of high particle density for 20 nm AuNPs at the same number of ligand molecules. The electrostatic interaction between the positively charged amino-groups of the AUT ligand with the negatively charged glycocalyx compounds on the cell surface is assumed to mainly regulate the cell adhesion. The increase of cell survival with the surface charge density is independent of the particle sizes, which indicates the cell adhesion mediated by the nonspecific ligand can be consider as homogeneous adhesion as the case of cell adhesive behavior on the PDL coated substrate (control sample).

The neurite outgrowth of cells on different particle sizes and densities were also investigated by characterizing the average axon length (μm) of a neuron. The axon length is displayed versus the particle density (Figure 4.11A) and the ligand density (Figure 4.11B) for different particle sizes. The dependence of the axon length on the particle density increases steeply in the first phase, while there are decreasing trends of the axon length in the second phase with higher particle densities for all particle sizes as seen in Figure 4.11A. Although the dependence of axon length on the particle density is also separated by different sizes, but there is a decreasing phase of axon outgrowth for each particle size, which is not observed for the case of the live cell and neurite number as the aforementioned part. For example, the axon length of neurons cultured on the 50 nm AuNPs increases and decreases sharply by only dozens of particles. In fact, neurons with their neurites cultured on the 50 nm AuNPs of a small range from 1 to 54 particle densities can be visually seen in the fluorescent microscopic images (Figure 4.11C). However, when the axon length is plotted versus the ligand density (Figure 4.11B), the difference of the axon length depending the ligand density by different particle sizes becomes smaller. Obviously, the dependence of the axon length increases steeply to a peak, and followed by a fast decrease before reaching a saturation for 20, 30, and 50 nm particle sizes. A clear trend is not so apparent for the case of 5 nm and 10 nm due to the limitation of the ligand density in the whole ligand density range. From the graph, it can be seen that the increasing phase and the

plateau are independent of the particle size, while the peak and the decreasing phase vary with the particle size. The axon length seems to reach the shorter peak of axon length for the bigger particles as compared to the smaller particles. The 50 nm NPs show the lowest peak for the axon dependence on the ligand density, while the highest peak is observed for the 20 nm NPs (Figure 4.11B). Although, there is a different response of the neurite outgrowth with the ligand density as compared to the cases of the cell survival as well as the neurite number, the neurite outgrowth is also strongly regulated by the ligand density. The positive charge surface correlated with the ligand density might be responsible for this observation of neurite growth behaviour. It was reported that the positively charged surface can affect neurite outgrowth.[140-141] Although the mechanism how the positive charge affects the biological response of neurons is still not clear, it is suggested that an optimal range of intracellular calcium concentration is required for the neurite outgrowth.[142-143] Since the influx of Ca^{2+} across the cell membrane is controlled by the voltage-gated calcium ion channels, the electrostatic interaction between cell membrane and the electrically charged substrate might lead to the changes in the intracellular Ca^{2+} concentration. It was reported that a polymeric piezoelectric substrate with a surface charge density in a range of 10^{-4} C m^{-2} can be optimal for the neurite outgrowth.[141] This value is significant lower than a charge density of 24 x 10^{-2} C m^{-2} for 500 particles per μm^2 of 20 nm AuNPs as reported by

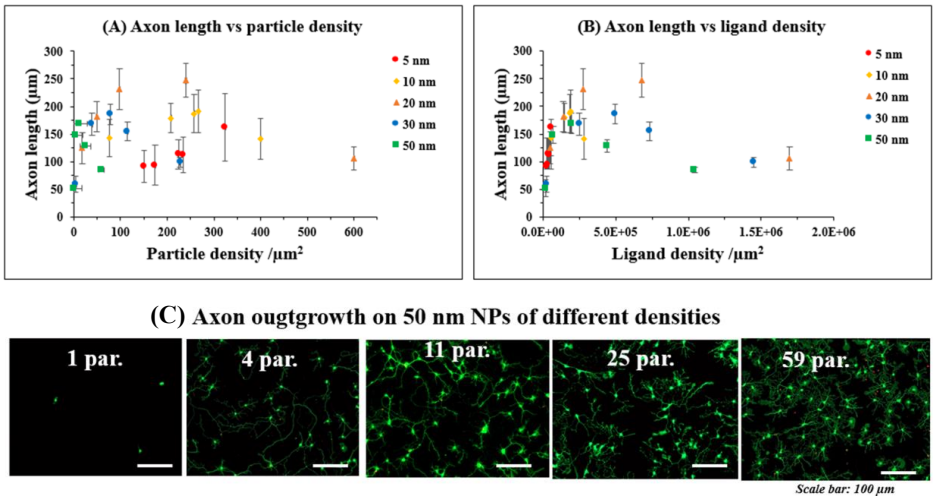

Figure 4.11 Dependence of axon length on particle density (A) and ligand density (B) for different WB AuNP sizes. (Experiment is repeated at least three times, N=6; the variation shown by standard error, SE). C) Live/dead fluorescent images of neurons on 50 nm WB AuNPs with different particle density.

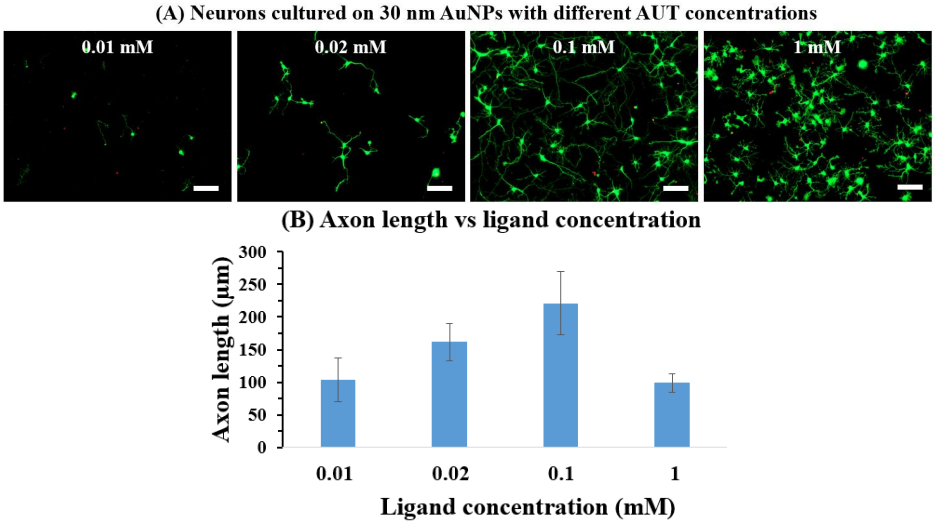

Figure 4.12 Live/dead fluorescent images (top) of neurons on 30 nm WB AuNPs (density 228 particles/μm^2) with different AUT concentration using (scale bar: 100 µm). Quantitative graph of average axon length (bottom) for neurons on each AUT concentration sample (the error bar is standard error, SE).

P.Li.[24] However, there might be cross-talk influences by other factors such as topography and surface coupling strength of AuNPs, which are also contributing to the axon elongation. These particle parameters will be thoroughly studied and discussed in the latter sections. In fact, bigger particles might possess not only better capacity of ligand binding, but also higher surface coupling strength due to their larger surface contact. Although, the small effect of topography on the neuron adhesion by the sub-50 nm AuNPs, the mechanical properties of the nanoplatform can be crucial to regulate the cell adhesion and neurite outgrowth.[144-145]

Moreover, the strong influence of ligand density on the neurite outgrowth is also supported by control experiments, in which different ligand concentrations are used instead of using only a universal concentration of 1 mM in all experiments. The 30 nm NP samples with a same high density of 235 particles per μm^2 were functionalized by different AUT concentrations of 1 mM, 0.1 mM, 0.02 mM, and 0.01 mM. The cell survival and neurite outgrowth can be visually noticed from the fluorescent microscopic images of the neurons as shown in Figure 4.12.A. The average axon length of a neuron is statistically quantified for each AUT concentration sample (Figure 4.12.B). A high neuron survival with short neurites (about 100 µm) can be seen for cell cultured on the 1 mM AUT concentration sample as described before. Interestingly, the neurons

cultured on the 0.1 mM AUT concentration sample show the longest axon length as compared to the neurons cultured on other concentration samples. The axon length decreases together with the cell survival when the cells cultured on a relative low ligand concentration sample of 0.02 mM. At a very low ligand concentration of 0.01 mM, a very poor cell survival as well as short neurite outgrowth is observed, which may indicate an insufficient ligand density requiring for cell adhesion.

From these observation, it can be concluded that there is domination of ligand density over particle topography and distribution for all cell survival and neurite number, but also topographical effects for axon elongation in sub-50 nm range. However, here the cell adhesion was studied on the weakly bound (WB) AuNPs, when the particles were found to be not very stable on the surface and could be grasped by neurons.[61] In the next part the influence of particle-surface binding strength on the neuron adhesion will be comprehensively discussed. This part will also address the remain consideration about the poor and fluctuated cell survival as well as neurite outgrowth of neurons on the small WB particles of 5 and 10 nm sizes.

4.4 Surface coupling strength of AuNPs causes cytotoxicity on neurons

In this section, the influence of particle coupling strength on neuron adhesion will be thoroughly addressed and discussed. Although AuNPs are commonly used as nanostructure platforms for biological applications,[9-11] it is also known that AuNPs can develop a cytotoxic profile in biological entities depending on their sizes,[146-148] shapes,[149-150] compositions,[151-152] and capping agents.[153-154] It turned out that some particle properties such as the size have opposed influences on the cell behavior. For instance, metal AuNPs show an increased cytotoxicity with decreasing particle diameters, while the particle uptake rises with the particle size at mesoscopic scales. In most cases, the cytotoxicity of nanomaterials was studied by using colloidal AuNPs in vitro or in vivo. AuNPs embedded in a material or bound to a material surface are usually considered nontoxic. However, the cytotoxicity of nanomaterials releasing from the surface of the supporting structure during cell culture is still not fully clarified. Furthermore, it is known that the cells can create mechanical stress on the substrate via adhesion sites during their development.[45-46] Therefore, continuing pulling of particles from the cells may unfurl cytotoxic behaviour of particles and affect their viability due to the possibility of AuNP uptake. It can be anticipated that the binding strength of AuNPs to the sample surface should have a considerable impact on their cytotoxicity.

Table 4.4 WB and SB disordered AuNPs of different sizes and densities immobilized on SiO_2 substrates.

Size (nm)	Particle density (particles /μm^2) obtained by different incubation time (min)			
	1	**10**	**30**	**60**
5	150 ± 3	174 ± 4	224 ± 3	234 ± 8
10	199 ± 2	207 ± 4	247 ± 6	268 ± 15
20	18 ± 1	47 ± 6	98 ± 7	240 ± 12

In this work, since AuNPs are mainly used as the tool to tune the chemical composition on the surface for controlling the neuron adhesion, 5 nm, 10nm and 20 nm AuNPs of different density are prepared for both strongly bound (SB) and weakly bound (WB) AuNPs as shown in Table 4.4. The AuNPs are functionalized with the AUT ligands for inducing cell adhesion, for which the background is passivated by the PEG molecule to prevent undesired cell binding. Consequently, the cells adhere mainly via the AUT-AuNPs to the sample surface. The surface coupling of AuNPs on the substrate has been confirmed and characterized by the AFM as discussed in section 4.1.3. Depending on the binding strength of the particles themselves, the particles may detach from the surface due to the cell adhesion grasp during the cell culture. Thus, an alteration of cell viabilities as a function of particle binding strength and size need to be carefully investigated. Additionally, it is important to compare the cytotoxicity of the surface released AuNPs to dispersed AuNPs applied from solution buffer in the culture medium.

4.4.1 Cytoxic observations for SB and WB AuNPs

For this study, rat cortical embryonic neurons on the AUT- AuNPs of both binding strengths with different sizes and densities are used. To estimate the survival of the neurons after three days of in vitro culture (3 DIV), the cells are visualized by co-immunostaining with calcein (green) for live cells and ethidium homodimer (red) for dead cells. Fluorescence images of cultured cells are recorded and analyzed, (Figure 4.13), (live/dead stained cells of all particle sizes and densities are shown in Figure A4.6, A4.7; Appendix B).

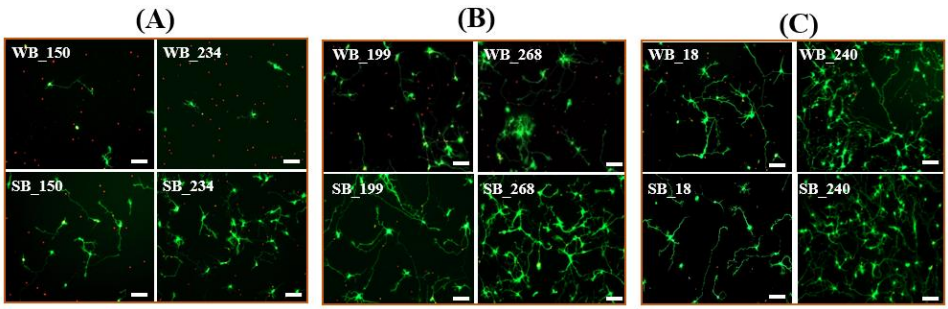

Figure 4.13 Representative fluorescence images of DIV3 neuron cultures on the nanoparticles of different sizes and densities (per μm^2) for weakly bound (WB) and strongly bound (SB) particles with live (green) and dead (red) staining. (A) 5 nm AuNPs with a density (particles per μm^2) of 150 (WB_150), 234 (WB_234) for WB particles and 150 (SB_150), 234 (SB_234) for SB particles. (B) 10 nm AuNPs with a density of 199 (WB_199), 234 (WB_268) for WB particles and 199 (SB_199), 234 (SB_268) for SB particles. (C) 20 nm AuNPs with a density of 18 (WB_18), 240 (WB_240) for WB particles and 18 (SB_18), 240 (SB_240) for SB particles. Scale bar 100 µm.

From the micrographs, there are noticeable differences of the cell survival between neurons plated on AuNPs of different binding strengths. Overall, the cell survival is significantly higher for the SB AuNPs than for cells on the WB AuNPs for all sizes and densities. The cell survival differences are strongest for particles with a diameter of 5 nm and 10 nm. To obtain a reliable conclusion, the cell survival and morphology on both binding strengths are statistically investigated. A clear dependence of the cell survival on the density of AuNP can be seen for all SB AuNP sizes (Figure 4.14A). The density of vital neurons rises with increasing particle density. Here, the surface composition on nanometer scale is controlled by using different AuNP densities and different AuNP sizes. For the same NP size, the increasing NP density leads to an increase of the number of particle associated adhesion molecules, which will enhance the cell adhesion. Both, increasing particle size and particle density lead to an increase of the ligand density by more than one order of magnitude, which explains the enhanced neuron survival for the SB AuNPs and in parts also for the WB AuNPs.

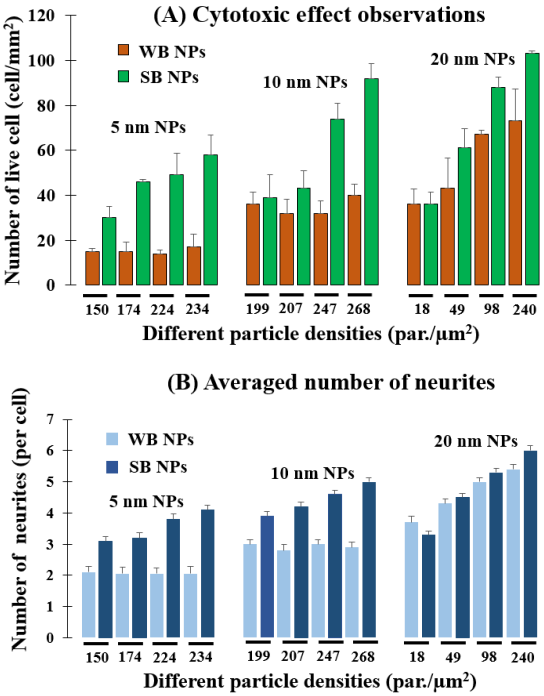

Figure 4.14 The cell survival and neurite number of the cells on WB particles compared to SB particles. (A) The cytotoxic effect of surface bound particles is derived from the number of live cell on the same particle size, density, and binding strength. The cells on both SB and WB particles: 5 nm AuNPs with densities of 150, 174, 224, and 234; 10 nm with densities of 199, 207, 247, and 268; and 20 nm with densities of 18, 49, 98, and 240. (B) The average number of neurites from neurons cultured on the same samples in (A). (Experiment is repeated at least three times, N=6; the variation shown by standard error, SE).

Interestingly, this trend of enhanced cell-density can be observed for the WB particles only on the 20 nm AuNPs, while the cells plated on smaller AuNPs (5 nm and 10 nm) show a similar low survival independent of the particle density (Figure 4.14A). The determined cell survival of neurons on the 20 nm WB AuNPs is consistent with our previous findings.[24] Neurons cultured on the 5 nm WB AuNPs show a large difference of cell survival by two- to threefold ($P < 0.01$, Student's t-test) for high particle densities, in comparison with the SB AuNPs. This indicates a cell harming effect of AuNP that are only weakly bound to sample surface. This detrimental influence seems to be size dependent since the survival differences are not so pronounced for larger AuNPs. They can be only unambiguously observed ($P < 0.01$) for high

particle densities (10 nm NPs: 247, 268 particles/μm^2; 20 nm AuNPs: 98, 240 particles/ μm^2, see Table 4.4) and do not exceed 30 % for 20 nm particles, Figure 4.14A.

In additional to the differences on the cell survival, the cells cultured on the 5 nm and 10 nm WB AuNPs show an unhealthy development with poor neural polarity and dendritic growth (Figure. 4.14B and Figure A4.6; Appendix B). A majority of cells develop only a few neurites (2-3), which remain mostly shorter than 100 μm. On the contrary, neurons grown on the SB AuNPs of 5 nm and 10 nm diameter exhibit more dendrites (3-5), matured growth cones, and formation of neural network. Neurons plated on 20 nm particles of both binding strengths do not show major differences in cell shape and neurite number. They possess a normal morphological development similar to neurons cultured on control samples after 3 DIV with few hundreds of micrometer long axons and around 5-6 neurites, which is in agreement with previous studies.[33] More importantly, it can be seen that only for SB particles, the neurite development shows a particle density (adhesion site number) dependence in which the number of neurites increases with the number of particles. The neuron developments on the SB particles are consistent with the neuron developments reported from previous studies of neuronal growth on nanostructure.[1, 3, 155]

4.4.2 Cytotoxicity comparisons between SB, WB, and colloidal AuNPs

The harmful effect of the nanoparticles indicates that the WB AuNPs develop a severe cytotoxicity during in vitro culture. The cytotoxic properties of AuNPs exposed to cells from colloidal solutions have been confirmed from previous studies.[156] It was also reported that small AuNPs possess a higher cytotoxicity than large AuNPs.[147, 157] The cytotoxicity becomes clearly apparent for 5 nm AuNPs where a detrimental influence on the survival can be observed for all particle densities, while for larger particles the difference between strongly and weakly bound particles vanishes.

Generally it is assumed that positively charged nanoparticles enter cells via binding to membrane-associated proteoglycans.[158] To verify a possible uptake of the amino-functionalized WB AuNPs, the cross sectional studies are performed to visualize and estimate the uptake of AuNPs. Therefore, cells after 3 DIV are fixated and embedded in resin by an ultra-thin resin embedding method optimized for scanning electron microscopy (SEM) of individual cells.[101] Focused ion beam (FIB) cross-sections are carried out to access neuron cross section and to

evaluate the AuNP uptake for both SB and WB AuNPs. For this purpose, the cortical neurons are cultured at 3 DIV on samples modified by AuNP on the highest accessible densities of all three sizes (5 nm, 10 nm and 20 nm) without addition of any solution dispersed nanoparticles. It is observed that high number of particles inside cells cultured on the WB AuNP, while almost no particles can be found inside the cells on SB AuNPs (Figure 4.15 and Figure A4.8; Appendix B). The AuNPs inside cells tend to form clusters or groups of AuNPs rather than being individually distributed over the cell (Figure 4.15C, D). These observations can be explained as the AuNPs are trapped by either endosomes or lysosomes.[148, 159-160] A distinctly smaller fraction of particles can be found inside the cells for 10 nm AuNPs. Obviously, the uptake of 20 nm AuNPs is higher than for 10 nm AuNPs (Figure. 4.15A). However, it should be noted that the diameter of the smaller particles is in the same range as the resolution of the SEM. The latter may explain why the 5 nm AuNPs could not be visualized inside the cells for both particle

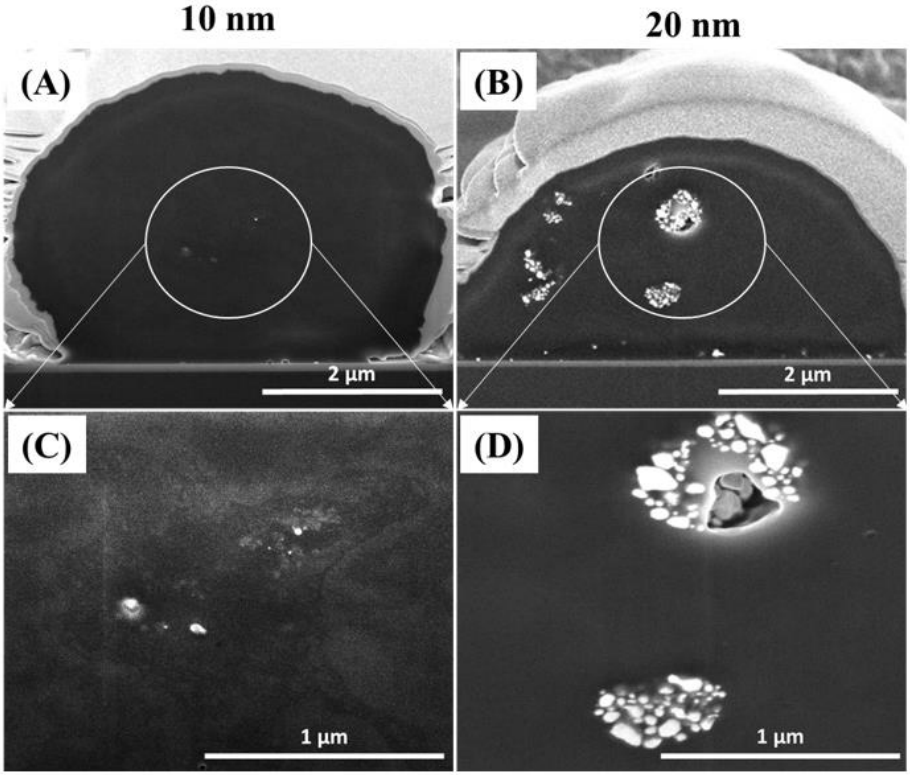

Figure 4.15 FIB cross-section images of DIV-3 cells on the 10 nm (A) and 20 nm (B) WB particles, and images at higher magnification (C) and (D).

binding strengths. Furthermore, it has been reported that particle uptake decreases with the NP size, which is in line with our observations.[161-162] Another reason for the low signal for 5 and 10 nm AuNPs samples can be the cytotoxicity of the particles themselves, since only cells with low particle uptake survive long enough to be studied by SEM. In order to locate the uptake AuNPs, the cells are stained with osmium tetroxide and uranyl acetate prior to the resin embedding steps for enhancing the contrast between intracellular organelles.[101, 163] The osmium tetroxide is used for staining lipid components, especially the cell membrane, while the uranyl acetate staining is performed for proteins, nucleic acids, hydroxyl groups in carbonhydrates and RNA. A statistical analysis of FIB cross-sections for investigating the uptake of 20 nm AuNPs inside the cells indicates that, mostly the uptake AuNPs are found close to the nucleus, where is known as the endoplasmic reticulum (Figure 4.16). It was reported that the uptake nanoparticles can be found in the smooth endoplasmic reticulum, and some can internalize the nucleus.[149, 164] The bigger particles might be mostly trapped by the reticulum, while the smaller particles might easily internalize the nucleus, and therefore resulting higher toxicity.

In the further study, the cytotoxicity of AUT-AuNPs is investigated by the same sizes and modified ligands, but freely dispersed in the cell culture medium in addition to the SB AuNPs. Therefore, 5 nm, 10 nm and 20 nm AUT-AuNPs are directly added to the culture medium after

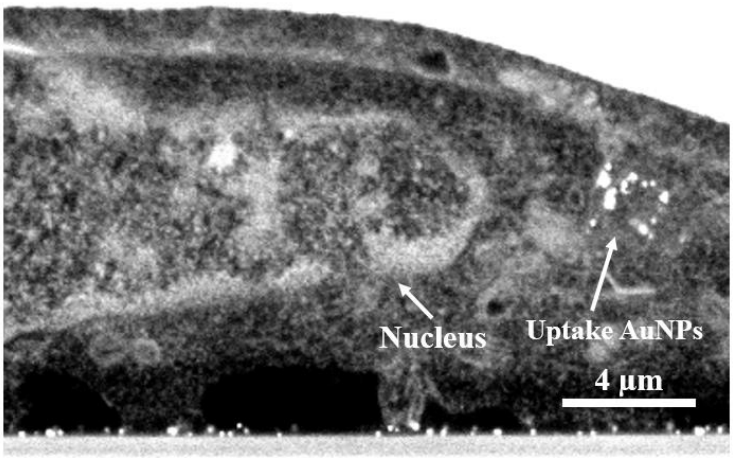

Figure 4.16 FIB cross-section images of a neuron cultured on the 20 nm, which is stained with osmium tetroxide and uranyl acetate in the sample preparation step for the FIB characterization.

seeding cells on Si/SiO_2 samples decorated by SB particles of the same size. The particle densities for each particle size are used at the highest density of 60 min incubation time (see Table 4.4) for this investigation. The amount of added colloidal nanoparticles for each particle size has been estimated according to the as-prepared particles as 4.7×10^{12}, 5.1×10^{11}, and 2.5×10^{10} particles per ml (or cm^3) of culture medium (see Table A4.1, Appendix. B). The number of added particles from solution (per cm^3) is comparable to the number of surface tethered particles for 20 nm AuNPs (per cm^2) and clearly exceeds the number of bound particles by at least one, and two orders of magnitude for 10 nm and 5 nm AuNPs respectively. The DIV-3 cell survival is statistically estimated after plating neurons on SB AuNPs with and without exposure to the colloidal particles of different sizes (the experiment is repeated at least three time). It is found that that the cell survival of cortical neurons strongly decreases, if the cells are immersed into a colloidal particle solution for both SB AuNPs and laminin coated SiO_2 (control) samples. The dispersed AUT-AuNPs shows a similar cytotoxic reduction of live cells for samples with SB particles and control samples (Figure A4.10, A4.11; Appendix B). Moreover, the toxicity effect decreases with the increase of the particle size. These observations consistently confirm the previously reported toxicity of solution-dispersed aminoalkylthiol functionalized AuNPs.[154, 165-166]

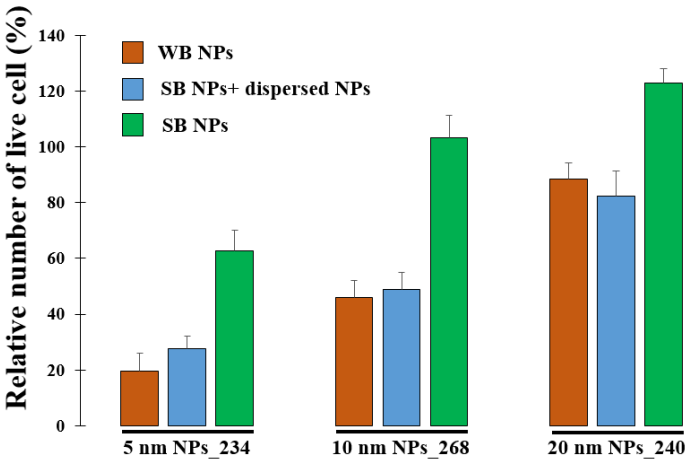

Figure 4.17 The cytotoxic effects of WB and AUT colloidal particles. The relative number of live cells between WB-NP samples, SB-NP samples + dispersed NPs, and SB-NP samples is shown. The densities for 5nm, 10 nm and 20 nm NPs are 234 (NPs_234), 268 (NPs_268), and 240 (NPs_240) respectively (particles per μm^2). (Experiment is repeated at least three times, N=6; the variations shown by standard error, SE).

Moreover, the cytotoxic effects of WB AuNPs are compared to the dispersed colloidal AUT-AuNPs, (Figure 4.17). Here, the relative number of live cells (in percentage) are normalized by dividing the average number of live cells of nanoparticle samples by the average number of live cells cultured on the control samples for each experiment. Generally, it can be seen that the cell survival is significantly different for cells cultured on SB AuNPs and the cells in contact with WB AuNP binding or dispersed AuNP for all particle sizes. Neurons in contact only with strongly bound particles show the highest survival among all tested samples, (see also Figure 4.14A). Interestingly, the survival of cells on 20 nm SB NP is higher than on the laminin control sample, which demonstrates the suitability of bound nanoparticle samples as model surface to promote cell adhesion at the nanoscale.[4, 167-169] It also reflects strong interaction between the positively charged, surface tethered nanoparticles and negatively charged glycocalyx of the cell membrane.[11] Furthermore, it can be seen that the cell survival strongly decreases for all particle sizes if colloidal or WB particles are present in the culture medium, especially for 5 nm and 10 nm NP sizes. It is worth noting that the harmful effect of the WB particles is similar or even slightly stronger for these small particle sizes than that of colloidal particles, although the number of particles exposed to the cells is smaller, see above and Table A4.2; Appendix B. This indicates a different endocytosis efficiency for surface bound and

colloidal AuNPs. Generally, it is assumed that the uptake of colloidal particle happens in a two-step process.[170-172] Within the first step, the freely diffusing particles associate with the cell membrane. During the second step, these particles are internalized into the cell by endocytosis. In principle, both uptake processes can deviate for surface tethered in comparison to medium-phase particles. For the association process, we have to take into account that the distribution of the particles is restricted from 3D for colloidal particles to 2D for surface tethered AuNPs, which increases the local density of particles at the vicinity of the cell membrane for the latter. Colloidal particles of small size and low sedimentation rates diffuse freely within the medium and bind / dissociate occasionally to the cell membrane.[173] If the affinity constant (K) is large, then the density of membrane associated particles saturates after a characteristic time τ.[170] The affinity constant is defined as the ratio of the rate constant k_a for the NP adsorption and k_d dissociation from the membrane. The saturation density of membrane associated particles can be estimated by [170]

$$D_{Pmax} = [k_a C/(k_a C + k_d)]D_0. \qquad (1)$$

C represents the concentration of particles added to the medium. The maximum density of particles D_0 that can adsorb to the cell membrane can be estimated from geometrical considerations by dividing the unit area (1 µm²) by the projected area of the a nanoparticle and multiplying with the volume fraction of monodisperse spheres randomly loose packed in 2D films.[174] The projected AuNP area is estimated taking the length of AUT and the Debye screening into account. The characteristic time can be calculated by $\tau = 1/(k_a C + k_d)$. Eun at al determined experimentally k_a = 4.95 x 10^3 $M^{-1}s^{-1}$ and k_d = 2.79 x 10^{-5} s^{-1} for amino-functionalized 18 nm AuNP, which allows the calculation of K, D_{Pmax}, and τ, Table 4.5.[175] From

Table 4.5 The highest number of different AuNP sizes immobilized on SiO_2 substrates and the maxium number of particles bound on cell membrane after τ.

Size [nm]	Density sample tethered AuNPs [µm^{-2}]	τ [h]	D_{Pmax} [µm^{-2}]
5	234 ± 3	4.2	7260
10	268 ± 15	8.7	648
20	240 ± 3	9.8	12

the resulting values it can be concluded that the characteristic times are clearly shorter than the culture time. Therefore, the particle density on the all membrane is saturated for colloidal particles when the cytotoxicity is determined. A comparison of this density with the density of particles tethered to the sample surface reveals that less colloidal particles are associated to the membrane for 20 nm AuNPs. In contrast, the density of membrane associated particles is higher than that of surface bound particles for 10 nm and 5 nm particles, nevertheless, the survival of cell in contact with WB and colloidal particles is similar. Apparently, surface confined but WB particles can possess a similar or higher toxicity than colloidal particles although the contact of the cell to the WB particles is limited by a relative small number of involved particles. These results indicate that the different cytotoxicity is not caused by a different accessibility of AuNP to the cell membrane, but rather by a different internalization process. Adherent cells organize their cytoskeleton according to physical and chemical properties of the sample surface.[6, 176] However, the cortical cytoskeleton also plays a pivotal role for different endocytic pathways.[177-178] The reorganization of the actin network at the interface between cell and solid sample surface in comparison to the solution exposed parts of the cell membrane may affect the efficiency of particle uptake. Furthermore, it is known that cells can transmit certain forces from their cytoskeletal contractile activities via adhesion cues to the substrate.[179-182] In this work, the tension forces generated by cells are transmitted from the cells to the substrate through the AuNPs, which function as adhesion bridges. The dual function of the actin cytoskeleton regarding force transmission and endocytosis may result in a variation of particle uptake effectiveness. Therefore, it can be assumed that the probability of AuNP uptake into the cells of surface confined nanoparticles can be different (larger) from the internalization of particles homogenously dispersed in buffer medium.

4.5 Surface coupling strength influences axonal outgrowth of neurons

It has been reported that the mechanical property of substrate plays an important role for the regulation of neuron adhesion and neurite outgrowth.[36, 45, 144-145, 183] In fact, mechanosensing is critical for the axon growth in the developing brain as reported by Koser et al.[183] Besides the cytotoxic effects of the WB NPs as discussed in the above section 4.3, the influence of the particle coupling strength on neurite outgrowth will be investigated in this part for neurons cultured on the 5 nm, 10 nm, and 20 nm AuNPs with different densities for both surface coupling

strengths. Although the cytotoxicity of WB NPs can affect the neurite outgrowth, a clear dependence of the axon length on the chemical ligand density for WB AuNPs of different sizes and densities has been affirmed in section 4.3. However, neglecting the cytotoxic effect, a change in surface coupling strength of AuNPs may result in different behavior of neurite outgrowth. Therefore, a statistical analysis of axon length for the neurons on the both WB and SB AuNPs by the same sizes and densities is analyzed, Figure 4.18A. The neurite length of neurons cultured on the similar particle sizes and densities is compared between WB and SB AuNPs. In the case of WB AuNPs, an increase of the axon length is observed for all particle sizes when the particle density increased. The increase of the neurite length with the particle density is already presented in the section 4.3, in which bigger particles induce the steeper slope for the neurite outgrowth. The densities of 5 nm, 10 nm, and 20 nm AuNPs used for this investigation vary in the increasing phase of neurite length (see Figure 4.11A).

In contrast, a complete opposite behavior of the axon outgrowth could be found on the SB AuNPs samples. Interestingly, the axon length of neurons on the SB AuNPs decreased with the particle density for all particle sizes. Even at very low 20 nm AuNP density of about 18 particles per μm^2, neurons develop the longest axon length. When the particle density increases, the neurite length decreases. The neurite outgrowth of the neurons cultured on the lowest (18) and highest particle (240) densities for WB and SB 20nm AuNPs could be noticeably recognized in the calcein fluorescent labeled images, Figure 4.18B. The contrasting behavior of the neurite outgrowth indicates a smaller impact of the chemical cue on SB AuNPs, but mainly regulates the neurite outgrowth on WB AuNPs. Since the mechanotransduction plays a pivotal role during axon outgrowth, the different particle coupling strength could explain this opposed elongation behavior. The different coupling strength of the WB and SB AuNPs were characterized by the AFM as shown in section 4.1.3. The SB AuNPs possessed significant stronger coupling strength onto the surface than the WB AuNPs.

To further investigate the effect of the binding strength on the cytoskeletal development, fluorescent immunostaining experiments are carried out. The cell nuclei, actin and tubulin proteins are labeled for the neurons cultured on the highest density (240 particles /μm^2) of 20 nm AuNPs of both coupling strength types (Figure 4.19). A shorter axon length (about 150 μm)

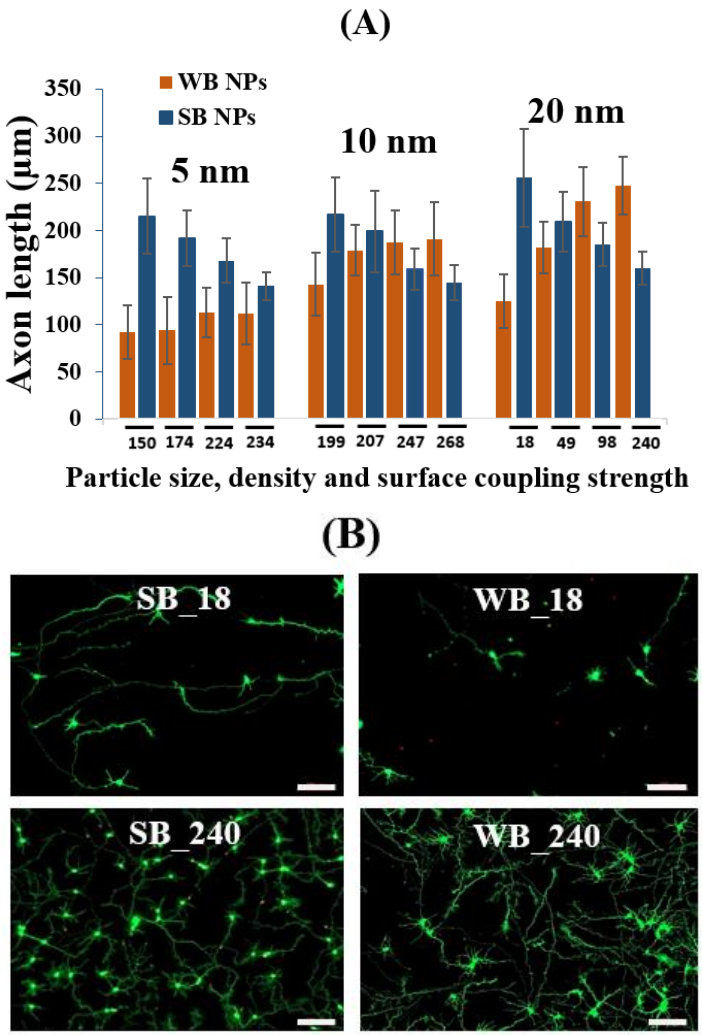

Figure 4.18 A) Dependence of axon length on particle density. B) Live/dead fluorescent images of neurons on 20 nm WB and SB NPs with lowest and highest particle densities (Experiment is repeated at least three times, N=6; the variations shown by standard error, SE). Scale bare: 200 µm.

with a bigger growth cone size is typically observed for the cell on the SB AuNPs as compared to a longer axon length (about 250 µm) with a smaller growth cone size for the case of WB AuNPs.

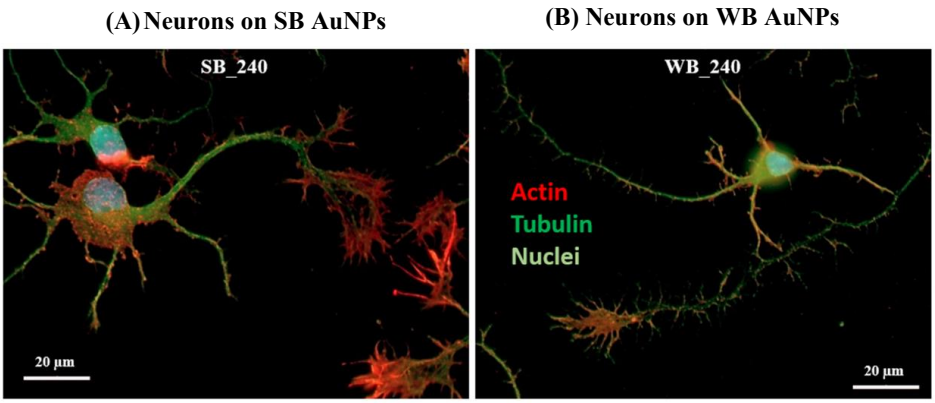

Figgure 4.19 Immunostaining images of neurons labelled with actin, tubulin, and dapi (for nuclei), the cells are cultured on 20 AuNPs with density of 240 particles /μm^2 for SB particles (A), and for WB AuNPs (B).

Besides the neurite length, a morphological difference in cell bodies are also observed. Cells plated on the SB AuNPs possess bigger cell bodies with an overall higher number of neurite branching (see also Figure 4.14B). In addition, the larger cell spreading correlates with higher actin protein expression in the cell body as well as in the growth cone of the cells on the SB AuNPs. This might indicate better cell adhesion of the cells with a stronger polymerization of actin due to better transduction of forces (see the model later). Therefore, the immunostaining of intracellular actin and vinculin proteins are also performed to visualize the adhesion complexes formation, Figure 4.20. In agreement with Figure 4.19, neurons cultured on WB AuNPs of the 240 extend longer neurite with smaller growth cone size, but less actin and vinculin (Figure 4.20A) as compared to neurons on the same particle density of SB AuNPs (Figure 4.20C). The higher actin and vinculin expression denote a larger adhesion complex formation of the neurons on SB AuNPs, to a certain extend. The weak coupling strength of WB AuNPs on the surface might result in fewer formation of adhesion complexes since the particles can be grasped or slipped over the surface during cell adhesion. Interestingly, at a relative low

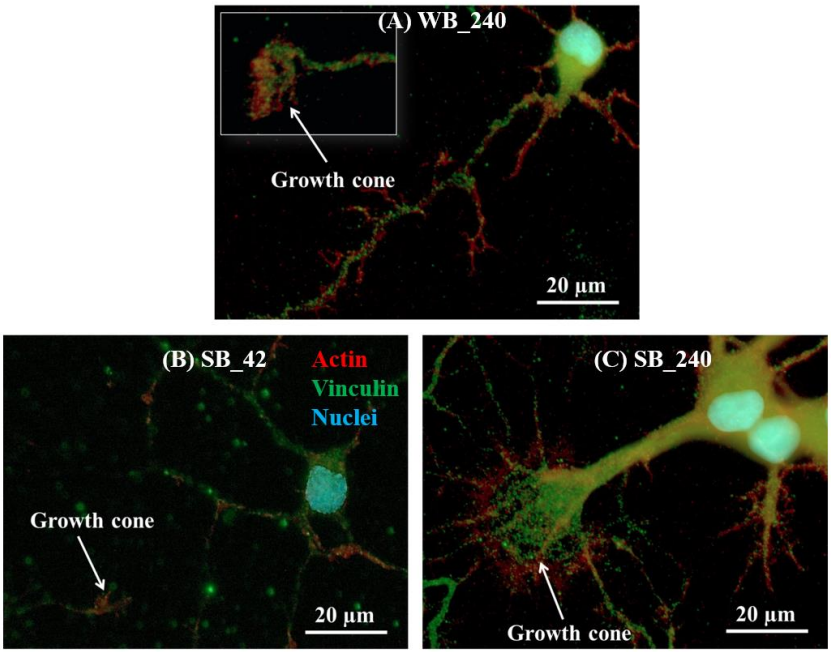

Figgure 4.20 Immunostaining images of neurons labelled with actin, vinculin, and dapi (for nuclei). The cells are cultured on 20 nm AuNPs with density of 240 (A) particles /µm^2 for WB particles, and 42 (B) and 240 (C) particles /µm^2 for SB particles. The growth cone is shown by the arrow in each image.

particle density of 42 SB AuNPs /µm^2, a similar level of neuron adhesion and neurite outgrowth is observed similar as for cells on WB AuNPs at high density (Figure 4.20B). The longer axon with a small growth cone indicates moderate actin and vinculin expression for these cells.

It is known that the axon growth is strongly controlled by the dynamic extension or retraction of the growth cone.[39, 45, 184] During neuronal development, cells communicate with environmental guidance cues through their receptors, which link their rigid cytoskeletal elements to the adhesive cues on the substrate. In order to elucidate the influence of different AuNP decorated samples on axon outgrowth, a simple model of growth cone dynamic has been proposed, Figure 4.21. The process of actin polymerization in filopodia of the growth cone will strictly regulate the dynamic growth cone protrusion.[39] When globular actins (G-actins) are polymerized to form filament actins (F-actins), a pushing force arises at the leading edge against the plasma membrane for growth cone extension, called $F_{polymerization}$. In addition, another force that governs the F-actin is the myosin contractile force, called retrograde flow (RF), F_{myosin},

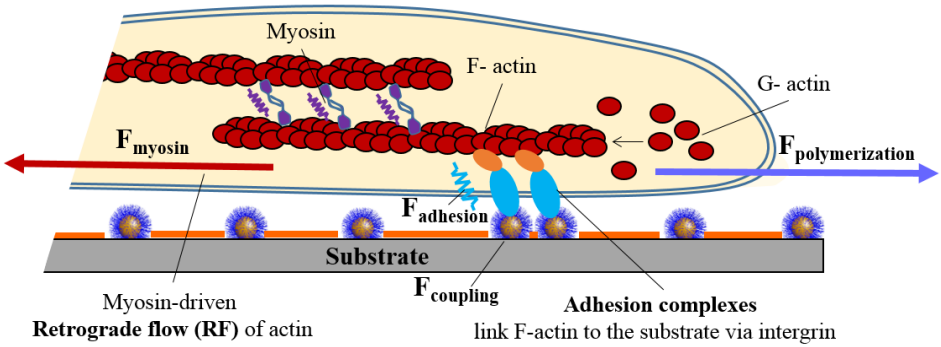

Figure 4.21 The model of growth cone extension on AuNPs immobilized the silicon substrate. F-actin polymerization from G-actin at leading edge of the growth cone pushes the plasma membrane for extending the growth cone forward ($F_{polymerization}$). However, the contractile activities of the myosin II attaches and pulls the F-actin reaward (F_{myosin}), which results a constitutive retrograde flow (RF) of the actin filament. The cell adhesion on the ligand functionalized AuNPs decorated substartes can activate integrin and cluster adhesome-adaptor proteins to form focal adhesion complexes. The attachments of cells on the substrate via AuNPs will result a mutual interaction between the cell and the AuNPs ($F_{adhesion}$), which restrains the RF and create cell traction forces on the particles. Depending on how stable the AuNPs couple onto the substrate ($F_{coupling}$), the mechanotransduction of adherent neurons can be trigged to regulate the axon outgrowth.

which is antiparallel with the $F_{polymerization}$.[185] The combination of the contractile force of myosin and the rearward RF of actin filaments due to leading edge actin polymerization regulates the growth cone dynamic. The balance between the rate of F-actin polymerization and the RF will determine whether the growth cone extends or retracts. If the RF is decreased by a certain factor, the growth come protrusion will increase and vice versa.[185] In addition, many adaptor proteins cluster together forming adhesion complexes, which physically link the F-actin cytoskeleton to adhesive cues on the substrate through cell receptors (integrin, NCAM).[39] The coupling between substratum-integrin-actin is named the molecular clutch,[38] which results in slowing down of the RF by an adhesion force, $F_{adhesion}$. This adhesion force associated with the molecular clutch arises to restrain myosin driving the RF and therefore regulating the force of actin polymerization to propel growth cone forward protrusion. Although the molecular clutch mechanism is still under debate for neuronal cells, the adhesion of neurons creating stress force to substrate has been reported by many research groups.[45-46] In this thesis, the AUT-AuNPs decorated substrates exclusively provides the binding sites for neuron adhesions since the background was passivated by backfill. It is assumed that when the neurons adhere on the AUT-AuNPs, the assembly of proteins forming adhesion complexes would link the F-action to the AuNPs through cell receptors. Depending on the dynamic state of the adhesion complex

formation and the coupling strength of AuNPs on the substrate ($F_{coupling}$), the adhesion force arises and affects the balance state between the RF and $F_{polymerization}$.

In case of the WB AuNPs, the pulling of neurons grasping on the particles during neurite outgrowth might result in the particle slipping or lifting from the substrate due to the weak $F_{coupling}$. The loss of particle from the surface can reduce the influence of the adhesion forces. In fact, from the FIB cross-section of neurons cultured on WB AuNPs, the particles were found to be lifted up with the cell membrane from the substrate, (Figure A4.9; Appendix B). The axon outgrowth is found mainly regulated by the ligand density as discussed in the section 4.3. Even without direct and specific link between cytoskeletal and extracellular environment, the actin polymerization is still activated by the surface charge, which is associated with the chemical ligand density on the surface.[140-141] However, there are possibly cross-talk influences between both the chemical ligand and mechanotransduction on the axon outgrowth, taken the different peaks of axon outgrowth dependence on the ligand density for different particle sizes into account (see the Figure 4.11.B). At the low particle densities, $F_{adhesion}$ is relative high due to the tensile force of cell pulling, while the $F_{coupling}$ is very week in the initial phase. Thus, low $F_{coupling}$ can limit the transmitted force between cell and substratum due to force dissipation. When the particle density increases, the number of point contact adhesions increases and results in the higher transmitted force (higher $F_{adhesion}$). Therefore, the axons are elongating. However, when the particle density increases, the transmitted total force increases to a critical value, which starts causing clutch slippage (breaking) at point contacts.[39] The slippage (breaking) of the adhesion complexes results in fewer and short lived point adhesion contacts, which disrupts the transmitted forces necessary for growth cone extension. Thus, when the particle (ligand) density increases, the axon length increases to a peak and decreases before reaching a plateau. This consideration is also supported by a statistical analysis of axon outgrowth on 30 nm SB AuNPs at a relative high particle density performed by varying the ligand concentration (see Figure 4.12). A low ligand concentration (0.1 mM) used for functionalizing the high particle density (228 particles/μm^2) can result in a $F_{adhesion}$ strength as similar as 1 mM ligand concentration for a lower particle density (77 particles/μm^2). Moreover, bigger particle sizes can possess stronger coupling strength (higher $F_{coupling}$ forces) onto the surface due to their larger area interacting with the surface. Thus, the interplaying influences of both the chemical ligand and the mechanical aspect of WB AuNPs might contribute to peak shift of axon length dependence on

the ligand density from 20 nm to 50 nm AuNPs, Figure 4.11B. The peak shift that is not clearly observed for the cases of 5 nm and 10 nm AuNPs could be explained due to the limitation of the ligand density for small sizes as well as their cytotoxicity (section 4.3).

In contrast to the WB AuNPs, it is found that the significantly stronger coupling strength of SB AuNPs contributes to different behavior of axon outgrowth with the particle density. The high $F_{coupling}$ of SB AuNPs allow the forces of the cellular cytoskeletal pulling to be transmitted to the substratum, which results in high local $F_{adhesion}$. Even very few AuNPs can transmit a considerable total force to the cell, high enough to stimulate fast axon elongation, which is not the case for WB AuNPs with very small $F_{coupling}$. High densitie particles of SB AuNPs (point contacts) contribute to even higher $F_{adhesion}$, which overcomes a threshold and causes the breaking or disassembly of point contacts via molecular stretching.[39] Therefore, the axon elongates with a lower rate for increasing densities of SB AuNPs.

Moreover, the larger amount of actin and vinculin proteins, which could be found in the growth cone of neurons on SB AuNPs at the highest particle density denotes a higher number of adhesion complexes (Figure 4.20). The adhesion complexes link the F-actin to the substrate, which can result in the RF attenuation and therefore promoting growth cone spreading. However, during axon growing, the growth cone is highly dynamic, which is correlated with the association and dissociation of adhesion complexes.[40, 184, 186-187] Thus, the mechanosensitivity of the growth cone is highly determined by whether adhesion forces, $F_{adhesion}$, can be transmitted to the F-actin before or after the adhesion complexes dissociate.[38] It has been reported that the availability of ligands on the surface regulates the levels of surface receptor expression (integrin) of neurons by affecting the rate of receptor degradation.[188] Specifically, neurons express a high number of receptor at the low lanimin ligand availability and vice versa. The increased number of surface receptors at the low ligand density is associated with long lifetime of receptors, which increases neuron adhesion as well as neurite outgrowth. In contrast, the significant faster rate of receptors removing from the cell surface at the high ligand density results much shorter lifetime of receptors, which lowers the rate of neurite outgrowth.[188] Therefore, it can be assumed that the fewer and short lifetime of point contact adhesions on SB AuNPs at high particle densities disrupts the transmitted forces, which are necessary for growth cone protrusion and fast axon outgrowth.

The neurons on high particle densities which is sufficient for neuron adhesion tend to expend their cell morphologies as well as growth cone size rather than elongating their neurite length. This observation was also indicated by a recent research, in which increase in growth cone size is correlated with decrease in axon length.[189] It was also reported that the globe RF of growth cone is contributed by not only myosin contractile activities and but also actin-network treadmilling.[185] The bigger growth cone size of neurons for high particle densities might be associated with high global RF, which reduces the rate of neurite outgrowth.[190] A clearer investigation of neurite out growth depending the particle density and ligand density of SB NPs will be also discussed in the next section, when the influence of SB AuNPs on neuron adhesion and neuritogensesis by different particle distributions is investigated.

4.6 The influence of ligand distributions between order and disorder

In sections 4.3, 4.4 and 4.5, the influences of the particle size, density, and surface coupling strength on neuron adhesion and neuritogensesis have been thoroughly discussed. It has been observed that the surface coupling strength of AuNPs strongly affects the neuron survival and neurite outgrowth. Specifically, the WB AuNPs can cause cytotoxic effects on the neuron survival, while noticeable toxicity is not observed for the case of SB AuNPs. Moreover, it has been found that the neuron adhesion can be equally promoted by a similar ligand density for different particle sizes and densities. By the same number of ligands in a unit area, a low number of big AuNPs can mediate cell adhesion similarly as a high number of small AuNPs. This refers to a locally sufficient ligand density, which is more essential for the cell adhesion than inter-ligand distances. However, it was reported that a threshold inter-ligand distance of sub-70 nm is required for cell adhesion.[14, 191-192] In these studies, an average RGD ligand spacing of beyond 70 nm dramatically reduces the cell adhesion and spreading of osteoblasts. The important role of lateral spacing of ligands was also confirmed by other groups for dorsal root ganglion (DRG) neurons.[1, 137]Although different cell types including neurons have been studied, all research used specific ligands for studying cell adhesion. Therefore, in this section, the influence of particle distributions of AUT-AuNP with different sizes and densities on neuron adhesion and neurite outgrowth is examined. The highly ordered and disordered SB AuNPs can be prepared by the micelle nanolithography method, which is free cytotoxic effects on neurons as compared to the WB AuNPs (see in section 4.4). First, a statistical quantification of cell survival on ordered and

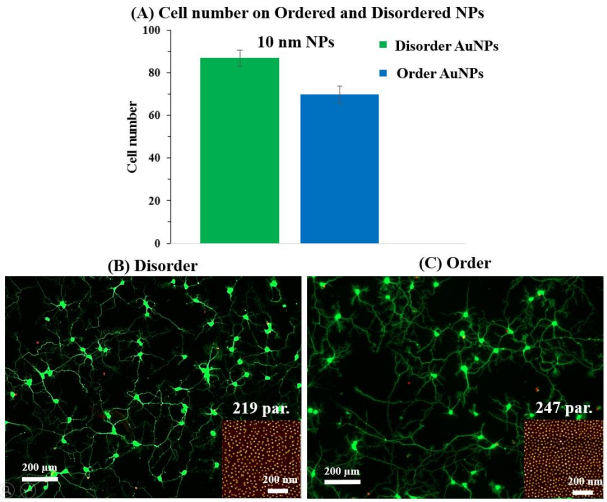

Figure 4.22 A) The statistical quantification of neuron survival on 10 nm AuNP synthesized by the micelle method for both ordered and disordered particles. (B-C) Fluorescent micrographs of neurons labelled for live cells (green) and dead cells (red) of the disordered array (B) and ordered array (C) with their inset images of AuNPs respectively (Experiment is repeated at least three times, N=6; the variations shown by standard error, SE).

disorder arrays of around 10 nm AuNPs, Figure 4.22. In this experiment, both the ordered and disordered AuNPs are prepared by the micelle nanolithography method (see section 4.1.1). Obviously, even at a lower particle density of 219 disordered particles μm^{-2} (average distance: 69 ± 3.4 nm) (Figure 4.22B) as compared to about 247 ordered particles μm^{-2} (average distance: 56 ± 1.3 nm) (Figure 4.22C), a noticeable better cell survival was observed for the cells on the disordered array (Figure 4.22 A).

To further study the influence of particle distributions on neuron adhesion, 5 nm, 10 nm, and 20 nm SB AuNP arrays of different densities are prepared by the micelle nanolithography with highly ordered particle distribution (see section 4.1.1, Table 4.1). The chemical modifications of the AUT ligand functionalized AuNPs and PEG background passivation are performed as described before. To evaluate the influence of ordered and disordered particle distributions, neuron survival on different sizes and densities of the ordered AuNPs is compared to the cell survival of neurons on the SB disordered AuNPs with similar sizes and densities (see section 4.3, Table 4.4). The statistic quantification of live cell number depended on the average particle distance (correlating with the particle density) to is analyzed for both ordered and

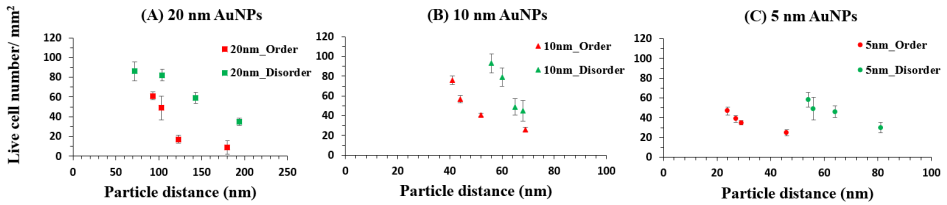

Figure 4.23 The dependence of live cell number on the particle distance for ordered and disordered AuNPs of different sizes (A) 20 nm, (B) 10 nm, (C) 5 nm AuNPs (Experiment is repeated at least three times, N=6; the variations shown by standard error, SE).

disordered AuNPs, Figure 4.23. From the graphs, it can be seen that the cell survival decreases with the inter-particle distance for all particle sizes of both distributions. However, by the same distance of each particle size, the neuron survival is noticeably higher for the cells on the disordered particles than the cells on the ordered particles. This result indicates that even at a higher inter-particle distance (lower particle density), disordered AuNP arrays can provide better neuron adhesion than those of the ordered AuNP arrays with a smaller inter-particle distance (higher particle density). The inhomogeneous ligand distributions of the randomly disordered AuNPs results in unequally distributed local ligand densities, while the homogeneous ligand distributions of the highly ordered NPs results in equal locally ligand densities on the surface. The better cell survival of neurons on the disordered NP array is induced by locally high particle density, which provide sufficient ligand molecules required to support the cell adhesion. This result is consistent with the observation reported by Spatz et al. for studying the impact of order and disorder patterns on osteoblasts.[14]. However, a different mechanism of cell adhesion is supposed due to the nonspecific ligands AUT used in this work as compared to the specific ligand (RGD) used by Spatz et al.

Generally, significant bigger slopes for the cell density/particle distance are observed for the disordered AuNPs. Interestingly, the difference in cell survival between ordered and disordered AuNPs is more apparent for the 5 nm and 10 nm AuNPs (Figure 4.23B, C), whereas it is smaller for 20 nm AuNPs (Figure 4.23A). At relative large particle distances for 5 nm and 10 nm AuNPs, the cell survival is very poor for both particle distributions. In the case of disordered 20 nm AuNPs, the cell survival almost stabilizes at about 85 cells /mm^2, when the particle distance is lower than 104 nm (98 particles /μm^2). A regularly sharp decrease in the cell survival down to about 35 cells /mm^2 is observed when the particle distance increases to 194

nm (18 particles /μm^2). However, for the cells on the ordered AuNPs, very poor cell survival (under 20 cells /mm^2) is found at large particle distances (from 123 nm to 180 nm). Interestingly, when the particle distance decreases from 123 nm to 93 nm (density increased from 56 to 90 particles μm^{-2} respectively) the cell survival is enhanced by a remarkable increase, even with a steeper slope (1.45 cells /nm) than the cells on the disordered AuNPs (0.52 cells /nm). The sudden decrease in the cell survival for the ordered 20 nm AuNPs at the range from 123 nm to 180 nm indicates beyond threshold particle distance for promoting the cell adhesion. In case of 5 nm and 10 nm ordered AuNPs, small sizes result in a significantly lower ligand density, which might be insufficient to support the cell survival as observed in the case of 20 nm ordered AuNPs. Obviously, within the used range of particle distances, the cell survival is still in the increasing phase for the 5 nm and 10 nm AuNPs with decrease in the particle distance, while the cell survival saturates for the 20 nm AuNPs. Noticeably big increases of cell survival are only observed for 10 nm and 5 nm AuNPs when the distance is lower than 52 nm (Figure 4.23B) and 29 nm (Figure 4.23C) respectively. From these observations, although disordered AuNPs facilitate a noticeable better cell adhesion, a certain sufficient ligand density is compulsorily required for the cell adhesion in the both particle distributions.

To compare the influence of the ligand distribution and the ligand density on neuron adhesion and neuritogenesis, the cell survival and neurite number are plotted versus both the particle density and ligand density, Figure 4.24. Overall, it can be seen that both live cell and neurite number increase by steeper slopes for bigger particles sizes when the density increases (Figure 4.24A, C). In agreement to the Figure 4.23, the disordered AuNPs can significantly enhance not only the cell survival, but also the neurite number as compared to the case of ordered AuNPs, especially small 5 nm and 10 nm particles. However, when the particle densities are converted to the ligand density (Figure 4.24B, D), the difference between particle sizes becomes smaller for each type of particle distributions. More importantly, the live cell and neurite number variation by the ligand density are both apparently higher for the case of disordered AuNPs, and generally independent of particle sizes. This observation confirms that the cell survival and neurite number are still strongly regulated by the ligand density, which is analogous to the case of the WB AuNPs, as discussed in section 4.3, Figure 4.10. Both particle distributions show that the cell survival and neurite number increase significantly with the ligand density and reaching the saturation from the ligand density of around 3 - 4 x 10^5 ligand

per µm^2. This value is smaller than the value of 7.5 x 10^5 ligand per µm^2 for the case of the WB AuNPs (Figure 4.11). The mechanotransduction of neurons for different particle coupling strength might contribute to this difference since all particles here are SB AuNPs. Moreover, as compared to the SB AuNPs, a higher particle density of WB AuNPs is required to compensate the particle uptake.

More importantly, the ordered and disordered particle arrangements show a certain influence of the ligand distribution on the neuron adhesion and neuritogensesis. To some extent, the better cell survival and higher neurite number of neurons on the disordered AuNPs might be correlated to the model of focal adhesion (FA) complex formation as reported by Spatz et al.[4, 14] For osteoblasts, the nanometer inter-distance of specific ligands (RGD) is crucial to induce the clustering of FAs for the cell adhesion. Only spacing smaller than 70 nm between two neighboring particles can induce the FA formation. The FA clustering and the related

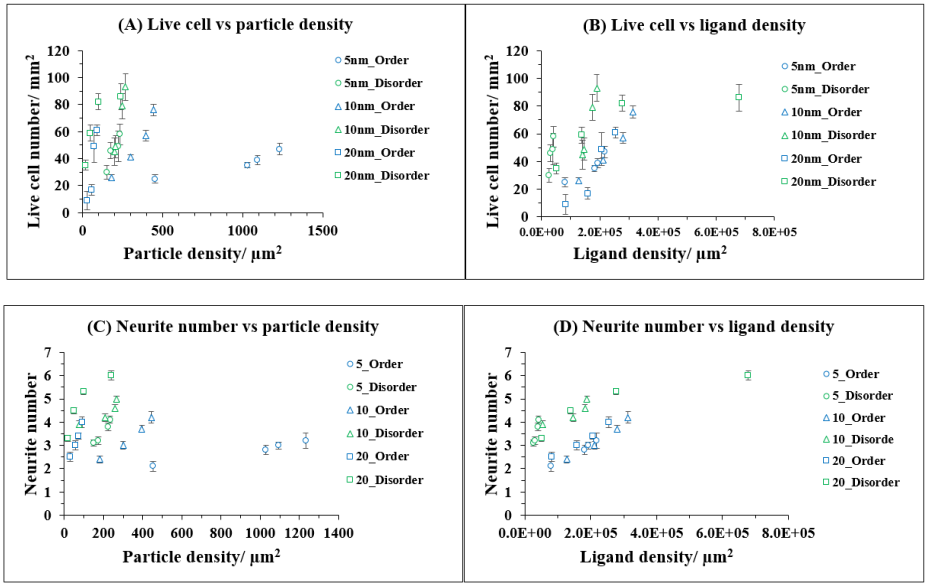

Figure 4.24 Dependence of live cell and number on particle density (A) and ligand density (B) for different particle sizes and distributions. Dependence of neurite number on particle density (C) and ligand density (D) for different particle sizes and distributions (Experiment is repeated at least three times, N=6; the variations shown by standard error, SE).

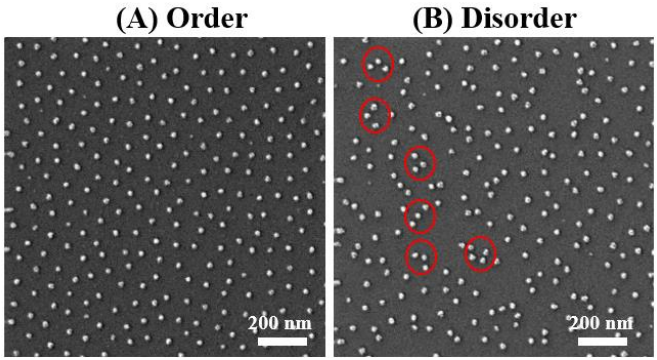

Figure 4.25 10 nm AuNP arrays of highly ordered (A) and disordered (B) distributions. The average distances of particles are about 94 nm for both ordered patterns, but the disorder possess many dense particle groups, in which the particle distances are smaller than 94 nm (indicated by the red circles).

integrin linkage between the substrate and the F-actin cytoskeletal results in better cell adhesion. The inter-particle distance bigger than 70 nm will not mediate the formation of FA or the integrin clustering, therefore resulting in poor cell adhesion.[14] Although the adhesion complex formation has been still not fully elucidated for neuronal cells, consistent observations for DRG neurons cultured on the DM-GRASP-functionalized AuNPs were confirmed by Pollerbeck et al.[1, 137] The ordered AuNP array with a interparticle distance of 58 nm can increase the cell adhesion (up to 4 to 5-fold) as compared to the AuNP array with the interparticle distance of 73 nm. At a similar particle density (or an averaged inter-particle distance), for disordered AuNPs exist many groups of particles, which are close enough to induce cell adhesion, Figure 4.25 (some of them indicated by red circles, for example). At the local sub-threshold distances of some particles gathering in the case of disordered AuNP array might support cell adhesion, which is not the case for ordered array with a homogeneous particle distribution. It can be derived that the local density of the AUT ligand, which is contributed by not only the inter-particle distance (density), but also the particle size and distribution is the critical parameter for regulating neuron adhesion.

To demonstrate the further influence of the particle distribution on neuritogensesis, the average axon length of a neuron is also statistically quantified and displayed versus the particle density and ligand density for both ordered and disordered patterns, Figure 4.26. A clear decrease in neurite length before reaching a saturation is observed for all particles when the

particle density increases (Figure 4.26A). The neurite outgrowth reduces dramatically in the range below 400 particles per μm^2. At higher particle density, the axon length almost stabilizes at a value of around 120 µm. Moreover, the dependence of the neurite length is independent of the particle sizes and distributions. Although a sufficient particle density is required for the cell adhesion, small 5nm AuNPs induce the neurite outgrowth as similarly as 10 nm and 20 nm particles. The consistence of the curve in each particle size indicates a negligible influence of the particle distributions. However, when the neurite length is plotted versus the ligand density, the dependence of neurite length is varied by the particle sizes (Figure 4.26B). In fact, all curves that are matched together when plotted versus particle density now separate from each other. Moreover, it can be seen that the particle distributions do not affect axon elongation at the same particle size. However, a size effect is observed on axon length for each particle size. At the same ligand density, bigger particles promote axon elongation better than smaller particles. Moreover, comparing the dependence of axon length on the ligand density for both SB (Figure 4.26b) and WB (see Figure 4.11B) AuNPs shows that the ligand density range that causes decreasing axon is much smaller for SB AnNPs. This indicates that the axon elongation is mainly controlled by mechanotransduction for unspecific neuron binding. In fact, the particle coupling strength has been found to be a key contribution to this neurite growing behavior as discussed before (see section 4.5). The neurite outgrowth behavior on different particle densities can be explained based on the model of growth cone extension as suggested in Figure 4.21. From the suggested growth cone model, the strong coupling of SB AuNPs on the substrates (high $F_{coupling}$) allows the cell traction forces to be transmitted to the substratum, which strongly affects the axon elongation rate. At low availability of adhesion sites (particle density), neurons

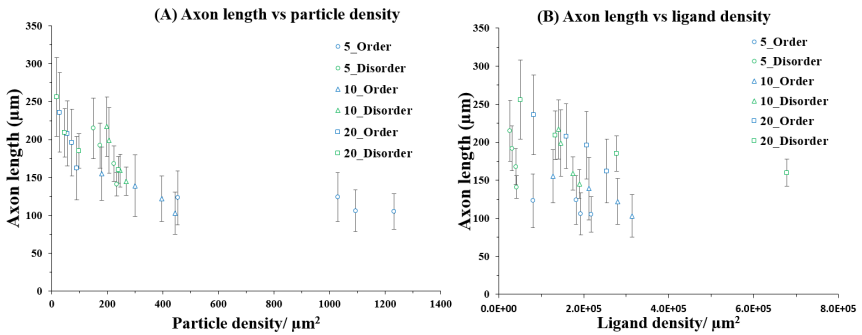

Figure 4.26 Dependence of axon length on particle density (A) and ligand density (B) for the SB AuNPs of different sizes and distributions (Experiment is repeated at least three times, N=6; the variations shown by standard error, SE).

tend to strengthen their adhesion to the substratum by expressing a high number of surface receptors. This allows transmitting forces from cells to substrate, which can restrain the RF to make axon growing faster. In contrast, at higher particle densities, the increased $F_{adhesion}$ results in breaking or disassembly of the point contact adhesions, which disrupts the transmitted forces and therefore reducing the axon outgrowth rate. In other words, fewer and transient point contact adhesions (adhesion complexes) at adhesion site density shortens force transmitting time between cells and substrate, which results in small reduction of the RF. Therefore, at higher particle densities, axons grow at lower rate and tend to spread bigger growth cone size rather than elongation (see Figure 4.20).

Overall, the disordered patterns can provide a noticeable higher capability of neuron adhesion and neurite number than the ordered patterns. The cell survival and neurite number increase sharply with the ligand density before reaching a plateau. The inhomogeneous distributions of disordered AuNPs create locally high ligand densities, which can support the cell adhesion, while it is not the case for the ordered AuNPs with homogeneous particle distributions for low particle densities. However, there is no influence of the particle distributions on the neurite outgrowth. The axon elongation is strongly controlled by mechanotransduction, which is mainly affected by the particle coupling strength. The axon length decreases with increasing particle density as both ordered and disordered SB AuNPs are used in this study. At relatively high particle densities, the observed short axon outgrowth might be also a consequence of the high charge (ligand) density, which affects the cells on both the SB and WB AuNPs.[140-141]

4.7 The regulation of cell adhesion by enoneuraminidase (endo-N) enzyme

The polysialic acid (PSA) associated with neural cell adhesion molecule (NCAM) on cell membrane can regulate both cell-cell and cell-substrate adhesion.[59] The PSA-NCAM is also required to induce developing neurons and synaptic plasticity.[20, 57-58] The level of PSA attached to NCAM is regulated by a specific neuraminidase (endo-N) enzyme controlling cell-cell aggregation.[59] In this thesis, the neuron adhesion is found to be mainly mediated by the unspecific electrostatic interactions between the negatively charged PSA moiety of NCAM and the positively charged AUT-AuNPs. Although the cell adhesion is obviously depended on the ligand density (surface charge) as described in aforementioned sections, further investigations

of neuron adhesion are performed by using the endo-N to remove the PSA from NCAM which provides the unspecific natural of neuron adhesion. To perform this study, 20 nm AuNPs with density of 90 particles μm^{-2} were prepared by the micelle nanolithography as nanoplatforms for either AUT or PA22 functionalization. Here the integrin derived ligands PA22 and laminin coated silicon substrates are used control samples. The endo-N enzyme is added to the culture medium of neurons plated on the AUT, PA22, and laminin samples at the same time after cell seeding. The live and dead cell staining micrographs of neurons were taken after 3 DIV on the respective samples with and without adding the enzyme, Figure 4.27A-F. The statistical quantification of the relative cell survival for the different samples with and without enzyme addition is shown in Figure 4.27G. The relative cell survival for each sample was determined by dividing the absolute live cell number of each sample by the absolute live cell number of laminin sample for each culture experiment.

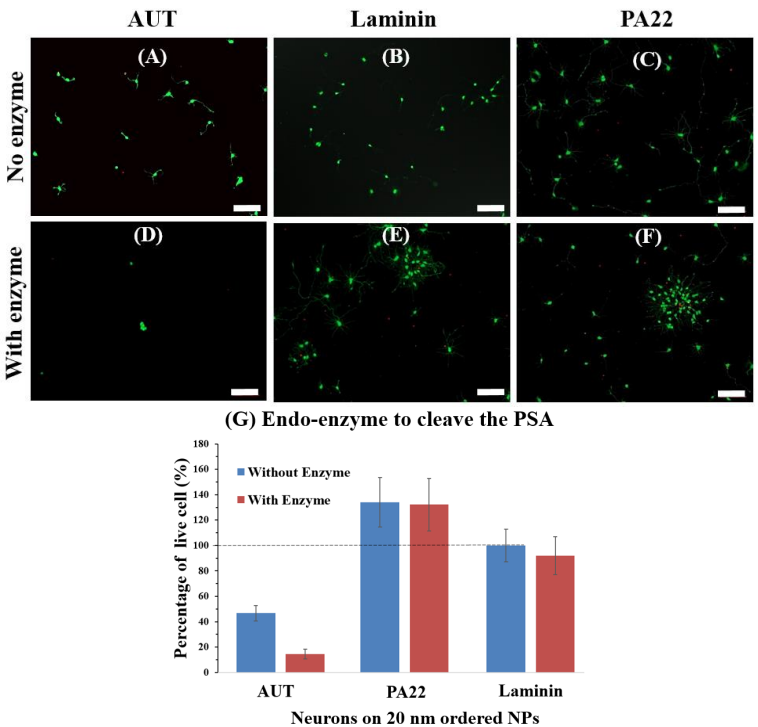

Figure 4.27 (A-F) Fluorescent micrographs of neurons labelled for live cells (green) and dead cells (red) of the AUT, PA22, and laminin samples with and without Endo-N enzyme using. G) The statistical quantification of a relative neuron survival on these samples. (compared to laminin control samples) (Experiment is repeated at least three times, N=6; the variations shown by standard error, SE). Scale bar: 100 µm

In case of the nonspecific AUT ligands, an obvious contrast of the live cell number is observed between samples without adding enzymes (Figure 4.27A, D). Although the difference of live cell number is not apparent between samples without (Figure 4.27B, C) and with adding enzyme (Figure 4.27E, F) for the specific ligands of PA22 and laminin, a noticeable cell aggregation can be observed in enzyme added samples. The statistical quantification confirms a dramatic reduction of the cell survival after adding the enzyme for AUT-AuNP samples, while only little changes in cell survival are found for laminin control samples, Figure 4.27G. The removal of PSA from NCAM by the specific endo-N enzyme cause a strong effect on the cell survival for the case of AUT ligand. The complex glycocalyx proteins associated with NCAM possess a very unusual structure including one or more relative long unbranched homopolymers of alpha 2, 8-linked PSA residues, which are specifically required for certain molecular interactions.[59, 193-194] The highly negative charge of the long PSA chains can not only regulate the cell-cell interactions, but also mediate cell-substrate adhesion through cationic ligand cues immobilized on the substarte.[195] The Endo-N specifically cleave alpha 2, 8-linked PSA resulting in a reduction of the membrane-membrane repulsion between cells.[193] Therefore, the removal of PSA obviously results in a cell aggregation as can be seen particularly for PA22 and laminin samples, Figure 4.27D-F.

Moreover, the cell survival is strongly reduced for AUT ligand after enzyme adding due to the removal of the negatively charged PSA associated to the NCAM on cell membrane. This confirms that the PSA is crucial for inducing cell adhesion through the electrostatic interactions on the AUT-AuNPs. This observation also agrees with the cases of charge variations by controlling particle sizes, densities, and ligand concentrations as discussed in the section 4.2. In contrast, when the cell adhesion is specifically mediated via the integrin-specific binding ligands PA22 and laminin, a minimal change in cell survival is observed for enzyme containing and enzyme-free samples. This indicates an unimportant role of the glycocalyx for specific cell adhesion. The significant higher cell survival on the PA22 ligand over the AUT ligand (Figure 4.27G) also proves a different cell mediated adhesion mechanism for each type of ligand. The integrin specific ligand could enhance cell adhesion by inducing stable adhesion complexes formation that directly links the cell cytoskeleton on the substrate.

4.8 Control of neuron adhesion by positive ferritin nanoparticle pattern

The spatio-temporal patterns of biochemical ligand cues play a crucial role for neuronal network guidance. Nano and microfabricated biochemical patterns can regulate the neurite outgrowth to respond to the topographical features of their environments.[70] The combination of top down lithography and bottom up self–assembly allows to take advantages of both methods for fabricating nanostructured biochemical patterns, which can be used to study cell adhesion and development. From our preliminary results, Gilles and Li demonstrated patterns of discrete gradient lines with different slopes for neuronal guidance by combining nanoimprint lithography and e-beam lithography with self-assembly AuNPs immobilization.[23, 25, 62]

Moreover, protein cage architectures such as ferritins are versatile nanoscale platforms for biological applications. Recently, Beck at al. have shown that the total charge of ferritins can be engineered to possess net positive or negative surface charge, while the nanocages of ferritins can be loaded with different inorganic NPs, such as cerium oxide or cobalt oxide.[32] This feature enables fabricating a nanostructure substrate of ferritins loaded metal NPs for controlling cell adhesion potentially. The positively or negatively charged surface of ferritin NPs (FerNPs) can act as cell adhesive or repulsive cues, which regulate cell adhesion through electrostatic interactions. In the line of using metal NPs for controlling neuronal adhesion, in this section, the positively charged FeNPs are used instead of the AUT-AuNPs for controlling the neuron adhesion and neurite guidance. Importantly, FerNPs can be loaded by different magnetically nanoparticles such as cerium oxide, ion, and cobalt NPs inside their cores, which possibly allows controlling of cell adhesion from externally magnetic fields.

4.8.1 Ferrin nanoparticle pattern fabrication

To perform this work, 6 nm positively charged FerNPs loaded with cerium oxide NPs, are prepared by Beck et al.[32], which can be used to immobilize the particles on negatively charged surfaces such as SiO_2 or glass. The FerNPs can be decorated on silicon substrates with different particle densities, Figure 4.28. The FerNPs are straightforwardly immobilized onto the substrate by electrostatic interactions between the positive charge of FerNPs and the native negative charge of the SiO_2 layer. The electrostatic interaction enables a stably particle binding onto the surface, even thoroughly rinsing steps are performed after the particle immobilization. Moreover, the binding of the FerNPs to the surface is very straightforward and even no plasma

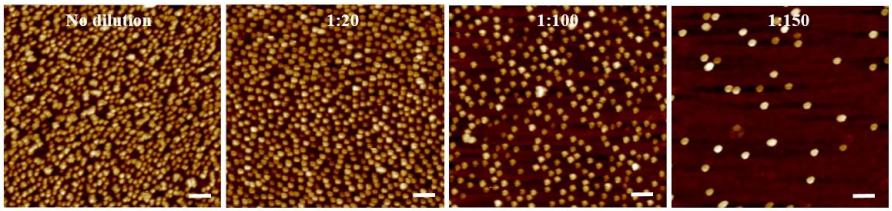

Figure 4.28 Positively charged FerNPs attached on SiO_2/Si substrates with different densities obtained by incubating the substrates in FerNP solutions of different diluting ratios in milliQ water. Scale bar: 100 nm.

activation step is required for the silicon substrate before particle incubation. In addition, by diluting the FerNPs solution, different particles densities can be obtained by using the using a same incubation time. Thus, verifying the FerNP density will directly result in surface charge density, which can be considered as similar to the case of tuning the surface charge by controlling the AUT-AuNP density. In order to control the neuron adhesion by the FerNP array, the background is also essential to be passivated by the cell aversive molecules. The trichloro(1H,1H,2H,2H-perflueooctyl) silane (FOTCS) (Sigma-Aldrich) is used for passivation. It can be chemically attached on the silicon surface by gas phase deposition (45mbar, 90 min) in a desiccator inside the glovebox.

Moreover, by using of the lithography technique, microstructured patterns on silicon wafers are fabricated in the HNF clean room, which are used as molds for preparing poly(dimethysiloxane) (PDMS) stamps.[196] The silicon mold has repeating stripes with lines of 10 μm widths and 20 μm spacing. The PDMS is first prepared by mixing the elastomer base with curing agent with a ration 10:1 (base: curing agent) and stored at 4^o overnight to remove the bubbles. Before making the PDMS stamp, the silicon mold is passivated by the FOTCS to obtain hydrophobic surface for preventing the adhesion of PDMS. 2 ml of the PDMS solvent is poured into the silicon mold put in a petri dish and curing at 60^o for 6 hours. In the next step, the PDMS stamp is removed from the silicon mold and cut with open path for liquid inlets. Both the PDMS stamps and clean silicon substrates are activated by oxygen plasma (20s, 1.4 mBar, 100W) for generating a hydrophilic surface. The PMDS stamp is put on to the silicon substrate. Then the colloidal FerNP solution is dropped into the inlets. The liquid will flow into the microstructures of PDMS stamps by capillary force and incubated for 30 min. Finally, FerNPs can be decorated on the silicon substrates with particles patterns through the PDMS stamp. In

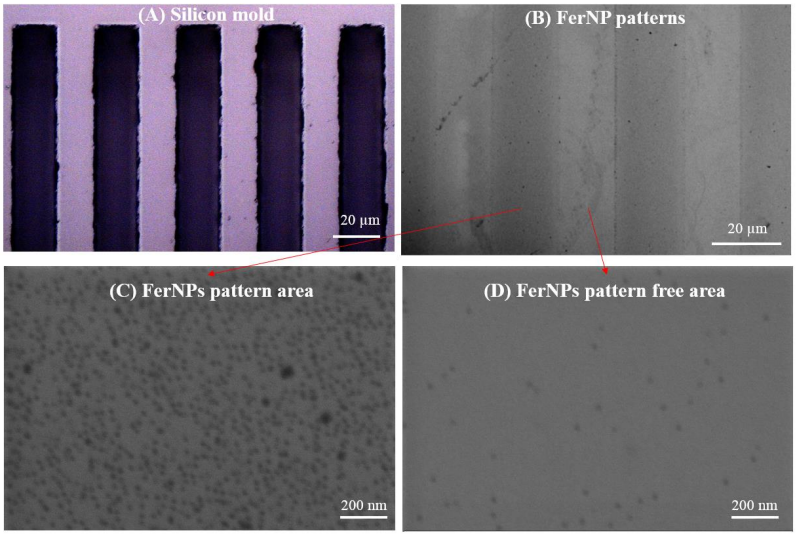

Figure 4.29 Positively charged FerNPs patterns fabricated by using the silicon mould (A). A PDMS stamp replicated by the silicon mould is used for fabricating the FerNP patterns as shown by the SEM image (B). The pattern area is decorated with a high density of FerNPs (C), while the pattern free area is almost no particles (D).

figure 4.29B-D, the SEM images of FerNP patterns on the silicon substrate is shown prepared from a silicon mold, which is imaged by an optical microscopy (Figure 4.29A, the layout of structure is shown in Figure A4.12, Appendix B). The density of FerNPs on the designed patterns (594 ± 69 particles/μm^2, in Figure 4.29C) obviously overwhelms the undecorated areas (78 ± 7 particles/μm^2, Figure 4.29D).

4.8.2 Cell culture on the Ferrin nanoparticle pattern

Neurons with density of 30.000 cells per mL are cultured on FerNP patterns and different control samples. For the cell culture, the control samples are important to eliminate artifacts from the sample preparation. Since the PDMS stamp can leave PDMS residues on the silicon substrate, a control sample which has been in contact only with the PDMS stamp has been prepared for cell culture experiments. Moreover, a FerNP pattern sample without FOTCS passivation and the sample with only the FerNPs decorated silicon substrates (with and without FOTCS passivation) are used as further control samples. The fluorescent images of neurons labelled with calcein for live cells (green) and ethidium homodimer for dead cells (red) are

recorder for samples with FerNP pattern and control samples at 3 DIV (Figure 4.30A-F). The cell survival is statistically quantified for each sample (Figure 4.30G). Obviously, the backfill shows a strong effect on the cell survival. The cells on only FerNP (Figure 4.30A) or FerNP pattern (Figure 4.30D) samples with the backfill show a noticeable lower number of live cells as compared to the case of no backfill applying (Figure 4.30B, E). The bare silicon samples with backfill (Figure 4.30C) and the bare silicon sample (after removing the stamp) with backfill (Figure 4.30F) show almost no cell survival. This indicates that the backfill can extremely well prevent the cell adhesion. Possible residues left from the PDMS stamp does not support the cell

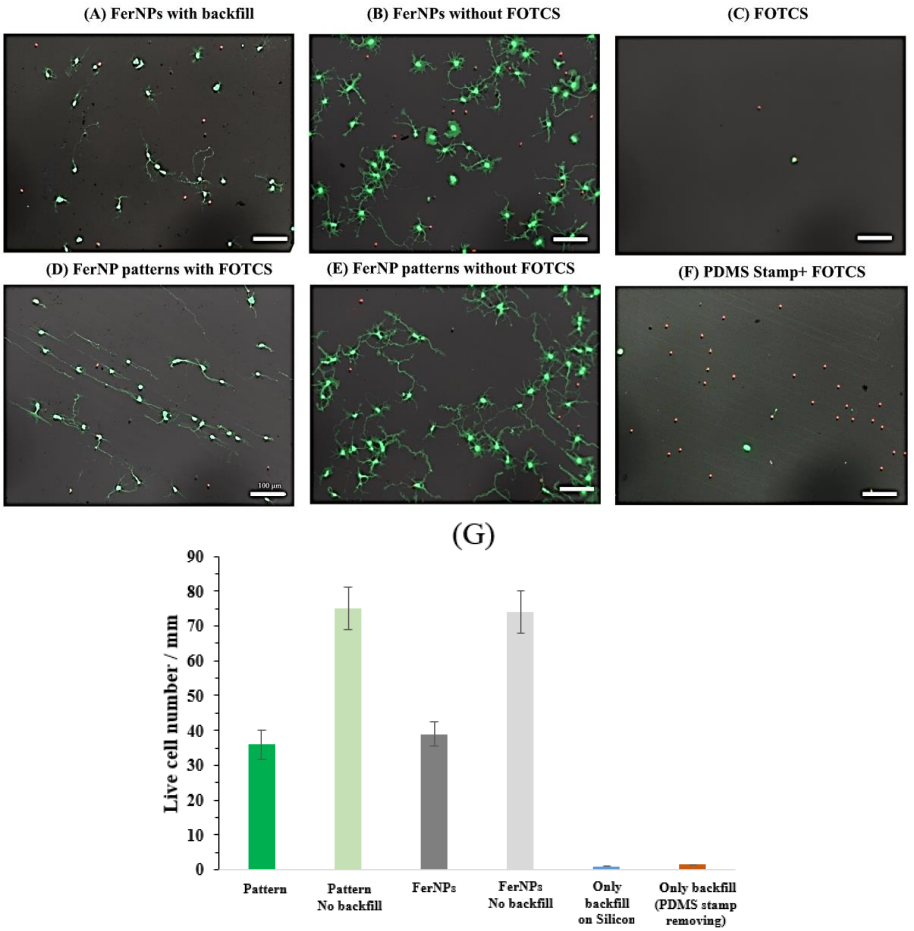

Figure 4.30 Live/dead fluorescent images of 3 DIV neurons on a FOTCS passivated (backfill) silicon substrate (A), a FerNPs immobilized silicon substrate without the backfill (B) and with only backfill (C), FerNP patterns with the bacfill (D) and without the backfill (E)a sample with residue of PDMS after removing the stamp with the backfill (F). The statistical analysis of live cell number for each sample respectively (G). Scale bar: 100 µm

adhesion. From the statistical quantification of cell survival (Figure 4.30G), the FerNP pattern and FerNP decorated samples with backfill show their capability for supporting neuron adhesion by exhibiting a live cell density of about 40 cells /mm^2. This cell survival number seems to be significantly higher than the cell survival on 5 nm WB AuNPs (see Figure 4.10A), and is comparable with the cell survival on 5 nm SB AuNPs (See Figure 4.14A). Although the cytotoxicity of FerNPs and their surface coupling strength are not investigated in this work, their better cell adhesion supporting capability compared to the AuNPs of the similar size might be correlated to their biocompatible properties.

Moreover, by statistically quantifying the percentage of cells that possess axons aligning along the FerNP patterns over total number of cells for each image (Figure 4.30D), a guiding effectiveness of 88% is obtained indicating a high chemical contrast by between the FerNP patterns and the FOTCS backfill. This guiding effect is significantly higher than the about 26% of the FerNP pattern without backfill applying (Figure 4.30E). The optical contrast of FerNP patterns on the microscope is too poor for calculating the guiding efficiency based on the area of cells on and beside the patterns. Therefore, in this work, the guiding efficiency is based on the percentage of cells, which possess axons aligning parallel to the patterns (Figure A4.13, Appendix B) over total cells in a unit area. The guiding effectiveness quantified for the FerNPs is different from the method which was reported by S.Gilles[25] and P.Li.[23] Nevetherless, the guiding efficiency of 88% for the FerNP pattern is comparable to a guiding efficiency of 92% for the AUT-AuNP patterns with FOTCS backfill as reported by P.Li.[23] For the first time, neuron adhesion and neurite outgrowth are controlled by the positive FerNP patterns with metal nanoparticles loaded inside FerNPs'nanocages. The capability of loading Ferritin magnetic NPs potentially allows the selective control of the cell adhesion by using an external magnetic field.

CONCLUSIONS AND OUTLOOKS

In the scope of this thesis, neuron adhesion and neuritogenesis have been studied by using gold nanoparticles (AuNPs) in sub-50 nm range with controllable particle sizes, densities, surface coupling strength and distributions as ligand nanocarriers. Non-specific chemical ligands, 11-amin-1-undecanthiol (AUT) molecules, are functionalized on AuNPs for cell adhesion, while background is passivated by cell aversive molecules, 2-[methoxy(polyethylenoxy)6-9 propyl] trichlorosilane (PEG). For the first time, the influences of all chemical ligand densities, ligand distributions, and substrate coupling strength on neuron adhesion have been presented and elucidated. This provides a better understanding of neuron-non-biomaterial interactions for designing neurobioelectronic devices or long-time in-vitro cell cultures.

For fabrication processes, highly ordered AuNPs with different sizes and densities have been synthesized by the block copolymer micelle nanolithography using poly(styrene-b-2-vinyl pyridine) polymers. The particle sizes are controlled by using different molecular weights (MWs) of the polyvinyl pyridine part or amount of gold precursor loading, while the particle densities are tuned by using different MWs of the polystyrene part or changing the dip-coating speed. On the other hand, the disordered AuNPs were produced by either the micelle nanolithography with adding polystyrene polymers or the particle immobilization using the self-assemble salanization method. Interestingly, by changing the oxygen plasma treatment, weakly bound (WB) and strongly bound (SB) AuNPs can be fabricated. A 2 min plasma exposure to the cit-AuNPs immobilized silicon substrate caused WB particles, while a longer plasma exposure of 30 mins produced SB AuNPs. The surface coupling strength was characterized and confirmed by atomic force microscopy (AFM) technique. The AFM and also other advanced techniques such as scanning electron microscopy (SEM), and X-ray photoelectron spectroscopy (XPS) have been used to characterize the nanostructures and chemical modifications.

Neuron adhesion and development have been characterized after three days of culture for samples modified by AuNPs with different sizes, densities, surface coupling strength, and distributions. It is found that neuron survival and neurite number are strongly regulated by the ligand density for all cases. In general, cell survival and neurite number increase with the rising ligand density and reach a plateau for all particle sizes. Although this indicates that cell adhesion mediated by non-specific AUT ligands can be considered as homogenous electrostatic

interactions, the local distribution of adhesion spots (particles) plays an important role in cell adhesion. Neurons cultured on samples decorated by SB 5 nm, 10 nm, and 20 nm AuNPs with different densities are statistically investigated for both ordered and disordered particles. At the same ligand density, it is observed that disordered AuNPs provide noticeably better capability for cell survival as well as neurite number than ordered particles. Better cell survival and neurite number for disordered AuNPs are explained by the unequal particle distributions between ordered and disordered AuNPs. Even by a similar particle density (ligand density), disordered AuNPs can provide locally high ligand densities in sub-areas, while it is not the case for ordered AuNPs. Although this observation is consistent with findings reported by Spatz et al.[14] for osteoblasts or Pollerbeck et al.[1, 137] for DRG neurons, non-specific chemical ligands used in this work mediate cell adhesion in a different mechanism as compared to specific ligands used in their studies. The investigation of neuron adhesion by non-specific AUT ligands in this work indicates that local ligand densities contributed by all particle densities (inter-particle distances), sizes and distributions are critically required for supporting cell adhesion. Moreover, the strong influence of the ligand density on neuron adhesion via electrostatic interactions is also confirmed by using different ligand concentrations or removing the PSA molecules from NCAM with a specific endoneuraminidase (endo-N) enzyme. In both cases, a reduction in either ligand density (positive charge number) or the negative charge of PSA-NCAM on the cell surface result in decreasing neuron adhesion. More importantly, it is revealed that the surface coupling strength of AuNPs in sub-20 nm has strong effect on cell adhesion and neruite development. A particle uptake and severe cytotoxic effect of loosely bound surface are observed for WB 5 nm, 10 nm, and in parts for 20 nm AuNPs, while SB AuNPs of the same size and density remain at the surface and have no decreasing effect on the neuron survival as well as neurite number. Although the number of particles applied to the system is relatively low, the effect of these surface confined particles can be more detrimental to the cells than colloidal particles added to the culture medium in big excess. These observations indicate an alteration of particle uptake towards higher efficiencies for surface confined AuNP in comparison to colloidal particles. It can be assumed that similar cytotoxic effects of loosely bound nanomaterials can occur also for other adherent cells. Presumably, also nanoparticles originally incorporated and later released from materials of technical devices may have a severe cytotoxicity due to the confinement of the released particles to the solid/cell interface. An

evaluation of the cytotoxicity of particles associated to material surfaces seems to be recommendable especially for long term cultures with small particles and nanomaterial containing implantable systems.

Axon outgrowth is also thoroughly investigated in this work as function of particle sizes, densities, surface coupling strength, and distribution. Axon elongation responses to these particle's parameters in a different manner as observed for cell survival and neurite number. It is found that the surface coupling strength of AuNPs strongly affect axon outgrowth. For WB AuNP samples, an axon elongation increases with the rising ligand density to a peak, and then decreases before staying at a plateau. In contrast, for SB AuNPs, neurons decrease their axon lengths with the rising particle density and then saturate. This indicates that mechanotransduction plays a pivotal role regulating the elongation of axons. When neurons adhere and elongate their axon by extending the growth cone, adhesion forces ($F_{adhesion}$) are produced at point contact adhesions between the cell and substratum due to the myosin contraction activities. Whether or not the adhesion forces can be transferred from cells to the substrate depends on the surface coupling strength of the AuNPs ($F_{coupling}$). For WB AuNPs, the relative weak $F_{coupling}$ causes the dissipation of $F_{adhesion}$ or even eliminate the force if the particle coupling is broken. The rising of particle (or ligand) density increases the total $F_{adhesion}$ due to increasing contact adhesion points, which allows force transmission and activates mechanotransduction for axon growth. However, when the particle density increases to a critical value, the $F_{adhesion}$ reaches a threshold. At this value, there is presumably slippage (breaking) of adhesion at point contacts, which slows the rate of growth protrusion.[39] Therefore, the axon length on WB AuNPs increases to a peak, then decreases and stays at a plateau. On the other hand, for SB AuNPs, significantly stronger $F_{coupling}$ allows the transmission of forces between cell and substratum even at a very low particle densities. This results in much longer axon length for SB AuNPs as compared to WB AuNPs at low particle densities. Howver, for SB AuNPs, $F_{adheison}$ is already relative high, which already exceed the threshold for adhesion breaking at point contacts. Therefore, an increase in the particle density results in a reduction of axon elongation. Moreover, it is found that the particle distribution does not affect the axon outgrowth. At the same particle density, ordered and disordered SB AuNPs induce similar axon outgrowth, which is strongly controlled by the particle densities.

Last but not least, in the line of using metal nanoparticles for controlling the neuron adhesion, patterns of ferritin nanoparticles (FerNPs) have been used to control the neuron adhesion and neurite guidance. The surface net charge density of FerNPs has been engineered to possess either positive or negative net charge, while the nanocages of the FerNPs are loaded with metal NPs of cerium oxide. In this work, the positively charged 6 nm FerNP are deposited at the line patterns with 10 μm widths and 20 μm spacing for controlling the cell adhesion by combining top-down lithography technique together with bottom-up self-assembly. Similar to the AUT ligands, the positively charged surface of FerNPs acts as cell adhesion cues via electrostatic interactions, while the background is passivated by the FOTCS molecules. A high guidance efficiency of the neurite outgrowth of 88 % has been observed due to the chemical contrast difference between the FerNPs and the FOTCS backfill. Importantly, the possibility of loading magnetic metal nanoparticles inside the nanocages of FerNPs opens potential applications for advanced controlling of cell adhesion. The adherent cells on FerNPs can potentially be locally modulated or lift off by an external magnetic field such as magnetic tweezers. The control of metal NPs loaded inside the FerNPs under cell attachment can be also used for drug deliveries or cell mechanical investigations.

ACKNOWLEDGMENTS

Prof. Andreas Offenhäusser - I would like to especially thank you for giving me the opportunity to fulfil my PhD study in a friendly and great research environment. I also thank you for your support and advice in my project.

Dr. Dirk Mayer - I would like to express my deep appreciation to you, my direct supervisor, who enthusiastically guided me during my whole PhD time. Thank you very much for many meaningful advices and discussions for my work. I learnt from you not only techniques for fulfilling my PhD work, but also methods for solving problems in a lab as well as in life. Thank you very much for revising my thesis, giving me helpful comments and advices.

Prof. Ulrich Simon - I would be greatly appreciated for your insightful advices and discussions we had during my PhD time. I also thank you for the great support and revising for my publication.

Prof. Bernhard Wolfrum and Dr. Vanessa Maybeck - Thank you for supporting me to work in your lab.

Dr. Corinna Kaulen (RWTH Aachen) - I would like to thank you for your supporting experiments, which are very important for my PhD work.

Dr. Tobias Beck (RWTH Aachen) – Thank you for providing me the ferritin nanomaterials, which are very useful for my project.

Elke Brauweiller-Reuters - I am grateful for your huge time spending to help me in the FIB experiments.

Michael Prömper – Thank you very much for providing me the silicon wafer and the silicon pattern mold.

Bettina Breuer, Rita Fricke, Elmar Neuman and Stephany Bunte – I would like to thank you for all of the support which you had done for me.

Andreea – Thank you very much for help me in many experiments, especially for the cell culture and resin embedding work.

Pinggui, Sivanesan, Silke, Nouran – It was nice time to work with you, thank you for your help.

Molecular Biolelectronics group, I would like to thank all people in the group for your discussions and advices during our group and literature meetings.

My many thanks go out to **all people in our institute (ICS8)** for the warm and friendly working environment.

I thank **the ministry of Vietnamese education and training (MOET)** for the main financial support during my PhD time.

And finally I would thank **my wife**, you have sacrificed a lot of things for supporting me to fulfill my PhD work.

REFERENCES

[1] Thelen, K.; Jaehrling, S.; Spatz, J. P.; Pollerberg, G. E., Depending on Its Nano-Spacing, ALCAM Promotes Cell Attachment and Axon Growth. *Plos One* **2012,** *7* (12).

[2] Chen, C. S.; Mrksich, M.; Huang, S.; Whitesides, G. M.; Ingber, D. E., Geometric control of cell life and death. *Science* **1997,** *276* (5317), 1425-1428.

[3] Hirschfeld-Warneken, V. C.; Arnold, M.; Cavalcanti-Adam, A.; Lopez-Garcia, M.; Kessler, H.; Spatz, J. P., Cell adhesion and polarisation on molecularly defined spacing gradient surfaces of cyclic RGDfK peptide patches. *Eur J Cell Biol* **2008,** *87* (8-9), 743-750.

[4] Arnold, M.; Hirschfeld-Warneken, V. C.; Lohmuller, T.; Heil, P.; Blummel, J.; Cavalcanti-Adam, E. A.; Lopez-Garcia, M.; Walther, P.; Kessler, H.; Geiger, B.; Spatz, J. P., Induction of cell polarization and migration by a gradient of nanoscale variations in adhesive ligand spacing. *Nano Lett* **2008,** *8* (7), 2063-2069.

[5] Palecek, S. P.; Loftus, J. C.; Ginsberg, M. H.; Lauffenburger, D. A.; Horwitz, A. F., Integrin-ligand binding properties govern cell migration speed through cell-substratum adhesiveness. *Nature* **1997,** *385* (6616), 537-540.

[6] Kim, M. C.; Kim, C.; Wood, L.; Neal, D.; Kamm, R. D.; Asada, H. H., Integrating focal adhesion dynamics, cytoskeleton remodeling, and actin motor activity for predicting cell migration on 3D curved surfaces of the extracellular matrix. *Integr Biol-Uk* **2012,** *4* (11), 1386-1397.

[7] Yoo, S.; Kim, R.; Park, J. H.; Nam, Y., Electro-optical Neural Platform Integrated with Nanoplasmonic Inhibition Interface. *Acs Nano* **2016,** *10* (4), 4274-4281.

[8] Jung, S.; Bang, M.; Kim, B. S.; Lee, S.; Kotov, N. A.; Kim, B.; Jeon, D., Intracellular Gold Nanoparticles Increase Neuronal Excitability and Aggravate Seizure Activity in the Mouse Brain. *Plos One* **2014,** *9* (3).

[9] Sanchez-Fefix, O.; Dyke, J. C.; Malyutin, A. G.; Stein, B. D.; Mahmoud, W. E.; Al-Ghamdi, A. A.; Al-Hazmi, F. E. S.; Bronstein, L. M., Synthesis of functionalized monodisperse magnetic nanoparticles for bioapplications. *Abstr Pap Am Chem S* **2013,** *246*.

[10] Doria, G.; Conde, J.; Veigas, B.; Giestas, L.; Almeida, C.; Assuncao, M.; Rosa, J.; Baptista, P. V., Noble Metal Nanoparticles for Biosensing Applications. *Sensors-Basel* **2012,** *12* (2), 1657-1687.

[11] Thanh, N. T. K.; Puntes, V. F.; Tung, L. D.; Fernig, D. G., Peptides as capping ligands for in situ synthesis of water soluble Co nanoparticles for bioapplications. *Fifth International Conference on Fine Particle Magnetism* **2005,** *17*, 70-76.

[12] Novotna, Z.; Reznickova, A.; Kvitek, O.; Kasalkova, N. S.; Kolska, Z.; Svorcik, V., Cells adhesion and growth on gold nanoparticle grafted glass. *Appl Surf Sci* **2014,** *307*, 217-223.

[13] Valdiglesias, V.; Costa, C.; Kilic, G.; Costa, S.; Pasaro, E.; Laffon, B.; Teixeira, J. P., Neuronal cytotoxicity and genotoxicity induced by zinc oxide nanoparticles. *Environ Int* **2013,** *55*, 92-100.

[14] Huang, J. H.; Grater, S. V.; Corbellinl, F.; Rinck, S.; Bock, E.; Kemkemer, R.; Kessler, H.; Ding, J. D.; Spatz, J. P., Impact of Order and Disorder in RGD Nanopatterns on Cell Adhesion. *Nano Lett* **2009,** *9* (3), 1111-1116.

[15] Franze, K.; Guck, J., The biophysics of neuronal growth. *Rep Prog Phys* **2010,** *73* (9).

[16] Suter, D. M.; Miller, K. E., The emerging role of forces in axonal elongation. *Prog Neurobiol* **2011,** *94* (2), 91-101.
[17] Discher, D. E.; Janmey, P.; Wang, Y. L., Tissue cells feel and respond to the stiffness of their substrate. *Science* **2005,** *310* (5751), 1139-1143.
[18] Johnson, C. P.; Fragneto, G.; Konovalov, O.; Dubosclard, V.; Legrand, J. F.; Leckband, D. E., Structural studies of the neural-cell-adhesion molecule by X-ray and neutron reflectivity (vol 44, pg 546, 2005). *Biochemistry-Us* **2005,** *44* (28), 9824-9824.
[19] Johnson, C. P.; Fujimoto, I.; Rutishauser, U.; Leckband, D. E., Direct evidence that neural cell adhesion molecule (NCAM) polysialylation increases intermembrane repulsion and abrogates adhesion. *J Biol Chem* **2005,** *280* (1), 137-145.
[20] Quartu, M.; Serra, M. P.; Boi, M.; Ibba, V.; Melis, T.; Del Fiacco, M., Polysialylated-neural cell adhesion molecule (PSA-NCAM) in the human trigeminal ganglion and brainstem at prenatal and adult ages. *Bmc Neurosci* **2008,** *9*.
[21] Lu, S. Y.; Bansal, A.; Soussou, W.; Berger, T. W.; Madhukar, A., Receptor-ligand-based specific cell adhesion on solid surfaces: Hippocampal neuronal cells on bilinker functionalized glass. *Nano Lett* **2006,** *6* (9), 1977-1981.
[22] Lee, M. H.; Brass, D. A.; Morris, R.; Composto, R. J.; Ducheyne, P., The effect of non-specific interactions on cellular adhesion using model surfaces. *Biomaterials* **2005,** *26* (14), 1721-1730.
[23] P.Li. Control of neuronal adhesion and neurites outgrowth by biofunctionalized gold nanoparticles. RWTH Aachen, 2016.
[24] Li, P. G.; Greben, K.; Wordenweber, R.; Simon, U.; Offenhausser, A.; Mayer, D., Tuning neuron adhesion and neurite guiding using functionalized AuNPs and backfill chemistry. *Rsc Adv* **2015,** *5* (49), 39252-39262.
[25] Gilles, S.; Winter, S.; Michael, K. E.; Meffert, S. H.; Li, P. G.; Greben, K.; Simon, U.; Offenhausser, A.; Mayer, D., Control of Cell Adhesion and Neurite Outgrowth by Patterned Gold Nanoparticles with Tunable Attractive or Repulsive Surface Properties. *Small* **2012,** *8* (21), 3357-3367.
[26] Glass, R.; Arnold, M.; Cavalcanti-Adam, E. A.; Blummel, J.; Haferkemper, C.; Dodd, C.; Spatz, J. P., Block copolymer micelle nanolithography on non-conductive substrates. *New J Phys* **2004,** *6*.
[27] Kastle, G.; Boyen, H. G.; Weigl, F.; Lengl, G.; Herzog, T.; Ziemann, P.; Riethmuller, S.; Mayer, O.; Hartmann, C.; Spatz, J. P.; Moller, M.; Ozawa, M.; Banhart, F.; Garnier, M. G.; Oelhafen, P., Micellar nanoreactors - Preparation and characterization of hexagonally ordered arrays of metallic nanodots. *Adv Funct Mater* **2003,** *13* (11), 853-861.
[28] Glass, R.; Moller, M.; Spatz, J. P., Block copolymer micelle nanolithography. *Nanotechnology* **2003,** *14* (10), 1153-1160.
[29] Spatz, J. P.; Mossmer, S.; Hartmann, C.; Moller, M.; Herzog, T.; Krieger, M.; Boyen, H. G.; Ziemann, P.; Kabius, B., Ordered deposition of inorganic clusters from micellar block copolymer films. *Langmuir* **2000,** *16* (2), 407-415.
[30] Spatz, J. P.; Sheiko, S.; Moller, M., Ion-stabilized block copolymer micelles: Film formation and intermicellar interaction. *Macromolecules* **1996,** *29* (9), 3220-3226.
[31] Spatz, J. P.; Sheiko, S.; Moller, M., Substrate-induced lateral micro-phase separation of a diblock copolymer. *Adv Mater* **1996,** *8* (6), 513-&.

[32] Kunzle, M.; Eckert, T.; Beck, T., Binary Protein Crystals for the Assembly of Inorganic Nanoparticle Superlattices. *J Am Chem Soc* **2016,** *138* (39), 12731-12734.
[33] Kaech, S.; Banker, G., Culturing hippocampal neurons. *Nat Protoc* **2006,** *1* (5), 2406-2415.
[34] Preston, A. R.; Eichenbaum, H., Interplay of Hippocampus and Prefrontal Cortex in Memory. *Curr Biol* **2013,** *23* (17), R764-R773.
[35] Gumbiner, B. M., Cell adhesion: The molecular basis of tissue architecture and morphogenesis. *Cell* **1996,** *84* (3), 345-357.
[36] Sackmann, E., BIOPHYSICS How cells feel the force. *Nat Phys* **2010,** *6* (6), 407-408.
[37] Bischofs, I. B.; Schwarz, U. S., Cell organization in soft media due to active mechanosensing. *P Natl Acad Sci USA* **2003,** *100* (16), 9274-9279.
[38] Swaminathan, V.; Waterman, C. M., The molecular clutch model for mechanotransduction evolves. *Nat Cell Biol* **2016,** *18* (5), 459-461.
[39] Kerstein, P. C.; Nichol, R. H.; Gomez, T. M., Mechanochemical regulation of growth cone motility. *Front Cell Neurosci* **2015,** *9*.
[40] Thoumine, O., Interplay between adhesion turnover and cytoskeleton dynamics in the control of growth cone migration. *Cell Adhes Migr* **2008,** *2* (4), 263-267.
[41] lab, C. m. Cell Adhesion. http://www.reading.ac.uk/cellmigration/adhesion.htm.
[42] Goldmann, W. H., Role of vinculin in cellular mechanotransduction. *Cell Biol Int* **2016,** *40* (3), 241-256.
[43] Bays, J. L.; Peng, X.; Tolbert, C. E.; Guilluy, C.; Angell, A. E.; Pan, Y.; Superfine, R.; Burridge, K.; DeMali, K. A., Vinculin phosphorylation differentially regulates mechanotransduction at cell-cell and cell-matrix adhesions. *J Cell Biol* **2014,** *205* (2), 251-263.
[44] Spanjaard, E.; de Rooij, J., Mechanotransduction: Vinculin Provides Stability when Tension Rises. *Curr Biol* **2013,** *23* (4), R159-R161.
[45] Betz, T.; Koch, D.; Lu, Y. B.; Franze, K.; Kas, J. A., Growth cones as soft and weak force generators. *P Natl Acad Sci USA* **2011,** *108* (33), 13420-13425.
[46] Bidone, T. C.; Kim, T.; Deriu, M. A.; Morbiducci, U.; Kamm, R. D., Multiscale impact of nucleotides and cations on the conformational equilibrium, elasticity and rheology of actin filaments and crosslinked networks. *Biomech Model Mechan* **2015,** *14* (5), 1143-1155.
[47] Weng, S. N.; Shao, Y.; Chen, W. Q.; Fu, J. P., Mechanosensitive subcellular rheostasis drives emergent single-cell mechanical homeostasis. *Nat Mater* **2016,** *15* (9), 961-967.
[48] Ray, A.; Lee, O.; Win, Z.; Edwards, R. M.; Alford, P. W.; Kim, D. H.; Provenzano, P. P., Anisotropic forces from spatially constrained focal adhesions mediate contact guidance directed cell migration. *Nat Commun* **2017,** *8*.
[49] Bajenaru, M. L.; Yungher, B.; Luo, X. T.; Park, K.; Guy, J.; Pelaez, D.; Tse, D. T.; Chiu, D., Gene therapy with constitutively active focal adhesion kinase (FAK) promotes retinal ganglion cells survival and regeneration after optic nerve crush. *Invest Ophth Vis Sci* **2016,** *57* (12).
[50] Thievessen, I.; Fakhri, N.; McIsaac, S.; Gao, L.; Chen, B. C.; Betzig, E.; Oldenbourg, R.; Waterman, C. M., Vinculin is required for cell polarization, migration and extracellular matrix remodeling in three-dimensional collagen matrices. *Mol Biol Cell* **2011,** *22*.

[51] Nishiuchi, R.; Takagi, J.; Hayashi, M.; Ido, H.; Yagi, Y.; Sanzen, N.; Tsuji, T.; Yamada, M.; Sekiguchi, K., Ligand-binding specificities of laminin-binding integrins: A comprehensive survey of laminin-integrin interactions using recombinant alpha 3 beta 1, alpha 6 beta 1, alpha 7 beta 1 and alpha 6 beta 4 integrins. *Matrix Biol* **2006,** *25* (3), 189-197.

[52] Kam, L.; Shain, W.; Turner, J. N.; Bizios, R., Selective adhesion of astrocytes to surfaces modified with immobilized peptides. *Biomaterials* **2002,** *23* (2), 511-515.

[53] Saneinejad, S.; Shoichet, M. S., Patterned glass surfaces direct cell adhesion and process outgrowth of primary neurons of the central nervous system. *J Biomed Mater Res* **1998,** *42* (1), 13-19.

[54] StJohn, P. M.; Kam, L.; Turner, S. W.; Craighead, H. G.; Issacson, M.; Turner, J. N.; Shain, W., Preferential glial cell attachment to microcontact printed surfaces. *J Neurosci Meth* **1997,** *75* (2), 171-177.

[55] Olbrich, K. C.; Andersen, T. T.; Blumenstock, F. A.; Bizios, R., Surfaces modified with ovalently-immobilized adhesive peptides affect fibroblast population motility. *Biomaterials* **1996,** *17* (8), 759-764.

[56] Jans, K.; Van Meerbergen, B.; Reekmans, G.; Bonroy, K.; Annaert, W.; Maes, G.; Engelborghs, Y.; Borghs, G.; Bartic, C., Chemical and Biological Characterization of Thiol SAMs for Neuronal Cell Attachment. *Langmuir* **2009,** *25* (8), 4564-4570.

[57] Theodosis, D. T.; Bonhomme, R.; Vitiello, S.; Rougon, G.; Poulain, D. A., Cell surface expression of polysialic acid on NCAM is a prerequisite for activity-dependent morphological neuronal and glial plasticity. *J Neurosci* **1999,** *19* (23), 10228-10236.

[58] Muller, D.; Wang, C.; Skibo, G.; Toni, N.; Cremer, H.; Calaora, V.; Rougon, G.; Kiss, J. Z., PSA-NCAM is required for activity-induced synaptic plasticity. *Neuron* **1996,** *17* (3), 413-422.

[59] Acheson, A.; Sunshine, J. L.; Rutishauser, U., Ncam Polysialic Acid Can Regulate Both Cell Cell and Cell Substrate Interactions. *J Cell Biol* **1991,** *114* (1), 143-153.

[60] Kiss, J. Z.; Wang, C.; Olive, S.; Rougon, G.; Lang, J. C.; Baetens, D.; Harry, D.; Pralong, W. F., Activity-Dependent Mobilization of the Adhesion Molecule Polysialic Ncam to the Cell-Surface of Neurons and Endocrine-Cells. *Embo J* **1994,** *13* (22), 5284-5292.

[61] Tran, A. Q.; Kaulen, C.; Simon, U.; Offenhausser, A.; Mayer, D., Surface coupling strength of gold nanoparticles affects cytotoxicity towards neurons. *Biomater Sci-Uk* **2017,** *5* (5), 1051-1060.

[62] Gilles, S.; Kaulen, C.; Pabst, M.; Simon, U.; Offenhausser, A.; Mayer, D., Patterned self-assembly of gold nanoparticles on chemical templates fabricated by soft UV nanoimprint lithography. *Nanotechnology* **2011,** *22* (29).

[63] Yen, S. J.; Hsu, W. L.; Chen, Y. C.; Su, H. C.; Chang, Y. C.; Chen, H.; Yeh, S. R.; Yew, T. R., The enhancement of neural growth by amino-functionalization on carbon nanotubes as a neural electrode. *Biosens Bioelectron* **2011,** *26* (10), 4124-4132.

[64] Yavin, E.; Yavin, Z., Attachment and Culture of Dissociated Cells from Rat Embryo Cerebral Hemispheres on Polylysine-Coated Surface. *J Cell Biol* **1974,** *62* (2), 540-546.

[65] Sipe, J. D., Tissue engineering and reparative medicine. *Ann Ny Acad Sci* **2002,** *961*, 1-9.

[66] Griffith, L. G.; Naughton, G., Tissue engineering - Current challenges and expanding opportunities. *Science* **2002,** *295* (5557), 1009-+.

[67] Guilak, F.; Cohen, D. M.; Estes, B. T.; Gimble, J. M.; Liedtke, W.; Chen, C. S., Control of Stem Cell Fate by Physical Interactions with the Extracellular Matrix. *Cell Stem Cell* **2009,** *5* (1), 17-26.
[68] Berrier, A. L.; Yamada, K. M., Cell-matrix adhesion. *J Cell Physiol* **2007,** *213* (3), 565-573.
[69] Santoro, F.; Dasgupta, S.; Schnitker, J.; Auth, T.; Neumann, E.; Panaitov, G.; Gompper, G.; Offenhausser, A., Interfacing Electrogenic Cells with 3D Nanoelectrodes: Position, Shape, and Size Matter. *Acs Nano* **2014,** *8* (7), 6713-6723.
[70] Goldner, J. S.; Bruder, J. M.; Li, G.; Gazzola, D.; Hoffman-Kim, D., Neurite bridging across micropatterned grooves. *Biomaterials* **2006,** *27* (3), 460-472.
[71] Yang, K.; Jung, H.; Lee, H. R.; Lee, J. S.; Kim, S. R.; Song, K. Y.; Cheong, E.; Bang, J.; Im, S. G.; Cho, S. W., Multiscale, Hierarchically Patterned Topography for Directing Human Neural Stem Cells into Functional Neurons. *Acs Nano* **2014,** *8* (8), 7809-7822.
[72] Ventre, M.; Netti, P. A., Engineering Cell Instructive Materials To Control Cell Fate and Functions through Material Cues and Surface Patterning. *Acs Appl Mater Inter* **2016,** *8* (24), 14896-14908.
[73] Musah, S.; Wrighton, P. J.; Zaltsman, Y.; Zhong, X. F.; Zorn, S.; Parlato, M. B.; Hsiao, C.; Palecek, S. P.; Chang, Q.; Murphy, W. L.; Kiessling, L. L., Substratum-induced differentiation of human pluripotent stem cells reveals the coactivator YAP is a potent regulator of neuronal specification. *P Natl Acad Sci USA* **2014,** *111* (38), 13805-13810.
[74] Conde, C.; Caceres, A., Microtubule assembly, organization and dynamics in axons and dendrites. *Nat Rev Neurosci* **2009,** *10* (5), 319-332.
[75] Anselme, K.; Ploux, L.; Ponche, A., Cell/Material Interfaces: Influence of Surface Chemistry and Surface Topography on Cell Adhesion. *J Adhes Sci Technol* **2010,** *24* (5), 831-852.
[76] Naka, Y.; Eda, A.; Takei, H.; Shimizu, N., Neurite outgrowths of neurons on patterned self-assembled monolayers. *J Biosci Bioeng* **2002,** *94* (5), 434-439.
[77] Kleinfeld, D.; Kahler, K. H.; Hockberger, P. E., Controlled Outgrowth of Dissociated Neurons on Patterned Substrates. *J Neurosci* **1988,** *8* (11), 4098-4120.
[78] Liu, H. W.; Huang, W. C.; Chiang, C. S.; Hu, S. H.; Liao, C. H.; Chen, Y. Y.; Chen, S. Y., Arrayed rGOSH/PMASH Microcapsule Platform Integrating Surface Topography, Chemical Cues, and Electrical Stimulation for Three-Dimensional Neuron-Like Cell Growth and Neurite Sprouting. *Adv Funct Mater* **2014,** *24* (24), 3715-3724.
[79] Gomez, N.; Chen, S. C.; Schmidt, C. E., Polarization of hippocampal neurons with competitive surface stimuli: contact guidance cues are preferred over chemical ligands. *J R Soc Interface* **2007,** *4* (13), 223-233.
[80] Zhu, X. L.; Chen, J.; Scheideler, L.; Reichl, R.; Geis-Gerstorfer, J., Effects of topography and composition of titanium surface oxides on osteoblast responses. *Biomaterials* **2004,** *25* (18), 4087-4103.
[81] Brunette, D. M.; Chehroudi, B., The effects of the surface topography of micromachined titanium substrata on cell behavior in vitro and in vivo. *J Biomech Eng-T Asme* **1999,** *121* (1), 49-57.
[82] Lincks, J.; Boyan, B. D.; Cochran, D. L.; Liu, Y.; Blanchard, C.; Dean, D. D.; Schwartz, Z., Cell type and maturation state determine cell response to surface roughness and composition. *J Dent Res* **1998,** *77*, 966-966.

[83] Micholt, L.; Gartner, A.; Prodanov, D.; Braeken, D.; Dotti, C. G.; Bartic, C., Substrate Determines Neuronal Polarization and Growth In Vitro. *Plos One* **2013,** *8* (6).
[84] Hoffman-Kim, D.; Mitchel, J. A.; Bellamkonda, R. V., Topography, Cell Response, and Nerve Regeneration. *Annu Rev Biomed Eng* **2010,** *12*, 203-231.
[85] Engler, A. J.; Sen, S.; Sweeney, H. L.; Discher, D. E., Matrix elasticity directs stem cell lineage specification. *Cell* **2006,** *126* (4), 677-689.
[86] Moore, S. W.; Roca-Cusachs, P.; Sheetz, M. P., Stretchy Proteins on Stretchy Substrates: The Important Elements of Integrin-Mediated Rigidity Sensing. *Dev Cell* **2010,** *19* (2), 194-206.
[87] Zhang, Q. Y.; Zhang, Y. Y.; Xie, J.; Li, C. X.; Chen, W. Y.; Liu, B. L.; Wu, X. A.; Li, S. N.; Huo, B.; Jiang, L. H.; Zhao, H. C., Stiff substrates enhance cultured neuronal network activity. *Sci Rep-Uk* **2014,** *4*.
[88] Wolfram, T.; Spatz, J. P.; Burgess, R. W., Cell adhesion to agrin presented as a nanopatterned substrate is consistent with an interaction with the extracellular matrix and not transmembrane adhesion molecules. *Bmc Cell Biol* **2008,** *9*.
[89] Wolfram, T.; Belz, F.; Schoen, T.; Spatz, J. P., Site-specific presentation of single recombinant proteins in defined nanoarrays. *Biointerphases* **2007,** *2* (1), 44-48.
[90] Moller, K.; Meyer, U.; Szulczewski, D. H.; Heide, H.; Priessnitz, B.; Jones, D. B., The Influence of Zeta-Potential and Interfacial-Tension on Osteoblast-Like Cells. *Cell Mater* **1994,** *4* (3), 263-274.
[91] Senaratne, W.; Andruzzi, L.; Ober, C. K., Self-assembled monolayers and polymer brushes in biotechnology: Current applications and future perspectives. *Biomacromolecules* **2005,** *6* (5), 2427-2448.
[92] Andruzzi, L.; Senaratne, W.; Hexemer, A.; Sheets, E. D.; Ilic, B.; Kramer, E. J.; Baird, B.; Ober, C. K., Oligo(ethylene glycol) containing polymer brushes as bioselective surfaces. *Langmuir* **2005,** *21* (6), 2495-2504.
[93] Hamley, I. W., *Block Copolymers in Solution: Fundamentals and Applications*. 2005.
[94] Kästle G. et al, *Micellar Nanoreactors—Preparation and Characterization of Hexagonally Ordered Arrays of Metallic Nanodots Advanced Functional Materials* **2003,** *13* (11), p.853-861.
[95] Tran, A. Q. DNA duplex stability studies using ordered arrays of nanoparticles as sensor platforms. uHasselt, 2012.
[96] Boyen, H. G.; Kastle, G.; Zurn, K.; Herzog, T.; Weigl, F.; Ziemann, P.; Mayer, O.; Jerome, C.; Moller, M.; Spatz, J. P.; Garnier, M. G.; Oelhafen, P., A micellar route to ordered arrays of magnetic nanoparticles: From size-selected pure cobalt dots to cobalt-cobalt oxide core-shell systems. *Adv Funct Mater* **2003,** *13* (5), 359-364.
[97] Lawson, D. M.; Artymiuk, P. J.; Yewdall, S. J.; Smith, J. M. A.; Livingstone, J. C.; Treffry, A.; Luzzago, A.; Levi, S.; Arosio, P.; Cesareni, G.; Thomas, C. D.; Shaw, W. V.; Harrison, P. M., Solving the Structure of Human H-Ferritin by Genetically Engineering Intermolecular Crystal Contacts. *Nature* **1991,** *349* (6309), 541-544.
[98] Macedo, S.; Romao, C. V.; Mitchell, E.; Matias, P. M.; Liu, M. Y.; Xavier, A. V.; LeGall, J.; Teixeira, M.; Lindley, P.; Carrondo, M. A., The nature of the di-iron site in the bacterioferritin from Desulfovibrio desulfuricans. *Nat Struct Biol* **2003,** *10* (4), 285-290.
[99] He, D. D.; Marles-Wright, J., Ferritin family proteins and their use in bionanotechnology. *New Biotechnol* **2015,** *32* (6), 651-657.

[100] Thiery, G.; Bernier, J.; Bergeron, M., A Simple Technique for Staining of Cell-Membranes with Imidazole and Osmium-Tetroxide. *J Histochem Cytochem* **1995,** *43* (10), 1079-1084.
[101] Belu A, S. J., Bertazzo S., Neumann E., Mayer D., Offenhäusser A., Santoro F., Ultra-thin resin embedding method for scanning electron microscopy of individual cells on high and low aspect ratio 3D nanostructures. *J Microsc.* **2016**.
[102] MT-MTD *Hooke's law*. http://www.ntmdt.com/spm-basics/view/hooke-law.
[103] Rebecca Howland et al, *A practical guide to scanning probe micriscopy*. 2000.
[104] John F Watts and John Wolstenholme, *An introduction to surface analysis by XPS and AES*. Wiley: 2003.
[105] Tran, A. Q. Nanostructures for biosensing: DNA duplex stability studies using ordered arrays of nanoparticles as sensor platforms. Hasselt University, Hasselt University, 2012.
[106] Greben, K.; Li, P. G.; Mayer, D.; Offenhausser, A.; Wordenweber, R., Immobilization and Surface Functionalization of Gold Nanoparticles Monitored via Streaming Current/Potential Measurements. *J Phys Chem B* **2015,** *119* (19), 5988-5994.
[107] Brewer, G. J.; Torricelli, J. R.; Evege, E. K.; Price, P. J., Optimized Survival of Hippocampal-Neurons in B27-Supplemented Neurobasal(Tm), a New Serum-Free Medium Combination. *J Neurosci Res* **1993,** *35* (5), 567-576.
[108] Fricke, R.; Zentis, P. D.; Rajappa, L. T.; Hofmann, B.; Banzet, M.; Offenhausser, A.; Meffert, S. H., Axon guidance of rat cortical neurons by microcontact printed gradients. *Biomaterials* **2011,** *32* (8), 2070-2076.
[109] Seyock, S.; Maybeck, V.; Scorsone, E.; Rousseau, L.; Hebert, C.; Lissorgues, G.; Bergonzo, P.; Offenhausser, A., Interfacing neurons on carbon nanotubes covered with diamond. *Rsc Adv* **2017,** *7* (1), 153-160.
[110] Kundu, P.; Belu, A.; Neumann, E.; Mayer, D.; Offenhausser, A., 3D Au-SiO2 nanohybrids as a potential scaffold coating material for neuroengineering. *Rsc Adv* **2016,** *6* (53), 47948-47952.
[111] Kaulen, C.; Homberger, M.; Bourone, S.; Babajani, N.; Karthauser, S.; Besmehn, A.; Simon, U., Differential Adsorption of Gold Nanoparticles to Gold/Palladium and Platinum Surfaces. *Langmuir* **2014,** *30* (2), 574-583.
[112] Nath, N.; Chilkoti, A., Label-free biosensing by surface plasmon resonance of nanoparticles on glass: Optimization of nanoparticle size. *Anal Chem* **2004,** *76* (18), 5370-5378.
[113] von der Mark, K.; Park, J.; Bauer, S.; Schmuki, P., Nanoscale engineering of biomimetic surfaces: cues from the extracellular matrix. *Cell Tissue Res* **2010,** *339* (1), 131-153.
[114] Skirtach, A. G.; Volodkin, D. V.; Mohwald, H., Bio-interfaces-Interaction of PLL/HA Thick Films with Nanoparticles and Microcapsules. *Chemphyschem* **2010,** *11* (4), 822-829.
[115] Alves, N. M.; Pashkuleva, I.; Reis, R. L.; Mano, J. F., Controlling Cell Behavior Through the Design of Polymer Surfaces. *Small* **2010,** *6* (20), 2208-2220.
[116] Dubiel, E. A.; Martin, Y.; Vermette, P., Bridging the Gap Between Physicochemistry and Interpretation Prevalent in Cell-Surface Interactions. *Chem Rev* **2011,** *111* (4), 2900-2936.
[117] Necas D. and P. Klapetek *Gwyddion*. http://gwyddion.net/.

[118] Brucker The nanoscale World-Bruker. http://nanoscaleworld.bruker-axs.com/nanoscaleworld/.
[119] Pichler, S.; Bodnarchuk, M. I.; Kovalenko, M. V.; Yarema, M.; Springholz, G.; Talapin, D. V.; Heiss, W., Evaluation of Ordering in Single-Component and Binary Nanocrystal Superlattices by Analysis of Their Autocorrelation Functions. *Acs Nano* **2011,** *5* (3), 1703-1712.
[120] Wu, C. K.; Hultman, K. L.; O'Brien, S.; Koberstein, J. T., Functional oligomers for the control and fixation of spatial organization in nanoparticle assemblies. *J Am Chem Soc* **2008,** *130* (11), 3516-3520.
[121] Williams, S. E.; Davies, P. R.; Bowen, J. L.; Allender, C. J., Controlling the Nanoscale Patterning of AuNPs on Silicon Surfaces. *Nanomaterials-Basel* **2013,** *3* (1), 192-203.
[122] Morel, A. L.; Boujday, S.; Methivier, C.; Krafft, J. M.; Pradier, C. M., Biosensors elaborated on gold nanoparticles, a PM-IRRAS characterisation of the IgG binding efficiency. *Talanta* **2011,** *85* (1), 35-42.
[123] Zhong, Z. Y.; Patskovskyy, S.; Bouvrette, P.; Luong, J. H. T.; Gedanken, A., The surface chemistry of Au colloids and their interactions with functional amino acids. *J Phys Chem B* **2004,** *108* (13), 4046-4052.
[124] Kooij, E. S.; Brouwer, E. A. M.; Wormeester, H.; Poelsema, B., Ionic strength mediated self-organization of gold nanocrystals: An AFM study. *Langmuir* **2002,** *18* (20), 7677-7682.
[125] Derjaguin, B.; Landau, L., Theory of the Stability of Strongly Charged Lyophobic Sols and of the Adhesion of Strongly Charged-Particles in Solutions of Electrolytes. *Prog Surf Sci* **1993,** *43* (1-4), 30-59.
[126] Verwey, E. J. W., Theory of the Stability of Lyophobic Colloids. *J Phys Colloid Chem* **1947,** *51* (3), 631-636.
[127] Llorca, J.; Casanovas, A.; Dominguez, M.; Casanova, I.; Angurell, I.; Seco, M.; Rossell, O., Plasma-activated core-shell gold nanoparticle films with enhanced catalytic properties. *J Nanopart Res* **2008,** *10* (3), 537-542.
[128] Xu, H. Y.; Luo, J. J.; Chu, W., Non-thermal plasma-treated gold catalyst for CO oxidation. *Rsc Adv* **2014,** *4* (49), 25729-25735.
[129] Wu, J. C.; Shi, W. W.; Chopra, N., Plasma Oxidation Kinetics of Gold Nanoparticles and Their Encapsulation in Graphene Shells by Chemical Vapor Deposition Growth. *J Phys Chem C* **2012,** *116* (23), 12861-12874.
[130] Darwich, S.; Mougin, K.; Rao, A.; Gnecco, E.; Jayaraman, S.; Haidara, H., Manipulation of gold colloidal nanoparticles with atomic force microscopy in dynamic mode: influence of particle-substrate chemistry and morphology, and of operating conditions. *Beilstein J Nanotech* **2011,** *2*, 85-98.
[131] Eppler, A. S.; Rupprechter, G.; Anderson, E. A.; Somorjai, G. A., Thermal and chemical stability and adhesion strength of Pt nanoparticle arrays supported on silica studied by transmission electron microscopy and atomic force microscopy. *J Phys Chem B* **2000,** *104* (31), 7286-7292.
[132] Raiber, K.; Terfort, A.; Benndorf, C.; Krings, N.; Strehblow, H. H., Removal of self-assembled monolayers of alkanethiolates on gold by plasma cleaning. *Surf Sci* **2005,** *595* (1-3), 56-63.
[133] Koslowski, B.; Boyen, H. G.; Wilderotter, C.; Kastle, G.; Ziemann, P.; Wahrenberg, R.; Oelhafen, P., Oxidation of preferentially (111)-oriented Au films in an

oxygen plasma investigated by scanning tunneling microscopy and photoelectron spectroscopy. *Surf Sci* **2001,** *475* (1-3), 1-10.
[134] Delivopoulos, E.; Ouberai, M. M.; Coffey, P. D.; Swann, M. J.; Shakesheff, K. M.; Welland, M. E., Serum protein layers on parylene-C and silicon oxide: Effect on cell adhesion. *Colloid Surface B* **2015,** *126*, 169-177.
[135] Gentile, F.; La Rocca, R.; Marinaro, G.; Nicastri, A.; Toma, A.; Paonessa, F.; Cojoc, G.; Liberale, C.; Benfenati, F.; di Fabrizio, E.; Decuzzi, P., Differential Cell Adhesion on Mesoporous Silicon Substrates. *Acs Appl Mater Inter* **2012,** *4* (6), 2903-2911.
[136] Yang, C. Y.; Huang, L. Y.; Shen, T. L.; Yeh, J. A., Cell Adhesion, Morphology and Biochemistry on Nano-Topographic Oxidized Silicon Surfaces. *Eur Cells Mater* **2010,** *20*, 415-430.
[137] Thelen, K.; Wolfram, T.; Maier, B.; Jahrling, S.; Tinazli, A.; Piehler, J.; Spatz, J. P.; Pollerberg, G. E., Cell adhesion molecule DM-GRASP presented as nanopatterns to neurons regulates attachment and neurite growth. *Soft Matter* **2007,** *3* (12), 1486-1491.
[138] Scholl, M.; Sprossler, C.; Denyer, M.; Krause, M.; Nakajima, K.; Maelicke, A.; Knoll, W.; Offenhausser, A., Ordered networks of rat hippocampal neurons attached to silicon oxide surfaces. *J Neurosci Meth* **2000,** *104* (1), 65-75.
[139] Hinterwirth, H.; Kappel, S.; Waitz, T.; Prohaska, T.; Lindner, W.; Lammerhofer, M., Quantifying Thiol Ligand Density of Self-Assembled Monolayers on Gold Nanoparticles by Inductively Coupled Plasma-Mass Spectrometry. *Acs Nano* **2013,** *7* (2), 1129-1136.
[140] Dadsetan, M.; Knight, A. M.; Lu, L. C.; Windebank, A. J.; Yaszemski, M. J., Stimulation of neurite outgrowth using positively charged hydrogels. *Biomaterials* **2009,** *30* (23-24), 3874-3881.
[141] Makohliso, S. A.; Valentini, R. F.; Aebischer, P., Magnitude and Polarity of a Fluoroethylene Propylene Electret Substrate Charge Influences Neurite Outgrowth in-Vitro. *J Biomed Mater Res* **1993,** *27* (8), 1075-1085.
[142] Gomez, T. M.; Spitzer, N. C., Regulation of growth cone behavior by calcium: new dynamics to earlier perspectives. *J Neurobiol* **2000,** *44* (2), 174-183.
[143] Kater, S. B.; Mills, L. R., Regulation of Growth Cone Behavior by Calcium. *J Neurosci* **1991,** *11* (4), 891-899.
[144] Ishibashi, Y.; Uesugi, K.; Morishima, K., Effect of Mechanical Stimulation on Neurite Outgrowth of Dorsal Root Ganglion Neurons Toward Integrative Mechanobiologic Nerve Bridge. *Ieee/Sice I S Sys In* **2016**, 797-802.
[145] Loverde, J. R.; Tolentino, R. E.; Pfister, B. J., Axon Stretch Growth: The Mechanotransduction of Neuronal Growth. *Jove-J Vis Exp* **2011,** (54).
[146] Boda, S. K.; Broda, J.; Schiefer, F.; Weber-Heynemann, J.; Hoss, M.; Simon, U.; Basu, B.; Jahnen-Dechent, W., Cytotoxicity of Ultrasmall Gold Nanoparticles on Planktonic and Biofilm Encapsulated Gram-Positive Staphylococci. *Small* **2015,** *11* (26), 3183-3193.
[147] Pan, Y.; Neuss, S.; Leifert, A.; Fischler, M.; Wen, F.; Simon, U.; Schmid, G.; Brandau, W.; Jahnen-Dechent, W., Size-dependent cytotoxicity of gold nanoparticles. *Small* **2007,** *3* (11), 1941-1949.
[148] Shang, L.; Nienhaus, K.; Jiang, X. U.; Yang, L. X.; Landfester, K.; Mailaander, V.; Simmet, T.; Nienhaus, G. U., Nanoparticle interactions with live cells: Quantitative

fluorescence microscopy of nanoparticle size effects. *Beilstein J Nanotech* **2014,** *5*, 2388-2397.
[149] Zhao, X. X.; Ng, S.; Heng, B. C.; Guo, J.; Ma, L.; Tan, T. T. Y.; Ng, K. W.; Loo, S. C. J., Cytotoxicity of hydroxyapatite nanoparticles is shape and cell dependent. *Arch Toxicol* **2013,** *87* (6), 1037-1052.
[150] Zhang, Y. A.; Xu, D.; Li, W. Q.; Yu, J.; Chen, Y., Effect of Size, Shape, and Surface Modification on Cytotoxicity of Gold Nanoparticles to Human HEp-2 and Canine MDCK Cells. *J Nanomater* **2012,** *7* (7), 375496.
[151] Rivet, C. J.; Yuan, Y.; Borca-Tasciuc, D. A.; Gilbert, R. J., Altering Iron Oxide Nanoparticle Surface Properties Induce Cortical Neuron Cytotoxicity. *Chem Res Toxicol* **2012,** *25* (1), 153-161.
[152] Sohaebuddin, S. K.; Thevenot, P. T.; Baker, D.; Eaton, J. W.; Tang, L. P., Nanomaterial cytotoxicity is composition, size, and cell type dependent. *Part Fibre Toxicol* **2010,** *7*.
[153] Kim, S. T.; Saha, K.; Kim, C.; Rotello, V. M., The Role of Surface Functionality in Determining Nanoparticle Cytotoxicity. *Accounts Chem Res* **2013,** *46* (3), 681-691.
[154] Goodman, C. M.; McCusker, C. D.; Yilmaz, T.; Rotello, V. M., Toxicity of gold nanoparticles functionalized with cationic and anionic side chains. *Bioconjugate Chem* **2004,** *15* (4), 897-900.
[155] Kim, M. H.; Park, M.; Kang, K.; Choi, I. S., Neurons on nanometric topographies: insights into neuronal behaviors in vitro. *Biomater Sci-Uk* **2014,** *2* (2), 148-155.
[156] Soenen, S. J.; Manshian, B.; Montenegro, J. M.; Amin, F.; Meermann, B.; Thiron, T.; Cornelissen, M.; Vanhaecke, F.; Doak, S.; Parak, W. J.; De Smedt, S.; Braeckmans, K., Cytotoxic Effects of Gold Nanoparticles: A Multiparametric Study. *Acs Nano* **2012,** *6* (7), 5767-5783.
[157] Broda, J.; Setzler, J.; Leifert, A.; Steitz, J.; Benz, R.; Simon, U.; Wenzel, W., Ligand-lipid and ligand-core affinity control the interaction of gold nanoparticles with artificial lipid bilayers and cell membranes. *Nanomed-Nanotechnol* **2016,** *12* (5), 1409-1419.
[158] Mislick, K. A.; Baldeschwieler, J. D., Evidence for the role of proteoglycans in cation-mediated gene transfer. *P Natl Acad Sci USA* **1996,** *93* (22), 12349-12354.
[159] Yang, C.; Uertz, J.; Yohan, D.; Chithrani, B. D., Peptide modified gold nanoparticles for improved cellular uptake, nuclear transport, and intracellular retention. *Nanoscale* **2014,** *6* (20), 12026-12033.
[160] Astolfo, A.; Arfelli, F.; Schultke, E.; James, S.; Mancini, L.; Menk, R. H., A detailed study of gold-nanoparticle loaded cells using X-ray based techniques for cell-tracking applications with single-cell sensitivity. *Nanoscale* **2013,** *5* (8), 3337-3345.
[161] Trono, J. D.; Mizuno, K.; Yusa, N.; Matsukawa, T.; Yokoyama, K.; Uesaka, M., Size, Concentration and Incubation Time Dependence of Gold Nanoparticle Uptake into Pancreas Cancer Cells and its Future Application to X-ray Drug Delivery System. *J Radiat Res* **2011,** *52* (1), 103-109.
[162] Chithrani, B. D.; Ghazani, A. A.; Chan, W. C. W., Determining the size and shape dependence of gold nanoparticle uptake into mammalian cells. *Nano Lett* **2006,** *6* (4), 662-668.
[163] Seyock, S.; Maybeck, V.; Offenhausser, A., How to image cell adhesion on soft polymers? *Micron* **2017,** *92*, 39-42.

[164] Sun, T. M.; Zhang, Y. S.; Pang, B.; Hyun, D. C.; Yang, M. X.; Xia, Y. N., Engineered Nanoparticles for Drug Delivery in Cancer Therapy. *Angew Chem Int Edit* **2014,** *53* (46), 12320-12364.
[165] Kuo, C. W.; Chen, P. L., The Applications of Metallic Nanowires for Live Cell Studies. *Electrodeposited Nanowires and Their Applications* **2010**, 213-228.
[166] Kuo, C. W.; Shiu, J. Y.; Wei, K. H.; Chen, P. L., Functionalized silver nanowires for live cell study. *Chem Lett* **2008,** *37* (6), 610-611.
[167] Schulte, C.; Ripamonti, M.; Maffioli, E.; Cappelluti, M. A.; Nonnis, S.; Puricelli, L.; Lamanna, J.; Piazzoni, C.; Podesta, A.; Lenardi, C.; Tedeschi, G.; Malgaroli, A.; Milani, P., Scale Invariant Disordered Nanotopography Promotes Hippocampal Neuron Development and Maturation with Involvement of Mechanotransductive Pathways. *Front Cell Neurosci* **2016,** *10*.
[168] Frandsen, C. J.; Noh, K.; Brammer, K. S.; Johnston, G.; Jin, S. H., Hybrid micro/nano-topography of a TiO2 nanotube-coated commercial zirconia femoral knee implant promotes bone cell adhesion in vitro. *Mat Sci Eng C-Mater* **2013,** *33* (5), 2752-2756.
[169] Kaibuchi, K., Neuronal polarity: From extracellular signals to intracellular mechanisms. *Neurosci Res* **2009,** *65*, S2-S2.
[170] Wilhelm, C.; Gazeau, F.; Roger, J.; Pons, J. N.; Bacri, J. C., Interaction of anionic superparamagnetic nanoparticles with cells: Kinetic analyses of membrane adsorption and subsequent internalization. *Langmuir* **2002,** *18* (21), 8148-8155.
[171] Felder, S.; Lavin, J.; Ullrich, A.; Schlessinger, J., Kinetics of Binding, Endocytosis, and Recycling of Egf Receptor Mutants. *J Cell Biol* **1992,** *117* (1), 203-212.
[172] Caruso, F.; Hyeon, T.; Rotello, V. M., Nanomedicine. *Chem Soc Rev* **2012,** *41* (7), 2537-2538.
[173] Cho, E. C.; Zhang, Q.; Xia, Y. N., The effect of sedimentation and diffusion on cellular uptake of gold nanoparticles. *Nat Nanotechnol* **2011,** *6* (6), 385-391.
[174] Meyer, S.; Song, C. M.; Jin, Y. L.; Wang, K.; Makse, H. A., Jamming in two-dimensional packings. *Physica A* **2010,** *389* (22), 5137-5144.
[175] Cho, E. C.; Xie, J. W.; Wurm, P. A.; Xia, Y. N., Understanding the Role of Surface Charges in Cellular Adsorption versus Internalization by Selectively Removing Gold Nanoparticles on the Cell Surface with a I-2/KI Etchant. *Nano Lett* **2009,** *9* (3), 1080-1084.
[176] Bischofs, I. B.; Schmidt, S. S.; Schwarz, U. S., Effect of Adhesion Geometry and Rigidity on Cellular Force Distributions. *Phys Rev Lett* **2009,** *103* (4).
[177] Conner, S. D.; Schmid, S. L., Regulated portals of entry into the cell. *Nature* **2003,** *422* (6927), 37-44.
[178] Apodaca, G., Endocytic traffic in polarized epithelial cells: Role of the actin and microtubule cytoskeleton. *Traffic* **2001,** *2* (3), 149-159.
[179] Teo, B. K. K.; Wong, S. T.; Lim, C. K.; Kung, T. Y. S.; Yap, C. H.; Ramagopal, Y.; Romer, L. H.; Yim, E. K. F., Nanotopography Modulates Mechanotransduction of Stem Cells and Induces Differentiation through Focal Adhesion Kinase. *Acs Nano* **2013,** *7* (6), 4785-4798.
[180] Trichet, L.; Le Digabel, J.; Hawkins, R. J.; Vedula, R. K.; Gupta, M.; Ribrault, C.; Hersen, P.; Voituriez, R.; Ladoux, B., Evidence of a large-scale mechanosensing mechanism for cellular adaptation to substrate stiffness. *P Natl Acad Sci USA* **2012,** *109* (18), 6933-6938.

[181] Biggs, M. J. P.; Richards, R. G.; Dalby, M. J., Nanotopographical modification: a regulator of cellular function through focal adhesions. *Nanomed-Nanotechnol* **2010,** *6* (5), 619-633.
[182] Biggs, M. J. P.; Richards, R. G.; Gadegaard, N.; Wilkinson, C. D. W.; Oreffo, R. O. C.; Dalby, M. J., The use of nanoscale topography to modulate the dynamics of adhesion formation in primary osteoblasts and ERK/MAPK signalling in STRO-1+enriched skeletal stem cells. *Biomaterials* **2009,** *30* (28), 5094-5103.
[183] Koser, D. E.; Thompson, A. J.; Foster, S. K.; Dwivedy, A.; Pillai, E. K.; Sheridan, G. K.; Svoboda, H.; Viana, M.; Costa, L. D.; Guck, J.; Holt, C. E.; Franze, K., Mechanosensing is critical for axon growth in the developing brain. *Nat Neurosci* **2016,** *19* (12), 1592-1598.
[184] Dent, E. W.; Gupton, S. L.; Gertler, F. B., The Growth Cone Cytoskeleton in Axon Outgrowth and Guidance. *Csh Perspect Biol* **2011,** *3* (3).
[185] Medeiros, N. A.; Burnette, D. T.; Forscher, P., Myosin II functions in actin-bundle turnover in neuronal growth cones. *Nat Cell Biol* **2006,** *8* (3), 215-226.
[186] Nichol, R. H.; Hagen, K. M.; Lumbard, D. C.; Dent, E. W.; Gomez, T. M., Guidance of Axons by Local Coupling of Retrograde Flow to Point Contact Adhesions. *J Neurosci* **2016,** *36* (7), 2267-2282.
[187] Myers, J. P.; Gomez, T. M., Focal Adhesion Kinase Promotes Integrin Adhesion Dynamics Necessary for Chemotropic Turning of Nerve Growth Cones. *J Neurosci* **2011,** *31* (38), 13585-13595.
[188] Condic, M. L.; Letourneau, P. C., Ligand-induced changes in integrin expression regulate neuronal adhesion and neurite outgrowth. *Nature* **1997,** *389* (6653), 852-856.
[189] Ren, Y.; Suter, D. M., Increase in Growth Cone Size Correlates with Decrease in Neurite Growth Rate. *Neural Plast* **2016**.
[190] Lin, C. H.; Forscher, P., Growth Cone Advance Is Inversely Proportional to Retrograde F-Actin Flow. *Neuron* **1995,** *14* (4), 763-771.
[191] Lee, K. Y.; Alsberg, E.; Hsiong, S.; Comisar, W.; Linderman, J.; Ziff, R.; Mooney, D., Nanoscale adhesion ligand organization regulates osteoblast proliferation and differentiation. *Nano Lett* **2004,** *4* (8), 1501-1506.
[192] Poole, K.; Khairy, K.; Friedrichs, J.; Franz, C.; Cisneros, D. A.; Howard, J.; Mueller, D., Molecular-scale topographic cues induce the orientation and directional movement of fibroblasts on two-dimensional collagen surfaces. *J Mol Biol* **2005,** *349* (2), 380-386.
[193] Rutishauser, U.; Watanabe, M.; Silver, J.; Troy, F. A.; Vimr, E. R., Specific Alteration of Ncam-Mediated Cell-Adhesion by an Endoneuraminidase. *J Cell Biol* **1985,** *101* (5), 1842-1849.
[194] Finne, J.; Makela, P. H., Cleavage of the Polysialosyl Units of Brain Glycoproteins by a Bacteriophage Endosialidase - Involvement of a Long Oligosaccharide Segment in Molecular-Interactions of Polysialic Acid. *J Biol Chem* **1985,** *260* (2), 1265-1270.
[195] Blau, A., Cell adhesion promotion strategies for signal transduction enhancement in microelectrode array in vitro electrophysiology: An introductory overview and critical discussion. *Curr Opin Colloid In* **2013,** *18* (5), 481-492.
[196] Schwaab, D.; Zentis, P.; Winter, S.; Meffert, S.; Offenhausser, A.; Mayer, D., Generation of Protein Nanogradients by Microcontact Printing. *Jpn J Appl Phys* **2013,** *52* (5).

APPENDIX A: ABBREVIATIONS

AC: Adhesion complex

APTES: 3-aminopropyltriethoxysilane

AUT: 11-amino-1-undecanethiol

AUT-AuNPs: amino functionalized gold nanoparticles

AFM: atomic force microscopy

Cit-AuNPs: citrate stabilized gold nanoparticles

DIV: days in vitro

Endo-N: endoneuraminidase

EtOH: Ethanol

FOTCS: trichloro(1H,1H,2H,2H-perflueooctyl) silane

FIB: focused ion beam

FerNPs: ferritin nanoparticles

MAP2: microtubule-associated protein 2

MW: molecular weight

MM: molecular mass

NP: nanoparticle

NCAM: neuronal cell adhesion molecule

PEG: 2-[methoxy(polyethylenoxy)6-9propyl] trichlorosilane

SEM: scanning electron microscopy

WB: weakly bound

RF: retrograde flow

SB: strongly bound

PSA: poliasilic acid

PDL: Poly-d-lysine

PDMS: poly(dimethysiloxane)

P2VP: poly(2-vinylpyridine)

PS: polystyrine

XPS: X-ray photoemission sprectroscopy

APPENDIX B: FIGURES AND TABLES

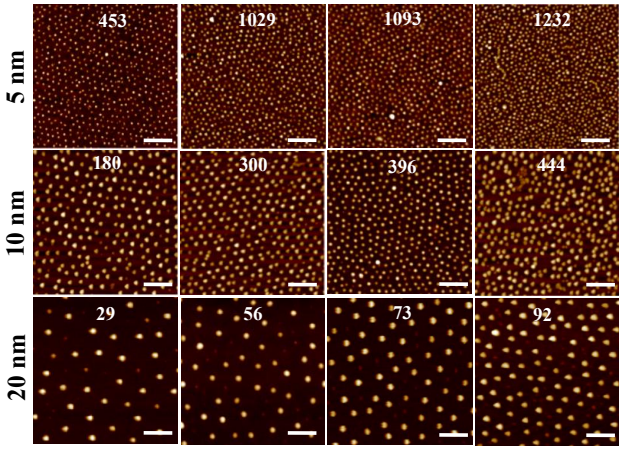

Figure A4.1 AFM images of ordered AuNPs with different sizes and densities, particles densities (per μm^2) are shown in each image. Scale bar: 100 nm.

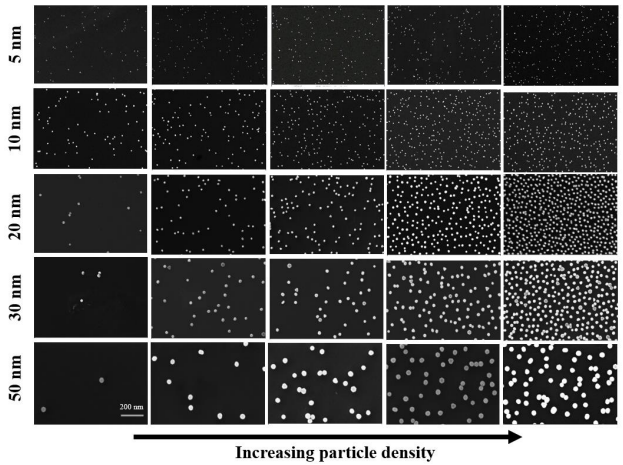

Figure A4.2 Live (green) and dead (red) fluorescence staining of DIV3 neurons on AUT-modified AuNPs of different sizes and densities with PEG backfill passivation. The particles are weakly bound to the substrate (WB particles). The particles densities (per μm^2) are shown in each image. Scale bar: 200 nm.

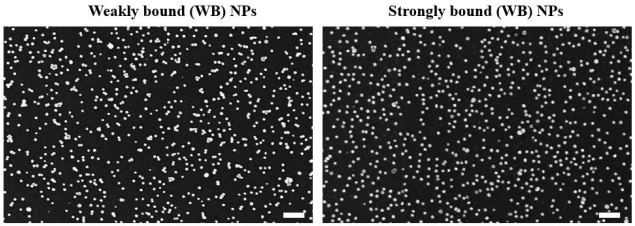

Figure A4.3 SEM images of 20 nm NPs after chemical modifications after applying an additional 1 min sonication treatment to illustrate the difference in particle binding strength. The left image shows weakly bound (WB) particles, which strongly aggregate during sonication (at least 8.6% particle aggregated), while the strongly bound (SB) particles remain separated (about 1.7% particles aggregated) after this treatment, right image. Noteworthy, during standard sample preparation for cell culture experiments, sonication was not used. Scale bar: 200 nm.

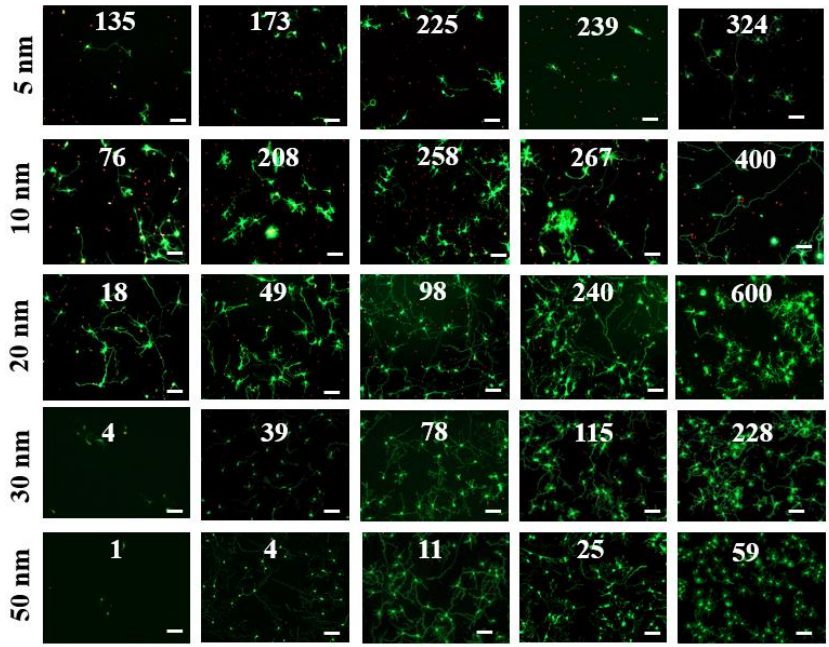

Figure A4.4 Live (green) and dead (red) fluorescence staining of DIV3 neurons on AUT-modified AuNPs of different sizes and densities with PEG backfill passivation. The particles are weakly bound to the substrate (WB particles). The particles densities (per μm^2) are shown in each image. Scale bar: 100 µm.

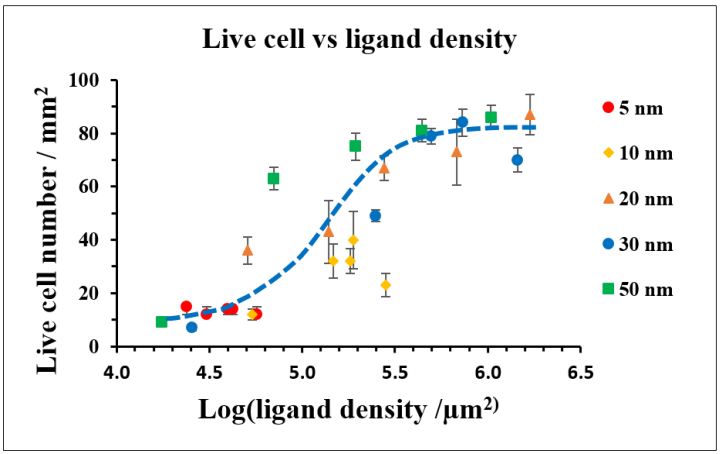

Figure A4.5 Dependence of live cell number on the particle size and density corresponding to a sigmoidal dose-response curve (dash grey curve), the graph is repotted from Figure 4.10C with a logarithm of ligand density (X-axis).

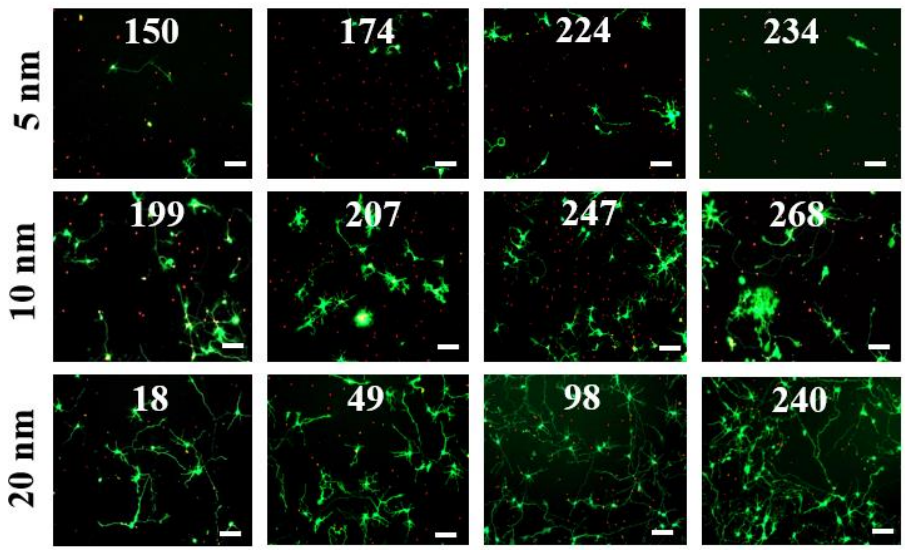

Figure A4.6 Live (green) and dead (red) fluorescence staining of DIV3 neurons on AUT-modified AuNPs of different sizes and densities with PEG backfill passivation. The particles are weakly bound to the substrate (WB particles). The particles densities (per μm^2) are shown in each image. Scale bar: 100 µm.

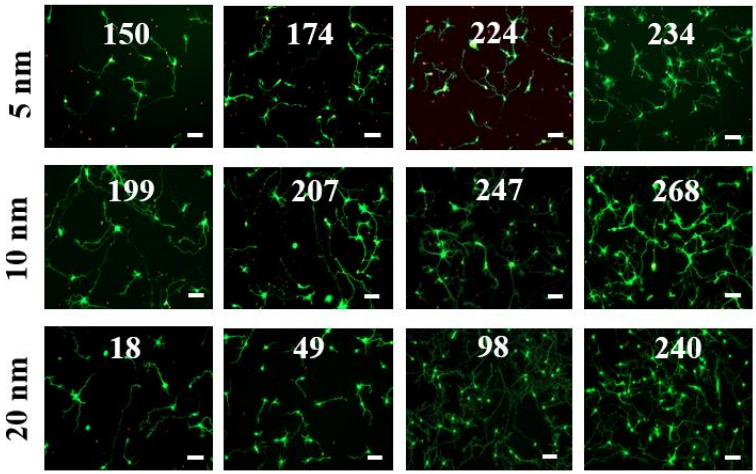

Figure A4.7 Live (green) and dead (red) fluorescence images of the DIV3 neurons on AUT-modified AuNPs of different sizes and densities with PEG backfill passivation. The particles are strongly bound to the substrate (SB particles). The particles densities (per μm^2) are shown in each image. Scale bar: 100 µm

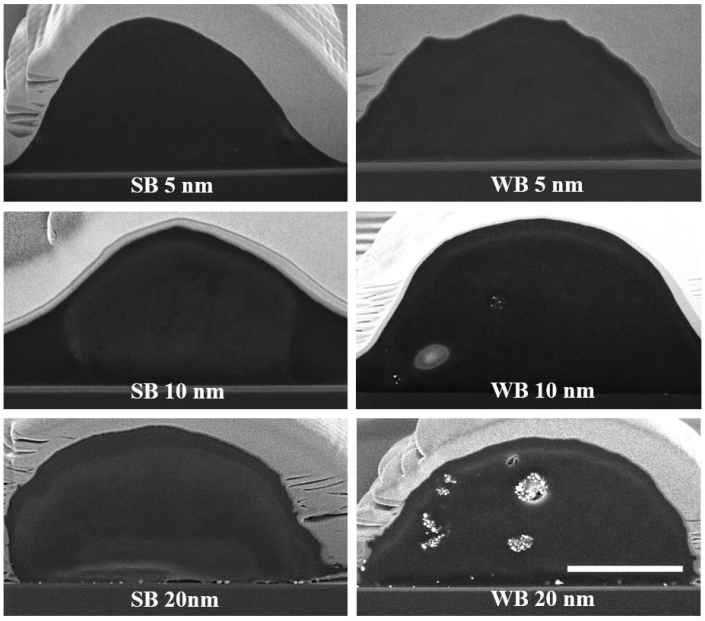

Figure A4.8 FIB cuts images of cells cultured on the 5 nm, 10 nm, and 20 nm particles for SB and WB. Scale bar: 2 µm.

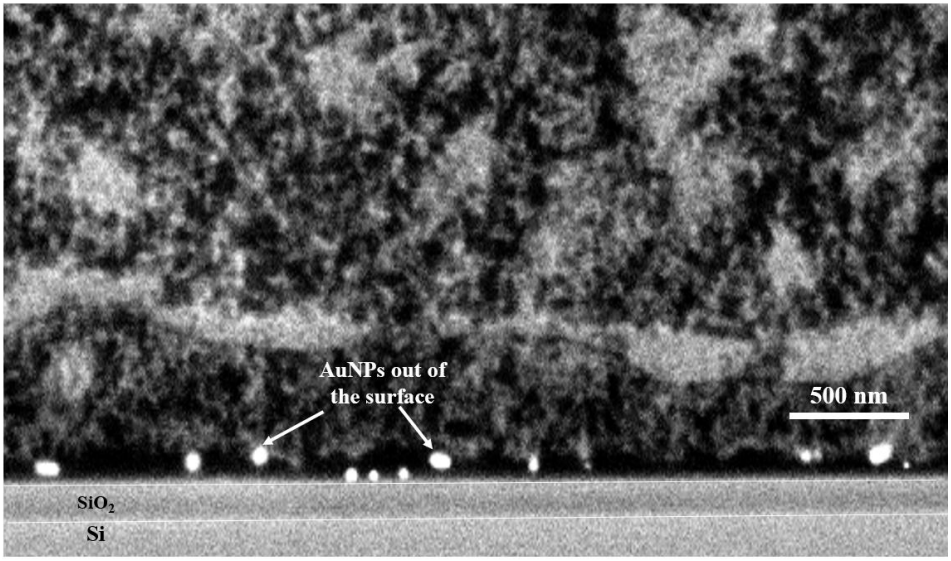

Figure A4.9 A FIB cross-section of a neuron on WB 20nm AuNP indicates the particles could be lift off from the substrates with the cell membrane

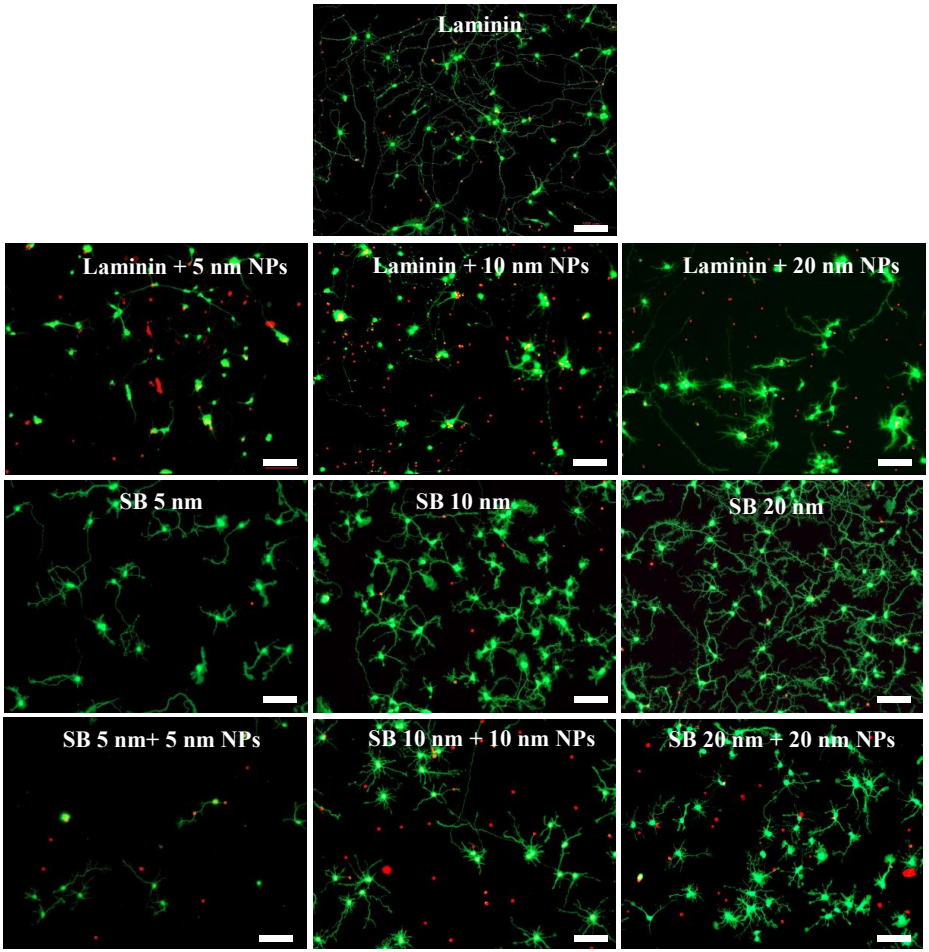

Figure A4.10 Live (green) and dead (red) fluorescence images of the DIV3 neurons on laminin coated SiO_2 (control), and SB NP samples (with and without added dispersed NPs). Laminin is used as coating for the reference sample to eliminate animal to animal variations and influences from varying culture conditions. It has been widely used as coating for in vitro studies of cortical cells. Scale bar: 100 μm.

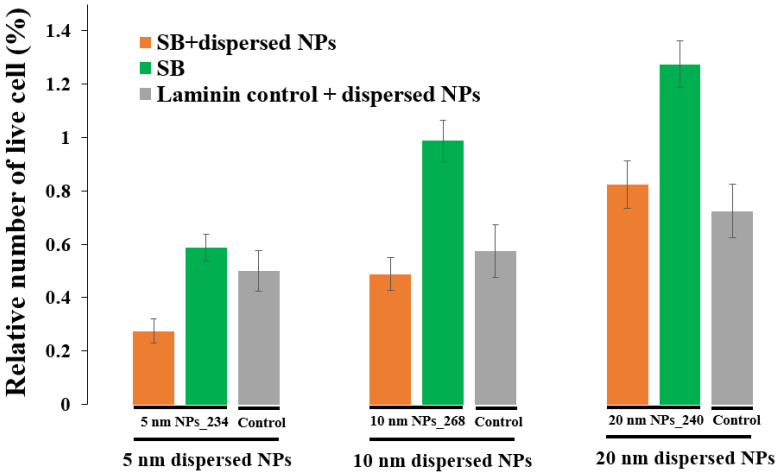

Figure A4.11 The statistical analysis of the relative live cell number on SB particles (with and without adding dispersed AuNP) and laminin coated SiO_2 samples (with added the nanoparticles). The relative number of live cells are calculated by dividing the live cell number of each sample by the live cell number of laminin coated SiO_2 sample (particle-free). The density of each particle size is given per μm^2 for 5 nm, 10 nm, and 20 nm as 234, 268, and 240 respectively. (The cell cultures were repeated at least three times, N=6; and variation shown by standard error, SE).

Size [nm]	Amount(1) [mg/l]	Density of as-prepared particles [μl^{-1}]	Particle density in culture medium [ml^{-1}]	Density of surface tethered AuNP in contact with cells(2) [cm^{-2}]
5	5966	4.7×10^{12}	4.7×10^{12}	1.05×10^{9}
10	1536	1.5×10^{11}	5.1×10^{11}	2.28×10^{9}
20	152	1.9×10^{9}	2.5×10^{10}	3.6×10^{9}

Table A4.1 The concentration of AUT-modified-AuNPs of 5 nm, 10 nm, and 20 nm sizes, the number of particles (per µL) is calculated from the amount of gold(1) measured from the atomic absorption spectroscopy (AAS) (2) The particles in contact with cells are calculated from the surface coverage of cells on SB AuNPs

Table A4.2: Characterization of AUT-AuNP.

Size [nm]	λ_{max} (UV-vis) [nm]	z-average (DLS) [nm]
5	532	85 ± 2
10	532	129 ± 5
20	530	90 ± 4

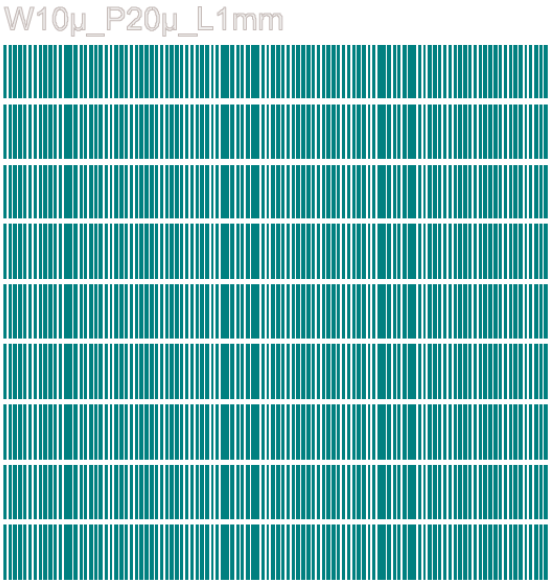

Figure A4.12 Layout of structure for fabricating the silicon (width: 10 µm; distance 20 µm; length of the individual lines: 1 mm; distance between lines: 100 µm).

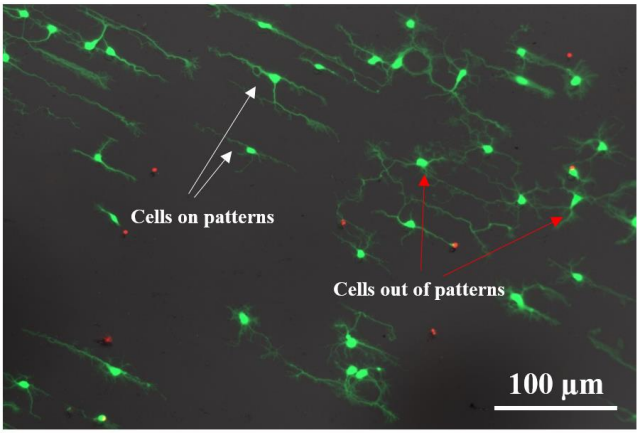

Figure A4.13 Estimating the guiding effectiveness of the FerNP patterns based on cells with axons on patterns (white arrows) and cells with axons out of the patterns (red arrows).

Band / Volume 159
Identifizierung von Bindungsdeterminanten von Tat-Vorläuferproteinen an den TatBCRezeptorkomplex während der Tat-abhängigen Proteintranslokation in *Escherichia coli*
A. Ulfig (2018), 186 pp
ISBN: 978-3-95806-290-0

Band / Volume 160
***Corynebacterium glutamicum* – a novel platform for the production of plant polyphenols**
N. Kallscheuer (2018), X, 98 pp
ISBN: 978-3-95806-291-7

Band / Volume 161
Neurons on 3D polymer nanostructures
A. Belu (2018), vii, 135 pp
ISBN: 978-3-95806-296-2

Band / Volume 162
Tailoring and Characterisation of Bioelectronic Interfaces
A. Markov (2018), 75 pp
ISBN: 978-3-95806-298-6

Band / Volume 163
Epitaxy of group IV Si-Ge-Sn alloys for advanced heterostructure light emitters
N. von den Driesch (2018), viii, 149 pp
ISBN: 978-3-95806-300-6

Band / Volume 164
Impact and Regulatory Control of the CGP3 Prophage in *Corynebacterium glutamicum*
E. Pfeifer (2018), IV, 206 pp
ISBN: 978-3-95806-301-3

Band / Volume 165
Establishment of Bacterial Microcompartments in the Industrial Production Strain *Corynebacterium glutamicum*
I. Huber (2018), X, 114, XI-XXXIV pp
ISBN: 978-3-95806-302-0

Band / Volume 166
Current-Induced Magnetization Dynamics in Ferromagnetic Nanowires
M. I. Khan (2018), vi, 138 pp
ISBN: 978-3-95806-308-2

Band / Volume 167
Management of Electrophysiological Data & Metadata
Making complex experiments accessible to yourself and others
L. Zehl (2018), 182 pp
ISBN: 978-3-95806-311-2

Band / Volume 168
Investigation of GeSn as Novel Group IV Semiconductor for Electronic Applications
C. Schulte-Braucks, Christian (2018), xx, 165, XII pp
ISBN: 978-3-95806-312-9

Band / Volume 169
Tailoring the Electronic Properties of Epitaxial Oxide Films via Strain for SAW and Neuromorphic Applications
Y. Dai (2018), VI, 133 pp
ISBN: 978-3-95806-319-8

Band / Volume 170
The electronic structure of transition metal dichalcogenides investigated by angle-resolved photoemission spectroscopy
M. Gehlmann (2018), ii, 108, XVIII pp
ISBN: 978-3-95806-324-2

Band / Volume 171
Control of neuron adhesion by metal nanoparticles
A. Q. Tran (2018), viii, 108 pp
ISBN: 978-3-95806-332-7

Schlüsseltechnologien / Key Technologies
Band / Volume 171
ISBN 978-3-95806-332-7

Mitglied der Helmholtz-Gemeinschaft

JÜLICH
Forschungszentrum